Title
Acute and Chronic Neural Stimulation via Mechano-Sensitive Ion Channels

Author
Tay, Andy

Publication Date
2017

Peer reviewed|Thesis/dissertation

UNIVERSITY OF CALIFORNIA

Los Angeles

Acute and Chronic Neural Stimulation *via* Mechano-Sensitive Ion Channels

A dissertation submitted in partial satisfaction of the requirements for the degree Doctor of Philosophy in Bioengineering

by

Andy Tay Kah Ping

2017

ABSTRACT OF THE DISSERTATION

Acute and Chronic Neural Stimulation
via Mechano-Sensitive Ion Channels

by

Andy Tay Kah Ping
Doctor of Philosophy in Bioengineering
University of California, Los Angeles 2017
Professor Michael Teitell, Co-Chair
Professor Dino Di Carlo, Co-Chair

Neural stimulation techniques for eliciting calcium influx can elucidate the physiological roles of specific neural populations. To overcome some of the limitations of existing techniques such as poor specificity and noxious effects of heat, I developed a technology for non-invasive control of neural activities using magnetic forces and magnetic nanoparticles (MNPs) which offer deep tissue penetration and controllable dosage. Extensive investigations with different neuro-toxins and experimental conditions support that the mechanism of magnetic stimulation that involves membrane-bound MNPs transducing magnetic forces into mechanical stretching of the cell membrane to enhance the opening probability of mechano-sensitive N-type calcium ion channels to induce calcium influx.

Making use of the ability of neural networks to actively regulate their ratio of excitatory to inhibitory ion channel/receptor, I also performed chronic magnetic stimulation on fragile X

syndrome (FXS) model neural networks. We found that chronic magnetic stimulation reduced the density of N-type calcium ion channels whose expression is increased in FXS. This technique demonstrates the potential of using bio-magnetic/mechanical forces to modulate expressions of mechano-sensitive ion channels where they are over-expressed in diseases such as abnormal nociception.

Nonetheless, there are still a few areas where the technique can be improved. Firstly, it is the use of MNPs with more uniform properties to have greater control on magnetic stimulations. Secondly, the technique needs to be useful for *in vivo* studies. Therefore, I started researching on magnetotactic bacteria (MTB) which produce biological MNPs with superior properties such as uniform sizes and highly homogenous magnetic properties with the goal of harvesting MNPs from them.

MTB, however, grow extremely slowly and the number of MNPs produced/bacterium is low. One way to overcome this problem is to evolve MTB over-producers of MNPs but this strategy is constrained by the absence of a selection platform that is quantitative and offer high throughput. To overcome this problem, I combined random chemical mutagenesis and selection using a magnetic ratcheting platform to generate and isolate MTB over-producers that produce twice as many MNPs/bacterium after 5 rounds of mutation/selection. I next designed a magnetic microfluidic device and demonstrate as a proof of concept, that it can be coupled to a bioreactor for high throughput microfluidic selection of MTB over-producers.

The dissertation of Andy Tay Kah Ping is approved.

Aydogan Ozcan

Felix Schweizer

Michael Teitell, Committee Co-Chair

Dino Di Carlo, Committee Co-Chair

University of California, Los Angeles

2017

DEDICATION

I would like to dedicate this work to my family (Father: Tay Chuan Lim, Mother: Teoh Swee Lian, Sister: Diana Tay Jia Yi) who supported my PhD journey.

I would also like to express gratitude to my lovely friends namely, Low Guanming, Lynn Ong Li Bing and Ker Wanlin for their encouragement and intellectual discussions to move my research forward.

I would also like to thank the National University of Singapore (NUS) for their financial support through the NUS-Overseas Graduate Scholarship and the various agencies for their fellowships that truly enriched my graduate experience. Specifically, I would like to thank Professor Lim Chwee Teck and Prof James Goh, my scholarship advisors under the NUS-OGS scheme.

Lastly, the work is not possible without my amazing mentor, Dino Di Carlo, who gave me confidence to explore my curiosity and space to establish scientific independence.

Table of Contents

ACKNOWLEDGMENTS

Chapter 1 contains the publication: Tay A., Schweizer, F. and Di Carlo, D. (2016) "Micro- and nano-technologies to probe the mechano-biology of the brain". Lab on a Chip, 16.11, 1962-1977. Doi:10.1039/C6LC00349D. AT wrote the manuscript. AT, FS, DD revised the manuscript.

Chapter 2 contains portion of the publication: Tay A., Kunze, A., Murray, C. and Di Carlo, D. (2016) "Induction of calcium influx in cortical neural networks by nanomagnetic forces". ACS Nano, 10.2, 2231-2341. Doi: 10.102/acsnano.5b07118. AT performed all the experiments. AK designed the magnetic chip. CM fabricated the magnetic chip. AT, AK and DD revised the manuscript. Chapter 2 also contains part of this publication: Tay, A. and Di Carlo, D. (2017) "Magnetic nanoparticle-based mechanical stimulation for restoration of mechano-sensitive ion channel equilibrium in neural networks". Nano Letters, 17.2, 886-892. Doi: 10.1021/acs.nanolett. 6b04200. AT performed all the experiments. AT wrote the manuscript. AT and DD revised the manuscript.

Chapter 3 contains part of this publication: Tay, A. and Di Carlo, D. (2017) "Magnetic nanoparticle-based mechanical stimulation for restoration of mechano-sensitive ion channel equilibrium in neural networks". Nano Letters, 17.2, 886-892. Doi: 10.1021/acs.nanolett.6b04200. AT performed all the experiments. AT wrote the manuscript. AT and DD revised the manuscript.

Chapter 4 contains the publication: Tay A., Murray, C. and Di Carlo, D. "Phenotypic selection of Magnetospirillum magneticum (AMB-1) using magnetic ratcheting". Advanced Functional Materials [In Press]. AT performed most experiments. CM fabricated magnetic ratcheting chip.

YC performed high resolution transmission electron microscopy. AT wrote the manuscript. AT and DD revised the manuscript.

Chapter 5 contains the publication (under preparation): Tay A., Pfeiffer, D., Rowe, K., Tannenbuam, A., Strangeway, R., Schüler, D. and Di Carlo, D. "Microfluidic magnetic separation for estimating the magnetic contents and cell cycle synchronization of magnetotactic bacteria". AT performed all experiments. DF and DS provided advice on MSR-1 culture and Δ*flaA* MSR-1 mutant. AT, KR, AT, RS performed magnetic field decay measurement with magnetometer. AT wrote the manuscript. AT and DD revised the manuscript.

Chapter 6 contains portion of the publication: Tay A. and Di Carlo, D. (2016) "Remote neural stimulation using magnetic nanoparticles". Current Medicinal Chemistry. Doi: 10.2174/0929867323666160814000442. AT wrote the manuscript. AT and DD revised the manuscript.

VITA

EDUCATION

University of California, Los Angeles (UCLA)

- Master's (Bioengineering) Sep 14-May 15

National University of Singapore (NUS) Aug 11-May 14

- Bachelor of Engineering (Biomedical Engineering) First Class Honors

SELECTED RESEARCH EXPERIENCE

UCLA Bioengineering Department, PhD Student Sep 14–Present

Neural stimulation

- Induce calcium influx in neural networks using magnetic forces
- Magnetic nanoparticle-mediated modulation of mechano-sensitive ion channel expressions

Directed evolution of magnetotactic bacteria

- Select mutant magnetotactic bacteria over-producer of high quality magnetic nanoparticles

Advisor: Di Carlo, Dino. Ph.D.

SELECTED ACADEMIC PUBLICATIONS

1. Andy Tay, Kunze, A., Murray, C. & Di Carlo, D. Induction of calcium influx in cortical neural networks by nano-magnetic forces. ACS Nano (2016).

2. Andy Tay, Kunze, A, Jun, D, Hoek, E & Di Carlo, D. The age of cortical neural network affects their interactions with magnetic nanoparticles. Small (2016).

3. Andy Tay, Schweizer, F. & Di Carlo, D. Micro- and nano-technologies to probe the mechano-biology of the brain. Lab on a Chip (2016).

4. Andy Tay & Di Carlo, D. (2016). Remote control of neuronal activities using magnetic nanoparticles. Current Medicinal Chemistry.

5. Andy Tay & Di Carlo, D. (2016) Nanoparticle-mediated restoration of ion channel equilibrium in neuronal networks. Nano Letters.

SELECTED SCHOLARSHIPS, AWARDS & HONORS

- Australia Endeavour Research Fellowship, Australia Department of Education 2017
- Travel Fellowship, Genetic Manipulation of Neuronal Activity IV (Janelia Farm) 2016
- University Fellowship, UCLA 2016
- Helmsley Fellowship, Cold Spring Harbor Laboratory (Course on Ion Channel) 2016
- Winner of Naturejobs Career Expo Journalism Competition, Naturejobs 2016
- Tony Award (2nd Place) Electron Microscopy Image Contest, FEI 2016
- Travel Fellowship, Global Young Scientist Summit (National Research Foundation) 2015
- Travel Fellowship, Biology of Ageing Conference (Singapore Immunology Network) 2015
- Travel Fellowship, Tropical School of Biophotonics 2015
- Non-Resident Graduate Academic Doctoral Award, UCLA 2014
- A*STAR Honor List, Agency for Science, Technology and Research 2014
- Asian-Pacific Medical Device Design Competition First Prize, IFMBE 2014
- Graduate Student Research Fellowship, UCLA 2014

Chapter 1: Micro- and Nano-Technologies to Probe Brain Mechanobiology

1.1 Introduction

In this chapter, I discuss the limitations of conventional tools for probing the mechano-biology of the brain and summarize published literature on micro- and nano-technologies to investigate neural mechanobiology with greater spatiotemporal resolution.

Technological advances and the growth of interdisciplinary research has now enabled the mechano-phenotyping of cells, enhancing our knowledge of the role of biomechanical forces (tension, pressure, shear, torque, stiffness (Young's modulus) etc.) on stem cell differentiation,[1] cancer metastasis[2] and malaria infection.[3] Similarly, there is now a growing number of publications of the role of biomechanical forces during brain development and neural development-related diseases in which understanding the mechanisms that allow neurons to sense, transduce and respond to mechanical stimuli, and the key molecules involved in the mechanisms has come to the forefront (**Fig. 1A**).[4]

Neurons continuously experience biomechanical forces that can affect their gene expression,[5] neurotransmitter release,[6] neurite outgrowth[7] and network connections.[8] In diseases such as autism spectrum disorder (ASO)[9] and traumatic brain injuries,[10] brain tissue misfolding has also been observed, suggesting the importance of biomechanical forces in guiding proper cognitive development and recovery (**Fig. 1B**).

To investigate the effects of biomechanical forces on neurons, conventional tools such as glass pipettes, atomic force microscopy[11] and osmotic pressure[12] have been utilized. However, these methods have extremely low throughput, require expensive equipment, and are not compatible with repeated and long term observation of the same cell/population (**Table 1**).[13]

Advances in micro-fabrication have made engineering micro- and nano-technologies possible for electrophysiological recordings on soft substrates[14] and likewise to apply biomechanical force on neurons.[13] Micro- and nano-technologies making use of micro-channels or functionalized nanoparticles can offer high spatial and temporal resolution for applying biomechanical forces in a high throughput fashion.[15] In addition, these technologies match the length scales of cells, require smaller number of cells and less reagents, and have efficient nutrient and waste transport to enhance neuronal viability.[16,17] Micro- and nano-technologies also do not require expensive and bulky equipment, and can be more easily adopted in laboratories (**Table 1**).

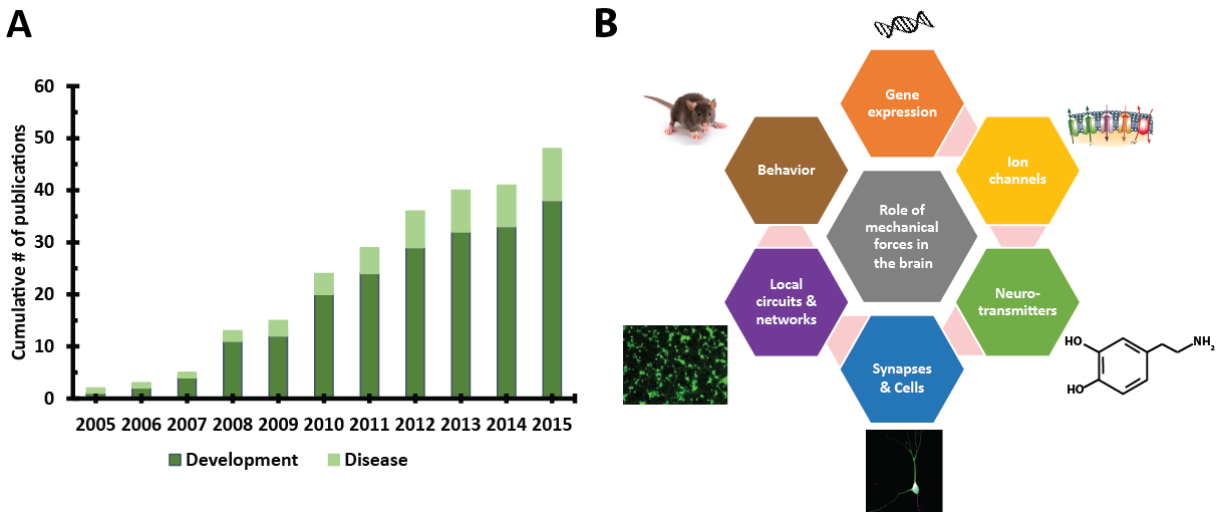

Fig. 1 Cumulative publications on micro- and nano-technologies capable of studying the role of biomechanical forces on brain function. (**A**) Literature search was performed using Google Scholar, PubMed and ScienceDirect databases. Key words 'micro', 'nano', 'neurons', 'neural', 'brain', 'mechanics', 'neurite', 'technologies' were used in various combination and with the Boolean operators '+/AND', '*/unknown' and 'OR'. The year range was restricted from 2005 to 2015. (**B**) Biomechanical forces can influence brain function at various length scales and hierarchy such as gene expression, synapse formation, neurite outgrowth and cortical folding. Image: ion channels reproduced with permission from [18]/ Nature Publishing Group. Reproduced with permission from the Royal Society of Chemistry.

1.2 Tools to explore the effects of biomechanical forces on the brain

Research over the years has unraveled various mechanisms or cellular components responsible for sensing mechanical stimuli in neurons: (i) the *viscoelastic* plasma membrane that consists of a

phospholipid bilayer that shows frequency dependent changes in tension and viscosity (*Maxwell material*) in response to mechanical stimuli that can trigger conformational changes in mechano-sensitive ion channels,[19] (ii) the polymerization and de-polymerization of actin monomers into polymers[20] that is implicated in *axonal growth cone* dynamics[21] and *dendritic spine plasticity*,[22] (iii) microtubules that can generate forces via polymerization of αβ-tubulin dimers or *catastrophic de-polymerization* that can influence *intracellular cargo transport* and *dendritic spine morphology*,[23] (iv) neuro-filaments which are abundant cytoskeletal proteins in myelinated axons[24] that are proposed to provide mechanical protection to the brain against compressive loads such as during injury[25] and (v) the extracellular matrix and cell adhesion molecules that provide a mechanical framework for cellular growth and can influence signal transduction.[26] As the mechanisms for mechanical stimuli sensing in neurons are not the focus of this review, we refer the readers to Tyler et al.[4] and Tsunozaki and Bautista[27] for a more comprehensive overview of this topic.

1.2.1 Conventional tools

The neuroscience community has developed and conventionally used a few techniques to probe the mechano-biology of the brain. Pressure can be exerted on neurons using micro-motor-driven glass pipettes and glass pipettes delivering solution of different osmolality to the neurons. Fluid shear stresses can also be generated using perfusion. These aforementioned techniques are compatible with traditional patch clamp approaches to measure the electrical activity of mechano-sensitive ion channels. Atomic force microscopy and deformation of flexible substrates are more recent tools developed to investigate the effects of biomechanical forces on neurons. Although it

is still a challenge to integrate them with patch clamp, these latter methods exert more precise forces on neurons.

Motor-driven pressure: In this method, positive focal pressure is applied via a piezoelectric micro-stage with user-input step size and step velocity to create membrane deformations (**Fig. 2A**).[28] The cell body is voltage-clamped in a whole-cell configuration and the neurite is stimulated with a polished glass probe with concurrent electrophysiological recordings to correlate mechanical stimuli with stimulus-induced current. Using this technique, it is possible to investigate the relationship between the kinetics of membrane deformation and mechanical sensing.[28]

Patch membrane pressure: This technique is similar to traditional patch clamping where a negative/positive pressure is applied to a patch membrane via a patch pipette. The induced membrane deformations are then correlated with data from concurrent electrophysiological recordings (**Fig. 2A**).[29] The size of the patched membrane can also be varied for single ion channel recordings. Calibrated pressure can be applied to the cell, and parameters such as different step size and period between step sizes can be defined by the user. One key advantage of this technique is the ability to deliver neuro-toxins or inhibitors to the neurons via the solution in the patch pipette, and to investigate the role of different ion channels responsible for responding to mechanical stimuli.[30] Absolute membrane capacitance can also be determined using this technique by fully dilating the cells followed by measuring the cell diameter.

Osmotic pressure: In this technique, bath compositions with varying osmolarity can be used to induce cell shrinkage (hypertonic solution) or cell swelling (hypotonic solution) (**Fig. 2A**).[30]

Deformation of the cell membrane in response to changes in osmotic pressure is then measured and correlated to changes in electrophysiological recordings. Nonetheless, osmotic pressure does not generate uniform tension in the cell membranes attributing to heterogeneous lipid membrane composition. This limitation complicates data interpretation.[31]

Fluid shear stresses: Shear stresses can be applied to neurons by perfusing solution with a certain shear rate and viscosity across the seeded neurons (**Fig. 2A**).[30] It has been found that shear stresses can induce signal transduction and upregulation of Bcl-1, a regulatory protein of cell death.[32] Similar to some of the described techniques above, this method can be used in tandem with electrophysiological recordings and to correlate changes in neuronal physiological activities with shear-stress induced gene expressions.

Deformation of flexible elastomer: In this technique, a calibrated vacuum pressure chamber is used to distend a flexible elastomer substrate to mechanically stretch and relax the seeded neurons (**Fig. 2A**).[33] The substrate can also be patterned with proteins to create protein gradients[34,35] with different stiffness[36] and topographies such as grooves to influence neuronal growth.[37,13,38] This method offers much higher throughput compared to the aforementioned techniques which assess mechanically evoked responses one cell at a time. Using this technique, scientists have found that mechanical stresses can mediate synaptic transmission and that applied tensions on neurites can preferentially favor the fate of neurites to become the axons which are typically longer than dendrites.

1.2.2 Micro-technology tools

Atomic force microscopy (AFM) and micro-cantilever: AFM makes use of a functionalized cantilever tip to form a bond with a molecule of interest on the cell membrane.[39] Deflections of the tip are used to construct a topographical map of the cell surface and can even be used to image 3D-sub-cellular features. The equipment can apply force and measure the force generated by the interactions between the functionalization molecule and membrane molecule. However, neurons can be detached from the surface of adhesion when the applied force is too great and care must be taken to avoid this.[39]

Gopal et al. described a 1D-microfabricated silicon cantilever probe combined with photonic nanogratings.[40] The probe displacement which is correlated to the applied biomechanical force can be calculated through the grating transmission spectrum. However, this technique is not compatible with 2 or 3D studies and there has been no subsequent follow-up study to further validate its use in researching the mechano-biology of the brain.

Micro-channels and micro-patterning: Various designs for 3D microfluidic chambers are available for modelling axonal growth, injury and recovery.[35,41,42] In most designs, the surfaces of the microfluidic chambers are patterned with adhesion proteins for directional growth[34] and the chambers are separated by a filter composed of microgrooves that allow only neurites but not cell bodies to grow through, thus separating the cell body from neurites (**Fig. 4A**).[41] High fluidic resistance is offered by the microgrooves which leads to diffusion-dominant transport of nutrients from one chamber to another that enables neuronal survival.[42] As axons typically grow faster than dendrites,[43] it is thus possible to isolate axons and use the system as a model for assessing the impact of biomechanical forces (such as using valves to apply pressure) on axonal injury and

recovery.[44] Pulsed laser excitation has also been integrated with micro-channels to induce acute axonal injuries and such systems can offer high throughput results for drug screening to accelerate axonal recovery.[45] Co-culture microfluidic platforms when combined with micro-technologies to exert mechanical forces on seeded neurons, astrocytes and oligodendrocytes can also be developed to investigate the role of different neural cells in neuronal development, injury and recovery.[46]

Potential tools: Progress in droplet microfluidics has enabled the generation of droplets having different sizes, composition and shapes.[47] Campàs et al. described the use of fluorescent oil micro-droplets to determine cell generated mechanical forces during tissue morphogenesis.[48] Surface-functionalized droplets introduced among the cells are subjected to local deformations as the cells develop. With the use of confocal microscopy and modelling, the group could quantify the forces exerted by different cells in a 3D tissue environment. It would be interesting to synthesize micro-droplets with rapidly adjustable surface tension controlled by light, temperature or pH and utilize them to apply or measure mechanical forces on neurons in living tissues.

There have also been reported literature making use of microelectromechanical system (MEMs)-resonators for probing the mechano-biology of cancer and neural cells. Corbin et al. first modelled the relationship between resonant shift effects and viscoelasticity of cells.[49] They next measured the frequency shifts from pre- and post-fixed breast cancer cell lines and found that more invasive cancer cells are softer and less stiff. Their results correlated well with measurements from AFM and clinical studies showing greater malignancy with softer cancer cells. Previously, Corbin and co-workers also made use of MEMs-resonators with media flow to measure the mass and growth (establishment of polarities, axonal elongation) of individual neural cells.[50]

Park and colleagues also introduced the vibration-induced phase shift method to understand cell stiffness by measuring the phase and amplitude of its height oscillations using a laser Doppler vibrometer.[51] This technology has shown potential for long-term study of single cells with minimal perturbations.

It has been reported by several groups that neuronal maturation and growth are favored in softer substrates.[52] One application of MEMs technologies can be to understand whether the stiffness of individual neural cells relate with their preferred growth environment. It is also high exciting to further develop MEMs to correlate cellular biophysical properties to physiological parameters such as gene expression, neurite outgrowths and synaptic transmission. Future ideas for this field would include development of platforms for measuring correlation of vibrational activity of neural cells with calcium-mediated signaling and multi-modal out-of-phase measurements of cells with functionalized beads.

1.2.3 Nano-technology tools

Ferromagnetic nanoparticles and magnetic forcing: *Ferromagnetic nanoparticles* (MNPs) can be quickly magnetized in the presence of a magnetic field. Micro-devices patterned with magnetic elements have been fabricated to establish steep magnetic gradients to enhance the magnetization of MNPs and resulting forces on neurons.[53] It has been shown that internalized MNPs can influence the protein tau distribution which affects the polarization of neurites for axon formation.[54]

Calcium is an important second messenger that is implicated in various signaling pathways that regulate gene expression.[55] In order to act as a specific second messenger, cytoplasmic calcium

concentration is maintained at a much lower concentration (100-300 nM) compared to extracellular spaces (1-3 mM) and endoplasmic reticulum (10-100 μM).[56] There is significant interest to manipulate calcium levels, especially in neurons where calcium dynamics within dendritic spines are associated with synaptic plasticity in neural networks.[57] Tay et al. have demonstrated that membrane-bound MNPs can trigger calcium influx in cortical neural networks patterned onto micro-fabricated devices with magnetic elements (**Fig. 2C**).[58]

Piezoelectric nanoparticles and ultrasound: Nanoparticles composed of materials such as barium titanate have *piezoelectric* properties and can be used to transduce ultrasound energy into mechanical perturbations and electricity.[59] Piezoelectric nanoparticles that bind to membranes have shown potential to elicit calcium and sodium influxes into neurons upon wireless ultrasound stimulation in a dose-dependent manner (**Fig. 2C**).[60]

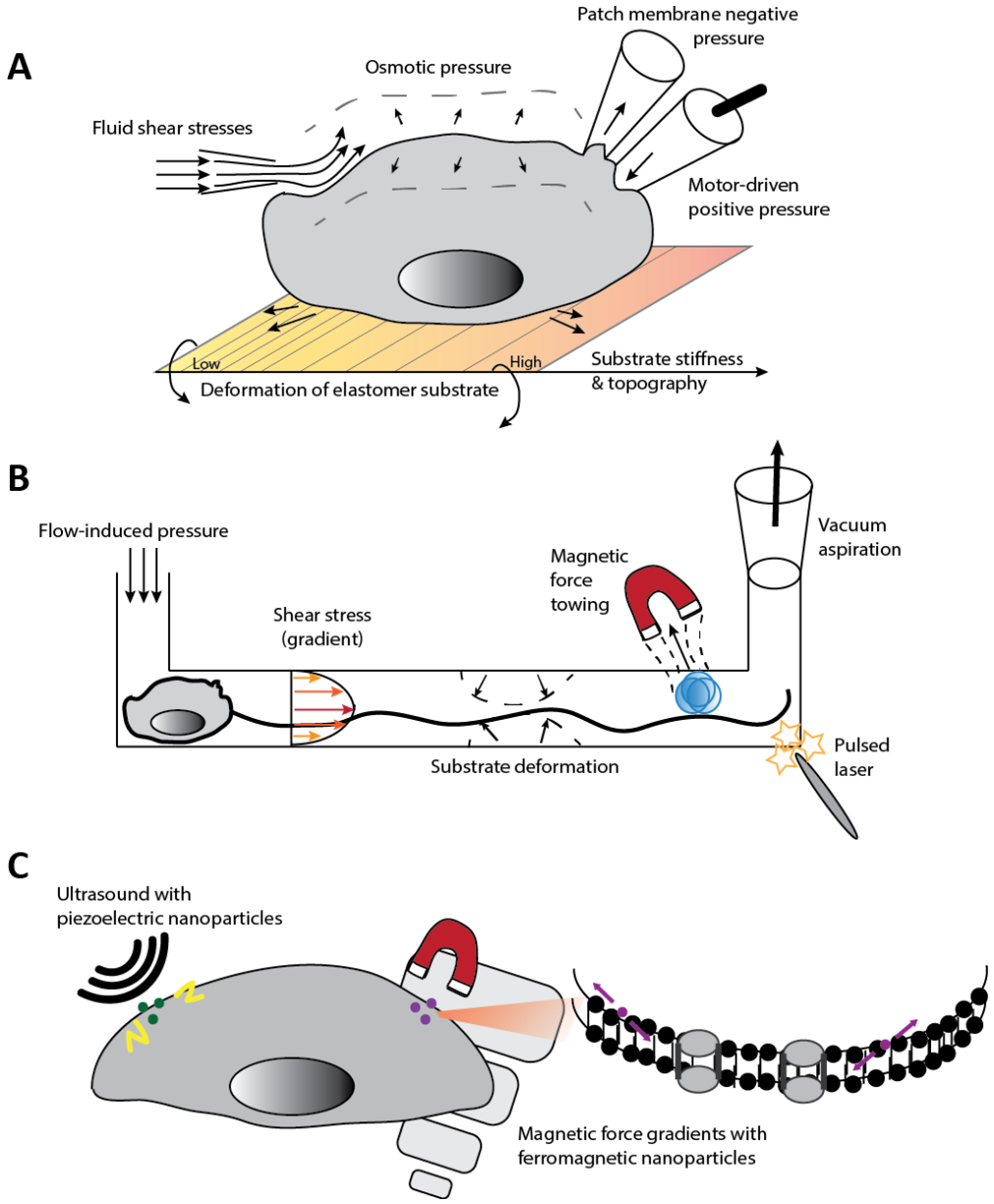

Fig. 2 Conventional, micro- and nano-technologies to probe the mechanobiology of the brain. (**A**) Conventional tools include the use of glass pipettes to apply positive and negative pressure which can be integrated with electrophysiological recordings. Fluid shear stresses and osmotic pressure techniques have also been used but they are generally limited by non-uniform generation of tension on the neurons. Neurons can also be seeded onto protein-coated substrates with various stiffness and chemical gradients and be subjected to mechanical stretching. Image inspired by [19]. (**B**) Micro-technologies facilitate precise spatial control of neuronal seeding and axonal growth. Using multi-compartment microfluidic devices, flow-induced pressure, fluid shear stresses and vacuum aspiration can be applied. Owing to the high flexibility of substrates, mechanical forces can also be applied to neurons or sub-cellular components via substrate pulling or compression. Magnetic nanoparticles and pulsed laser techniques have also been integrated with micro-technologies to increase the spatiotemporal control of force application. (**C**) Nanotechnologies make use of neurons seeded onto surfaces that impart magnetic gradients where upon magnetic force application, intracellular protein distribution can be biased and calcium influx can be triggered. Ultrasound has also been coupled with piezoelectric nanoparticles to perturb mechano-sensitive channels and generate electric fields to trigger calcium influx. Reproduced with permission from the Royal Society of Chemistry.

Table 1 Comparisons of tools used to probe mechano-biology of the brain

Methods	Information from technique	Advantages	Disadvantages
Conventional			
Motor-driven pressure	• Correlation of membrane deformations (magnitude, kinetics) to changes in electrophysiology • Activity changes in single ion channel *[only patch] • Usually one-off measurements	• Compatible with patch champing	• Low throughput • Expensive equipment • Steep learning curve for users • Sensitivity of step size is dependent on motor
Patch membrane pressure		• Compatible with patch champing	• Low throughput • Expensive equipment • Steep learning curve for users • Sensitivity of step size is dependent on motor
Osmotic pressure		• Compatible with patch champing	• Low throughput • Steep learning curve for users • Non-uniform tension in membrane
Fluid shear stresses	• Cellular responses to shear stresses (magnitude, direction) • Potential for long term monitoring	• Compatible with patch champing	• Low throughput • Non-uniform shear stress on neurons
Atomic force microscopy	• Cell stiffness • Cell elasticity • Usually one-off measurement	• Can investigate specific molecular interactions for mechanical sensing	• Low throughput • Cell detachment from surface
Stretching of flexible elastomer	• Cellular response to mechanical forces (direction, magnitude, frequency)	• Higher throughput • Can be combined with micro-electrode arrays for electrophysiological recording	• Cell detachment • Difficult to integrate with patch clamping • May generate non-uniform tension in membrane

	• Potential for long term monitoring		
Micro-technologies			
Multi-compartment micro-channels	• Cellular growth, injury and recovery in response to mechanical forces (magnitude, direction, duration) • Response of different neural cells to applied mechanical forces • Roles of different neural cells and chemicals in neuronal recovery after injury • Concomitant monitoring of cellular responses such as calcium signaling, up/down-regulation of genetic pathways in response to mechanical forces • Results from long-term studies	• Low cost • High throughput • Co-culture is possible • Compartmentalization • Controlled laminar flow • Similar length scale to cell size • Easy for large-scale manufacture • Tunable mechanical properties such as stiffness • Compatible with microscopy due to transparent material • Efficient nutrient delivery and waste exchange to enhance neuronal viability • Fine spatial (with surface patterning and micro-structures) and temporal control of neurochemical environment	• Unknown leaching of chemicals through micro-channel walls such as inhibitors added for experiment • Ways for sealing of micro-channel openings need to be developed as water evaporation can also generate unwanted forces on seeded neurons • Reproducibility of force application may be low in certain configurations, and thus modeling and experimental validation prior to testing with neurons are desired. • Not suitable for growing certain neurons such as motor neurons from spinal cord due to small size of micro-devices
Nano-technologies			
Ferromagnetic nanoparticles	• Local and specific response of different	• Remote control • High throughput	• Nano-toxicity • Requires magnetic gradients to enhance magnetic force strength

	neural cells to applied mechanical forces • Cellular responses to mechanical forces applied at much higher temporal resolution than other techniques can offer • Sensitivity of different neural cells to a wide magnitude range of mechanical forces • Results of chronic stimulation for long term studies	• Quantifiable mechanical forces • High spatiotemporal resolution • Non-invasive method of force application • Nanoparticles with different surface groups, charge and sizes can be used for specified targeting	• May require surgery to implant magnetic chips/elements into brain tissues • Numerous mechano-sensitive ion channels may complicate specific targeting
Piezoelectric nanoparticles		• Remote control • High throughput • Quantifiable mechanical forces • High spatial (2D) and temporal resolution • Non-invasive method of force application • Nanoparticles with different piezoelectric properties such as crystal structures can be used	• Nano-toxicity • Poor penetration of ultrasound through the skull

1.3 Effects of biomechanical forces on cellular functions

In this section, the effects of biomechanical forces on gene expression, ion channels, and cellular and tissue level behaviors of neurite outgrowths to brain folding are described. Micro- and nano-technologies employed in related studies are also reviewed. However, as seen from **Fig. 1A**, the number of publications in this field is still growing, and therefore, potential integration of micro- and nano-technologies are also proposed to provide readers with new potential areas of research. The literature is intentionally arranged to show the progression from the genetic to cellular and organ level. Although the effects of biomechanical forces on the brain are described in different sections, it must be noted that fundamentally, they are inter-connected as shown in **Fig. 3**.

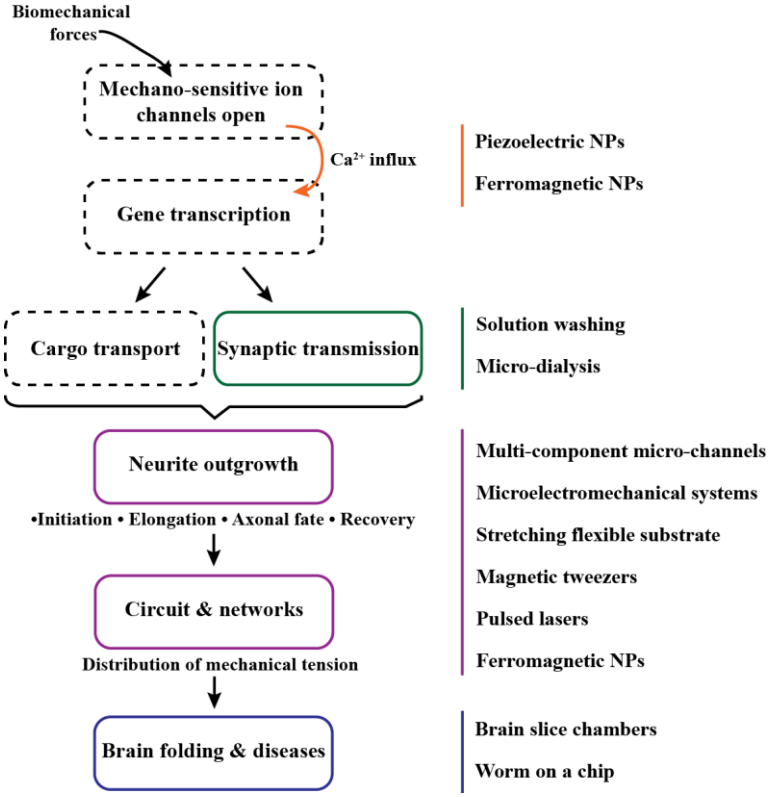

Fig. 3 Graphical summary of most of the research findings described in this review. Left: influence of biomechanical forces on mechano-sensitive ion channels leading to calcium influx and gene transcription. This then affects neurite outgrowth and neuronal networks, eventually culminating with an impact on brain folding and brain-related diseases. Right: micro- and nano-technologies that have been developed to interface at the different levels (color-coded). Reproduced with permission from the Royal Society of Chemistry.

1.3.1 Regulation of gene expression and calcium influx

Biomechanical forces play a pivotal role in regulating gene expression in mechano-sensory neurons responsible for touch sensations and pain sensation (nociception).[61] Mechano-sensory neurons transduce mechanical forces into electrical signals via mechano-sensitive ion channels.[62] Two main mechanisms have been proposed to understand how forces can activate mechano-sensitive ion channels: (i) the lipid bilayer stretch model where tension in the membrane triggers conformational changes such as membrane curvature, resulting in opening of ion channels. This is the simplest model and was derived from studies on MscL and MscS that allow *Escherichia (E.) coli* to sense osmotic stresses[63] and (ii) the spring-like tether model where an external molecule binds directly to mechano-sensitive ion channels and upon deflection by external stimuli, the tether opens the ion channels.[62] Readers can refer to Chalfie et al. for a more thorough review of the different mechano-sensory genes.[64]

Conventional: The mechanosensitive nature of ion channels discovered thus far had relied on conventional tools such as glass pipette and osmolality changes. Due to the extensive literature in this area, only selected studies using different conventional techniques will be reviewed. **Table 2** shows a list of mechano-sensitive ion channels.

Zhang and colleagues induced swelling and shrinkage of magnocellular neurosecretory cells (MNCs) by changing pipette pressure or osmolality of injected fluid and found that osmosensory transduction is a reversible mechanical process that depends on an intact actin cytoskeleton.[65] The team also found that volumetric changes triggered mechanical gating of the stretch-inhibited cation channels which led to change in channel conductance as measured with patch clamps. Similar experiments were also performed by Viana et al. who investigated the effects of hypo-osmotic membrane stretch on intracellular calcium concentration and found that the

pattern and rate of calcium influx could be correlated to the different functional sub-types of mouse sensory trigeminal neurons.[66]

The patch pipette technique has also been used in numerous studies to elucidate the mechanical-sensing properties of ion channels. For instance, Vilceanu and Stucky performed focal mechanical stimulation by applying patch membrane pressure on dorsal root ganglion (DRG) neurons and found that the TRPA1 ion channel mediates the slowly adapting mechanically activated currents.[67]

Bhattacharya et al. radially stretched primary somatosensory neurons and found that sub-populations of neurons (identified by their molecular markers and sizes) could be activated by different stretch intensities.[33] Although calcium influx was observed in all sub-sets of neurons, different neurons displayed different sensitivity to stretch. This study is highly insightful as it revealed that even within the TRPV1 ion channels, those that were dually sensitive to hydroxy-α-sanshool and capsaicin were stretch sensitive while those that were dually sensitive to capsaicin and menthol were stretch insensitive. The results highlighted the utility of technologies capable of providing precise and reproducible force ranges to understand the mechano-sensitivity of different sub-populations of neurons in the nervous system.

Micro-technologies: Microfluidic devices have been designed to investigate the influence of biomechanical forces on the gene expression in stem cells[68] and cardiac cells,[69] but no similar device has yet been adopted by the neuroscience community. 3D microfluidic devices can be coupled to equipment such as micro-motor and syringe pump-driven flows to apply mechanical stretching and shear stresses to cultured neurons. The magnitude and frequency of the forces is user-controlled and cultured neurons can be harvested easily from the micro-channels using trypsin for downstream gene expression studies. Nonetheless, this method is only suitable for study of the

bulk population and to explore the heterogeneous response of sub-populations of neurons to mechanical forces, single cell analysis may be integrated as a downstream assay after mechanical stimulation in microfluidic chambers. Such studies will be crucial to reveal the relationship between biomechanical forces and their effects on gene expression to excite neurobiologists about this area of research.

Nano-technologies: Although conventional tools have been useful to discover the mechano-sensitivity of many ion channels, their low spatiotemporal control of mechanical force application might not have provided the most accurate description of the properties of the ion channels. For instance, the force threshold for opening of mechano-sensitive ion channels cannot be captured using conventional tools which have minimum applied forces larger than the force threshold of ion channel activation. Furthermore, conventional tools such as changing osmolality creates non-uniform tension on the membrane which can complicate data interpretation. In these aspects, nano-technological tools that are able to provide uniform mechanical forces with much higher spatiotemporal resolution can further elucidate the properties of mechano-sensitive ion channels.

Marino and co-workers utilized piezoelectric barium titanate nanoparticles with tetragonal configuration that preferentially bind to the surface of neurons to trigger calcium and sodium influx upon ultrasound stimulation (**Fig. 4E**).[60] This method can facilitate remote control of neuronal circuitry in a non-invasive manner and has demonstrated that the induction of calcium influx can enhance neurite outgrowth and bias the direction of neurite growth,[59] making it a compelling potential nano-therapeutic method. To understand the mechanisms for calcium influx, the authors showed that treatment with gentamycin, an inhibitor of some mechano-sensitive ion channels,[70] did not affect the calcium transients. Nonetheless, gentamycin is unable to inhibit all mechano-

sensitive ion channels.[71] We speculate that the use of piezoelectric nanoparticles might still have interacted with mechano-sensitive ion channels, which contributed to parts of the calcium influx. While the ultrasound technique demonstrates an attractive means of remotely controlling the brain circuits, it must be acknowledged that ultrasound penetration through the brain is still limited.[72] Furthermore, as the neurons used in the experiments are differentiated from neuroblastoma cells which have large size variations, the observed large amplitude calcium influx may be a consequence of large cell size and not ultrasound stimulation.[73] Lastly, the authors only demonstrated calcium influx in single cells but not propagation in neural networks which is crucial to understand brain functions.[74]

Tay et al. have also demonstrated the induction of calcium in cortical neural networks using magnetic force stimulation with membrane-bound MNPs (**Fig. 4F**).[58] An average of 20% increment in calcium fluorescence signals (observed by fluo-4 fluorescent calcium indicator) and a heightened frequency in calcium spiking was observed in stimulated neural networks. The team also inhibited N-type mechano-sensitive calcium channels with ω-conotoxin and found that the stimulatory effects of the magnetic forces were diminished. Nonetheless, further work with different neuro-toxins such as tetrodotoxin and patch clamping are necessary to confirm the specific targeting of N-type calcium channels.

As illustrated in **Fig. 3**, mechano-sensitive ion channels are a critical link between calcium influx and downstream effects such as modification of gene expressions and neurite outgrowths. Nano-technological tools offering higher spatiotemporal resolution and capability to generate precise and reproducible force range on the neurons can be employed in *in vitro* and *in vivo* studies to map out how the strength and frequency of calcium signals affect neuronal functions.

Table 2 List of some mechano-sensitive ion channels

Ion type	Channel (year of discovery)[ref]	Mechano-related application (year of application)[ref]
K^+	Shaker (K_v1) (1969)[75]	N.A.
	TRAAK ($K_{2P}4.1$) (1995)[76]	N.A.
Na^+	$Na_v1.5$ (1984)[77]	N.A. Note: $Na_v1.5$ is found primarily in cardiac muscle cells.
Ca^{2+}	N-type (1985)[78]	Membrane bound ferromagnetic nanoparticles activate N-type Ca^{2+} channels to trigger Ca^{2+} influx via lipid membrane stretching (2016)[58]
Mixed cationic	TRPV1 (1969)[79]	TRPV1 is not sensitive to mechanical stimuli *but* instead its heat-sensitive property is exploited to control worm movements (2010)[80] and induce calcium influx using generated heat from MNPs (2015)[81]
	PIEZO2 (2010)[82]	NPs with piezoelectric properties have been used to trigger calcium influx but the connection to PIEZO2 is *not* yet demonstrated (2015)[60]
Cl^-	CFTR (1989)[83]	N.A. Note: CFTR is found primarily in lung epithelial cells.

K_v1: voltage gated K^+ ion channel; 2P: 2 pore domain; TRAAK: TWIK-related arachidonic acid stimulated; $Na_v1.5$: voltage gated Na^+ ion channel; TRPV1: transient receptor potential cation channel subfamily V member 1; PIEZO: piezo-type mechanosensitive ion channel component 2; CFTR: cystic fibrosis transmembrane conductance regulator. Refer to [4] for more examples of mechano-sensitive ion channels.

A few interesting observations can be made from **Table 2**:

(1) There are a few biomedical applications that attempted to modulate the activation of Ca^{2+} ion or mixed cationic channels as Ca^{2+} is an important second messenger for intracellular signaling and cell control. On the other hand, Na^+, K^+ and Cl^- ion channels have not found use in related applications yet. These may be because the latter ions are implicated in action potential generation and have lower sensitivity to mechanical forces. Therefore, triggering their opening is less specific and may have adverse downstream consequences.

(2) Biomedical applications modulating ion channels usually made use of nanoparticles. One interesting idea is to doubly conjugate nanoparticles with target peptide specific to an ion channel for specific mechano-activation and antibodies to specific brain regions for nano-therapeutic applications.

(3) There is an unusually long time gap between the discovery of the ion channel and using the ion channels for biomedical applications. We expect that enhanced collaboration between neuroscientists and engineers can reduce the time gap.

1.3.2 Regulation of synapses and neurotransmitter release

As discussed earlier, calcium influx can be triggered by mechanical forces *via* the mechano-sensitive ion channels. The resulting calcium influx is strongly tied to the release of *neurotransmitters* encapsulated in vesicles at the pre-*synaptic* terminal and subsequent fusion of vesicles at the post-synaptic terminal.[84] Siechen and co-workers found that vesicle clustering at the neuromuscular presynaptic terminals of embryonic *Drosphila* depended on the mechanical tension in the axons.[6] In severed axons which are slack, vesicle clustering was absent; however, vesicle clustering was restored with the application of mechanical tension to the severed end of the axon. Vesicle clustering was also observably increased when mechanical tension was applied to axons indirectly via the post-synaptic muscle. The team proposed that tension could influence actin polymerization and de-polymerization which preceded vesicle clustering.[85] This observation suggests that mechanical tension can modulate vesicle clustering at synapses, and thus may mediate the strength of synapses, plasticity and memory.

Conventional: Fan et al. constructed a device where a brain slice were placed between screws and rotation of the screws would result in uniaxial stretching of the brain tissues and neurons residing in them.[86] Synaptic excitability was observed to be modulated by mechanical tension and repeated mechanical stimulation resulted in cumulative excitability. An interesting but still unexplained observation is that hyper-osmolality can induce enhanced release of neurotransmitters. Making use of stretch motor and changing the osmolality of the solution, Kashani and co-workers found evidence that both stretch and hyper-osmolality triggered neurotransmitter release in the frog neuro-muscular junctions, supporting the influence of biomechanical forces in regulating synaptic activities.[87]

Micro-technologies: Nerve and muscle cells communicate via neurotransmitters at the neuromuscular synapse to coordinate mechanical responses to stimuli. Tourovskaia et al. made use of a microfluidic device to apply agrin, a proteoglycan,[88] focally to protosynaptic acetylcholine receptors (AchR) in muscle cells. After 4 h of agrin exposure (100 nM), it was found that there was enhanced aggregation (10%) and reduced loss of AchR (17%) at the agrin-treated areas.[89] This platform can be modified to study the formation, pruning and aggregation of vesicles or receptors at the synapses of neurons subjected to various mechanical forces during developments or in disease states. One possible configuration is where neurons and muscle cells are co-cultured in separate chambers to establish neuromuscular synapses. The chambers for each cell type can then subjected to different magnitudes of mechanical forces to evaluate the impact of forces on vesicle and receptor clustering at the synapse and synapse maintenance.

Disruption of synaptic transmission is implicated in numerous psychiatric and neurological diseases where the mechano-biology of the brain may play a role.[90] By combining microfluidic device designs capable of applying mechanical forces and collecting neurotransmitters released transiently due to the mechanical stimuli, there can be better understanding of the relationship on the effects of biomechanical forces on synaptic transmission.

Due to the short time scale of neurotransmitter release (hundreds of milliseconds), it has been difficult to apply transient pulses of neurotransmitters to study the role of *ligand-gated ion channels* in neuronal developments and neuro-diseases.[91] Photo-activation of 'caged' neurotransmitters requires expensive reagents and equipment and this technique is limited by the library of photoactivatable compounds.[91] Optogenetics also require exogenous expression of photo-sensitive genes.[92] Microfluidic devices have been employed in solution switching to transiently apply brief (~400 μs) gamma-aminobutyric (GABA) to recombinant $GABA_A$ receptors

to evoke current resembling hippocampal inhibitory post-synaptic currents.[91] Taylor et al. also described a microfluidic local perfusion (μLP) chamber to direct the formation of synapses in >100 parallel rows for high throughput manipulation of pre- and post-synaptic regions.[93] The presence of multiple perfusion channels facilitate high spatiotemporal control of glutamate treatment and monitoring of calcium fluctuations. The platform was also used to show that perfusion of dihydroxyphenylglycine (DHPG), an agonist of glutamate receptor, over dendrites signaled the nucleus to trigger transcription of activity-regulated-cytoskeleton-associated-protein (Arc) and the Arc mRNA was first accumulated in the soma and was later re-distributed to the synaptic regions. These aforementioned platforms can facilitate high throughput manipulation of synapses arranged with fine spatial control e.g. in parallel rows.[94] The device, and hence the neurons, can be coupled to mechanical stretching, followed by subsequent transient solution perfusion and collection of neurotransmitter released due to mechanical stimuli. Microfluidics have also found utility for micro-dialysis where micro-devices with partially permeable membranes with selective molecular weight cut-offs are implanted in brain areas to continuously sample chemical molecules diffusing through them.[95] One possible integrated system would be to arrange synapses in parallel rows, followed by mechanical stretching of the system to activate mechano-sensitive ion channels and detection of neurotransmitter release using micro-dialysis[96,97] to enhance our insights into the role of mechanically-activated neurotransmitter release. This integrated system can be a tool to enable better design of bone inserts to apply electronically-controlled force ranges on surrounding neurons in damaged spinal cord.

1.3.3 Regulation of neurite growth

In early neuronal development, *neurites* sprout from the cell body and the tips of the neurites i.e. *growth cones* advance by pulling onto substrates, and hence elongating the neurites.[98] After the second day of *in vitro* culture, one of the neurites experiences accelerated growth and becomes the axon while the other neurites become dendrites.[43] It has been shown that tension exerted on neurites can initiate outgrowth or lead to elongation above a force threshold while viscoelastic deformation without growth or retraction can occur when the applied tension is below the threshold.[99,100] Excessive mechanical tension can also lead to neurite retraction due to deformations of mechano-sensitive ion channels.[101] Interestingly, it has also been proposed that mechanical tension and a critical neurite length (~10 μm longer than other neurites) can specify axonal fate, potentially establishing neurons with two axons (Note: usually neurons have only one axon).[7] The growing neurites can also form communication networks which increase the tensile forces on each neuron. The accumulation of mechanical tension can also promote the elongation and elimination of neurites,[8] eventually affecting folding in the brain.[102]

Conventional: Making use of calibrated glass needles and a micro-manipulator, Chada and colleagues showed that neurite outgrowth can be initiated with mechanical forces earlier (a few hours after seeding) than spontaneous outgrowth i.e. ~ day 1-2.[99] The team also found that neurons (forebrain *vs*. sensory) displayed different responses to mechanical tension as there was an absence of a force threshold for neurite initiation in the former neuronal population. Similar to these findings, it was found that live *Drosophila* neurons behaved like a *viscoelastic* solid (*towed axons* lengthened linearly with applied forces) and maintained a resting tension of 1-13 nN.[103] The neurons could also respond to sudden release of tension by contraction and subsequent generation of tension back to the resting state. Recently, it has been found that neither actin filaments nor

tubulin polymerization is required for initial neurite outgrowth in *Drosophila* neurons which is highly regulated by kinesin-1.[104] Microtubule motor kinesin-1 facilitates the sliding movements of microtubules against each other especially in young neurons. However, as the neurons aged, microtubule transport is heavily downregulated, suggesting the role of different proteins at different developmental stages in neurite initiation and elongation.

Making use of a micro motor-stepper moving at a rate of 3.5 μm per 5 min, Smith and co-workers were able to extend the length of thousands of axons by more than 1 cm (1000x longer than an average neuron) after 10 days of stretching.[105] However, at double the pulling rate, the axons were unable to withstand the tension and became disconnected. This finding has huge implications for the use of biomechanical forces in promoting axonal growth for tissue transplants in patients with spinal cord and nerve injuries.[106] It also has great significance for us to understand the axonal-dependence on mechanical tension during development as the limbs grow.

Micro-technologies: Ahmed and colleagues described a flexible substrate made of polydimethylsiloxane (PDMS) to facilitate application of tension and compressive strains up to 45% to neural cells and tissues.[107] The substrate was clamped and could be subjected to biomechanical forces by controlling the integrated linear actuator. Using this platform, the authors found that *Drosophila* motor neurons actively contracted their axons and they hypothesized that internal tension might be present in axons that account for axonal development and synaptic plasticity.

3D microfluidic chambers and wells have also been created for neuronal seeding and growth.[108] Using surface patterning and fluidic resistance, axons can be preferentially separated from the dendrites, hence creating a model to study axonal growth, injury and recovery.[45,109,110] Nguyen et al. utilized a vacuum-supplemented microfluidic channel array that models an array of

micropipette tips to apply mechanical tension to seeded neurons.[111] It was found that applying tension to the neurites enhanced their typical growth rates by 2-12x. The team also supplemented the observation with a model based on microtubule dynamics to demonstrate how biomechanical forces can affect the polymerization and de-polymerization of microtubules and subsequently, neurite growth.

As the technique of vacuum and valve-based aspiration to induce axonal injury does not allow reproducible injured sites,[44,109] Hellman and co-workers developed a microfluidic platform that employed pulsed laser beam irradiation to produce partial and complete dissection of axons with high special control (**Fig. 4B**).[45] The group found that axonal recovery was initiated within 1-2 h post-injury and that recovery was initiated at the proximal side of the axon i.e. closer to cell body. Furthermore, while the inhibition of calcium influx reduced the severity of axonal degeneration, it also delayed recovery, suggesting the tight regulation of calcium second messenger for axonal recovery. Guo et al. have also applied a similar system that employed femtosecond lasers to dissect the axons of *C. elegans* so quickly that it did not induce any behavioral changes in the worms[112] as compared to other methods involving immobilization with carbon dioxide and compression.[113]

Kilinic et al. combined microfluidic chambers with magnetic tweezers to tow axons towards axonal repellents with low forces of ~ 15 pN (**Fig. 4C**).[114] The inhibition of kinesin-5 motor promoted axonal towing on surfaces coated with axon repellents, suggesting the possibility of using mechano-chemical stimulation for nerve repair such as in a glia scar environment that overexpresses axonal repellents.[115] Gu and colleagues integrated nano-pumps into microfluidic culture to create cross-flows and found that the direction of fluid flow could influence axonal migration and cause axonal turning with an angle more than 90^{o} (**Fig. 4D**). [116] This platform is

useful to study the impact of biomechanical forces due to flows on axonal growth especially on mechano-sensory neurons.

Nano-technologies: Making use of a micro-fabricated chips with engineered magnetic gradients, Kunze and co-workers showed that magnetic forces due to internalized MNPs can influence the distribution of tau proteins that can affect neurite polarization for axon formation.[54] Single cortical neurons experiencing forces in the range of 4.5-70 pN bias their tau protein assembly opposite to the patterned poly-L-lysine while a larger force range of 190-270 pN was needed for clusters with 6 neurons or more. At forces above 300 pN, magnetic field-induced displacements were observed. These findings hint at the potential of mechanically driving the polarization of neurons for nano-therapeutics.

The research findings described in this section demonstrate huge potential for integration of micro- and nano-technologies for repairing injured axons. One possibility is to use microfluidic chambers for engineering nervous system tissues while magnetic nanoparticles are employed to initiate neurite outgrowth and enhance the growth rate of neurites in a desired direction. Various magnitude and frequency of mechanical forces can be exerted to model forces experienced by neurons in different periods of developments and injury such as breakage of nerves in the spinal cord. Additionally, magnetic forces which are non-invasive may also be used to stimulate neurons with different magnitudes of forces to better guide the recovery of patients with spinal cord injuries.

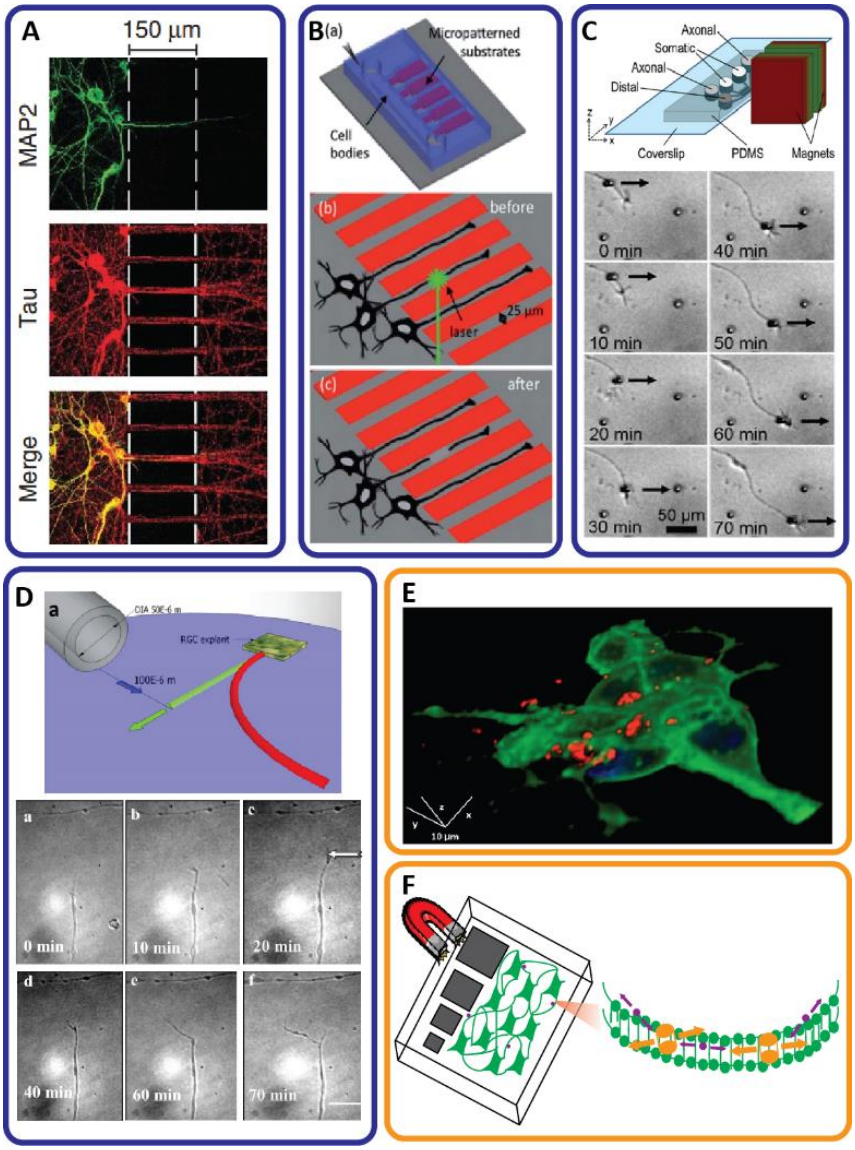

Fig. 4 **Micro**- and **nano**-technologies for probing mechano-biology of the brain. (**A**) A 3D microfluidic platform designed to direct axonal growth. As axons typically grow faster than dendrites, a barrier length can be established to isolate axons (TAU stained) from dendrites (MAP2 stained). Reproduced with permission from [41]/Nature Publishing Group. (**B**) Pulsed laser is used to sever axons patterned onto micro-channels to create a model of acute axonal injury. The laser-induced damage can be controlled for its intensity, spatial and temporal specificity. Reproduced with permission from [45]/ Nature Publishing Group. (**C**) Top: schematic of using magnet to tow axons bound to magnetic nanoparticles functionalized with neural cell adhesion molecule (NCAM). Bottom: example of axon towing with picoNewton (pN) force. Reproduced with permission from [114]/Creative Commons license. (**D**) Top: schematic showing that forces due to fluidic flow can influence axonal growth direction (green: initial direction, red: outgrowth direction). Bottom: example of axon turning due to fluidic forces. Reproduced with permission from [116]/ Creative Commons license. (**E**) Ultrasound stimulation can transduce mechanical perturbations into electricity generation with barium titanate nanoparticles with piezoelectric properties. This technology shows promise for remote trigger of calcium influx in neurons. Reproduced with permission from [60]/ American Chemical Society. (**F**) Nano-magnetic forces can activate mechano-sensitive N-type calcium channels to trigger calcium influx into neural networks seeded onto micro-fabricated substrate with steep magnetic gradient. Reproduced with permission from [58]/ American Chemical Society. Reproduced with permission from the Royal Society of Chemistry.

1.3.4 Regulation of circuitry and plasticity

The connectivity of neuronal systems is influenced by axonal branching, retraction and elimination.[117] Axonal branches enable an axon to establish synapses with dendrites of multiple neurons for communication. Mechanical forces have been proposed to influence axonal branching and pruning.[118] Anava et al. cultured invertebrate neurons on carbon nanotube (CNTs) islands and found that neurite elongation was enhanced when there was attachment to the CNTs and the lack of attachment resulted in axonal retraction or elimination.[8] Using vector equilibrium, the team found a high correlation between the calculated tension and diameter of the neurites. This study showed that tension-induced selection of axons might play a role in determining brain circuitry and networks.[7] Microfluidic chambers and nanoparticle-mediated tools as mentioned in **section 3.3** can be coupled for neuronal circuitry studies. However, in this case, the focus of the analysis would be the neuronal networks instead of individual neurons. One interesting areas of further investigation is whether enhanced mechanical tension in one axon affect the axonal/dendritic health or fate of the connecting neurons. For such a study, the physics of force equilibrium will be useful to determine the distribution of mechanical load. This area of research can be extremely meaningful as the paradigm for neuroscience shifts from individual neurons to neural networks.[74]

1.3.5 Regulation of brain folding

The brain consists of distinct anatomical sub-regions, and cortical folding or gyrification is responsible for the large surface area (~1600 cm^2) of the human brain as compared to its volume (~1400 cm^3).[119] Since the late nineteenth century, Wilhelm His has investigated the folding of cerebral cortices.[120] The characteristic shape of the cortical convolutions were demonstrated via simulations to minimize axonal tension and affect the thickness of different cortical layers.[120,121]

Furthermore, biomechanical forces during cortical development could account for larger numbers of neurons in the gyrus (convex folds) as compared to the sulcus (concave folds) and variations in cellular morphologies in different sub-regions that might influence cellular functions in these regions.[120] There is strong evidence supporting the relationship between improper cortical folding and brain-related diseases such as in lissencephaly (smooth brain disease characterized by the lack of folding, caused by lack of neuronal migration during development) and polymicrogyria (presence of excessive number of small gyri on the brain surface) that are associated with cognitive impairments and mental retardation.[122] Using magnetic resonance imaging, it has been observed that children suffering from autistic spectrum disorder suffer from cortical folding abnormalities[123] with increased frontal cortical folding[124] and cortical thickness[125] that can impact brain connectivity. Although research in this field has been performed for years, the exact mechanism for cortical folding is still unknown and there is a need for technological improvement to investigate the roles of biomechanical forces in brain development at the highest tissue level length scale. Recently, Tallinen et al. demonstrated that in addition to the influence of genetics and biochemistry on brain folding, the size, shape, placement and orientation of the folding in brain can arise through iterations and variations of the brain geometry in early fetal brain developments.[126] This new piece of evidence strongly supports previous findings that biomechanical forces play an important role in brain developments[127,128] and related diseases.[129] Interested readers can refer to Bayly et al.[119] and Silvia et al.[130] for greater details mechanical models of brain development.

Micro-technologies: Microfluidic chambers are ideal for investigating the impact of biomechanical forces on cortical misfolding and brain injuries due to their preferential properties such as laminar perfusion, efficient exchange of nutrients and waste products and high

spatiotemporal control for brain slice studies.[15] It is known that seizures and cortical spreading depression originate and spread from a specific region.[131] Mechanical forces can thus be applied focally to a target region with subsequent monitoring of downstream effects such as tensions applied by adjacent tissue, calcium influx and release of neurotransmitters. The brain slices can even be maintained in microfluidic chambers patterned with microelectrode arrays to perform on-chip electrophysiological recordings[132] following induced mechanical perturbation or injury. Micro-technologies offer spatial control and higher brain slice viability compared to conventional slice cultures or chambers that do not allow easy or reproducible investigation of biomechanical forces on brain folding. Making use of microfluidic chambers with designed 3D topographies that recapitulate structure in the gyrus and sulcus of various dimensions, neuronal migration and axonal tensions may be monitored over time. This platform can overcome the limitation of using rodent brains which have no folding and where brain tissue slices are often too thin to have noticeable folding. It may also be useful to understand how the ridges and depression in the cortices affect neuronal connectivity and communication. This configuration of microfluidic platform is not only useful to study the effects of biomechanical forces on brain development but also embryonic growth that still remains largely unknown.

1.3.6 Traumatic brain injuries

Traumatic brain injuries refer to brain damage attributed to external mechanical force such as during a crash or concussion. Traumatic brain injuries are graded as mild, moderate and severe on the basis of the level of consciousness after resuscitation.[133] Mild traumatic brain injury is usually accompanied by full neurological recovery; moderate traumatic brain injury leaves the patient

feeling lethargic; severe traumatic brain injury can cause the patient to be comatose and unable to follow commands.[133]

Conventional: Ellis and co-workers made use of a pump to apply pressure to astrocytes seeded onto flexible silicon membranes to create a model of rapid stretch-induced injury.[134] PC12 cells, although a poor model for neurons, were also subjected to horizontal oscillation to induce shear stress injuries.[135] It was found that injury induced swelling in the neurite terminals and the detachment of growth cones. This resulted in disruption to the cytoskeleton and inability to maintain cell shape. Lusardi et al. also made use of neurons plated on flexible substrates followed by a pneumatic pressure pulse to investigate the effects of mechanical stretching on a fraction of cells on the un-stretched cells with concurrent monitoring of acute calcium influx propagation.[136]

Micro-technologies: Microfluidic devices have been designed to survey the mechanisms governing the fate (recovery or death) of neurons suffering from mechanical damage. Magdesian combined microfluidic micro-channels with AFM and found that rat hippocampal neurons could recover axonal transport with no degeneration of axons when compressed with a pressure of 65 ± 30 Pa for 10 min while dorsal root ganglia (DRG) neurons could resist pressure up to 540 ± 220 Pa.[137] The authors attributed the higher resistance of DRG neurons to compressions to the lower elasticity (20%) of their axons which allowed the axons of the DRG neurons to accommodate greater stresses. The finding is also aligned to a previous finding on the mechanical heterogeneity of the brain which may be connected to their susceptibility to mechanical damage and recovery.[138] Maneshi and co-workers also designed a microfluidic chamber capable of applying shear stress using a fast pressure servo.[139] It was found that shear forces could induce a rise in intracellular calcium levels in astrocytes and the rise was cumulative and had a force threshold. Treatments with different chemicals also revealed the source of calcium to be from the extracellular

environment such that the calcium level rise was probably due to either transient micro-pore formation in neural membranes allowing ion influx or activation of mechano-sensitive ion channels (not specified by the authors). The different configurations of the micro-channels described in **section 3.3** have already been used to explore the role of mechanical forces in traumatic brain injuries and recovery from injuries at the single-cell and network level. Furthermore, microfluidics has been employed to study neurons in immobilized *C. elegans* as a model for brain injury.[140]

Table 3 Glossary of technical terms used

Glossary	
Ligand gated ion channels Transmembrane ion channels that allow ion passage in response to binding of a specific chemical molecule such as a neurotransmitter i.e. endogenous chemical that allow neuro-transmission	Viscoelastic Non-Newtonian material that exhibits both viscous and elastic properties and the strain is a function of time with applied stress
Neurites Axon and dendrites of a neuron	Maxwell materials Materials with both viscous and elastic properties
Dendritic spine plasticity Dynamic changes in the shape, volume and number of spines (membranous protrusions from dendrites that form synapses with axons) within hours	Catastrophic de-polymerization Dynamic instability of microtubules that causes sudden change from growing to shrinking states
Axonal growth cone Terminal of a neurite seeking synaptic connections	Nanoparticles Particles in the size range of 1-500 nm
Cargo transport Transport of materials/cargo such as proteins and lipid between the cell body and axon	Towing (axons) Pulling of (axons) in a certain direction with external forces on a surface
Dendritic spine morphologies Membranous protrusions from dendrites with mushroom, thin and stubby morphologies	Ferromagnetism Materials with high susceptibility to magnetization and persistence of magnetic properties after magnetic field removal
Synapses Junction between an axon (pre-synaptic terminal) and dendrite (post-synaptic terminal)	Piezoelectric Electrical charge stored in materials in response to mechanical stresses

1.4 Conclusions

Research over the past 40 years has supported that biomechanical forces are essential for proper brain development. Biomechanical forces can influence gene expression, modulate synaptic activity, affect axonal initiation, lengthening and recovery, and brain folding. Besides its roles in development, biomechanical forces also play a part in diseases such as when there is over-sensitization of mechano-sensory neurons, cortical disorders where there are abnormalities in cortical folding and in recovery from traumatic brain injuries. While conventional tools have been extremely useful in validating the mechano-sensitivity of ion channels and neurite outgrowths, their utility is limited in studies requiring better spatiotemporal resolution and throughput. Micro- and nano-technologies and combined platforms as we have described here offer much higher spatiotemporal resolution, enhanced throughput, possibility of potential co-cultures and remote control that are useful for studying the effects of biomechanical forces on brain development and related diseases, and potentially applying forces at the right place and time to mitigate disease in the future. In the following **chapter (2)**, I will describe how I make use of nano-technologies to elicit calcium influx in neural networks. Indeed, there are many questions that remain unknown such as the role of biomechanical forces in differential regulation of gene expression and the relationship between biomechanical forces and brain folding. However, advances and continual improvements in micro- and nano-technologies can enable exciting investigations to answer these fundamental questions that have emerged in the neuroscience discipline since the late nineteenth century.

Chapter 2: Acute Neural Stimulation

2.1 Introduction

In the previous chapter, I discussed the advantages of using nano-technologies to probe the mechano-biology of the brain. In this chapter, I describe the development of a magnetic micro-fabricated substrate and magnetic nanoparticles technology to induce calcium influx in neural networks by enhancing the opening probability of mechano-sensitive N-type Ca^{2+} channels.

As a second messenger in a plethora of signaling pathways, spatial and temporal variation in intracellular calcium (Ca^{2+}) influxes have been shown to induce gene transcription, influence mRNA translation and even post-translational protein modification[141]. However, in order to act as a specific second messenger, cytoplasmic Ca^{2+} concentration is maintained at a much lower concentration (100-300 nM) compared to extracellular spaces (1-3 mM) and endoplasmic reticulum (10-100 μM)[56]. To spatially and temporally activate signaling in cells, there is thus significant interest to manipulate Ca^{2+} levels, especially in neurons where Ca^{2+} dynamics within dendritic spines are associated with synaptic plasticity in neural networks[142], learning and behaviors[57].

Intracellular Ca^{2+} concentrations have been controlled with electricity, chemical stimulation, ultrasound, heat and even light[92]. The earliest attempts to control Ca^{2+} levels in neurons employed electrodes and chemical delivery systems that allowed temporal control but were unable to provide localized stimulation to densely packed neural tissues[143]. Ultrasound stimulation of ion channels can remote trigger calcium influxes although it is still largely limited by its non-specificity (space and time) on the neural networks and its potential side effects of heating[60,144]. The progress in optogenetics has demonstrated the utility of light to activate photo-sensitive ion channels in neurons specifically[143,145,146]. Nonetheless, these techniques necessitate

complex modification of exogenous genes to express photo-sensitive ion channels or the delivery of photo-sensitive ligand to specific receptors on neurons which are either irreversible or require a long time for effects to diminish. Optical approaches in general are still limited by the poor penetration of visible light into deep tissues and its resolution hinges heavily on the precision of the optical fibers used for light delivery[147].

Magnetic fields are ideal for non-invasive manipulations as they can achieve deep tissue penetration and localization by tuning force-inducing field gradients. To overcome the weak interaction between magnetic fields and biological molecules, magnetic fields should be translated into mechanical forces or torques[148,149] such as during Magnetic Resonance Imaging (MRI) in the latter case. One way of achieving this is through ferromagnetic nanoparticles (MNPs) that bind to cell membrane receptors or are internalized into the neurons followed by subsequent exposure of the neurons to magnetic field gradients.

Huang et al.[80] and recently, Chen et al.[81] made use of low-radiofrequency alternating magnetic field-induced heating to stimulate the opening of temperature-sensitive ion channels (TRPV1) in rat neurons. Although high amplitude Ca^{2+} influxes were observed in the latter case, Chen and co-workers did not comprehensively investigate the effects of sustained heating, heating due to internalized MNPs and heat diffusion to non-targeted sites at noxiously high temperature of 43 ^{o}C. The use of this technique for therapeutic treatments of human neuro-diseases may also face several challenges: (1) non-specific activation due to various endogenous chemical agonists such as lipoxygenase products[92] to mammalian TRPV1 receptor and (2) potential complications with viral delivery agents and gene therapies.

Very recently, Marino et al. also demonstrated the use of ultrasound to activate piezoelectric nanoparticles to induce Ca^{2+} influxes in individual neurons differentiated from

human neuroblastoma-derived cells[60]. However, in their technology, there was no indication that the Ca^{2+} influxes were propagated in the neural network. As the neural network paradigm gains traction and importance for the investigation of brain-related activities[74], it is important to demonstrate the propagation of Ca^{2+} influxes in neural networks to better predict *in vivo* behavior. In addition, although there were some cases of high Ca^{2+} influxes, the heterogeneity in sizes of differentiated neurons complicates the fluorescence quantification[73]. Essentially, larger cell bodies are expected to have larger Ca^{2+} influxes and vice-versa. Lastly, while ultrasound technology is improving, its poor penetration though the human skulls can limit downstream application of this technology[72].

In summary, an ideal method for remote stimulation of neural network should be non-invasive, safe under long duration exposure, spatially and temporally controllable and with different degrees of activation.

Previous studies have shown that internalized MNPs can stop neurite outgrowth with forces in the low pico-Newton (pN) range[150]. Our group demonstrated that localized mechanical stimuli due to magnetic fields can alter intracellular distributions of the microtubule-associated protein tau[54]. Related work using magnetic force was also presented by Etoc and colleagues[151]. Additionally, MNPs have reportedly affected gene regulation, Ca^{2+} influx[152] and lowered threshold and duration of action potential[153]. These observations suggest that low pN range mechanical forces induced by magnetic fields may be capable of influencing signal transduction in neurons. However, the technical difficulty of performing electrophysiological recordings with magnetic force stimulation has not allowed the mechanisms giving rise to Ca^{2+} influx to be investigated.

Here, we demonstrate that nano-magnetic force stimulation with MNPs could induce Ca^{2+} influx within *in vitro* grown cortical neural networks and heighten the magnitude and frequency

of intracellular Ca^{2+} waves. Stimulated cortical neural networks showed an average 20% increment in Ca^{2+} fluorescence signals, with the effects having a spatial resolution of 200 μm. Additionally, inhibition of Ca^{2+} influx in the presence of nano-magnetic forces by ω-conotoxin, an N-type Ca^{2+} channel inhibitor, implicated mechano-sensitive ion channels as responsible for Ca^{2+} influxes. Our findings support the hypothesis that magnetic forces can induce Ca^{2+} influxes that would likely mediate the growth of neurite[154] and intracellular distribution of proteins[54,155] and suggest the use of wireless magnetic forces to remotely modulate neural network activity.

2.2 Results and Discussions

2.2.1 Experimental set-up

Primary dissociated cortical neurons were plated onto poly-L-lysine (PLL, 20 – 100 μm) stripes on a neuro magnetic chip that guided network growth during culture (**Fig. 1a – 1b**). Two-week old cortical neural networks were then incubated with MNPs and stimulated with nano-magnetic forces within an engineered magnetic field of 150 mT maximum strength (~ 110 mT at the chip surface about 1 μm above the permalloy elements as characterized previously in [54]). The dimensions of the magnetic elements in combination with the observed cluster size of MNPs exert forces in the pico Newton range (**Fig. 1c**). Fluorophores were used to monitor Ca^{2+} fluctuations in the cortical neural network followed by data analyses (**Fig. 1d**).

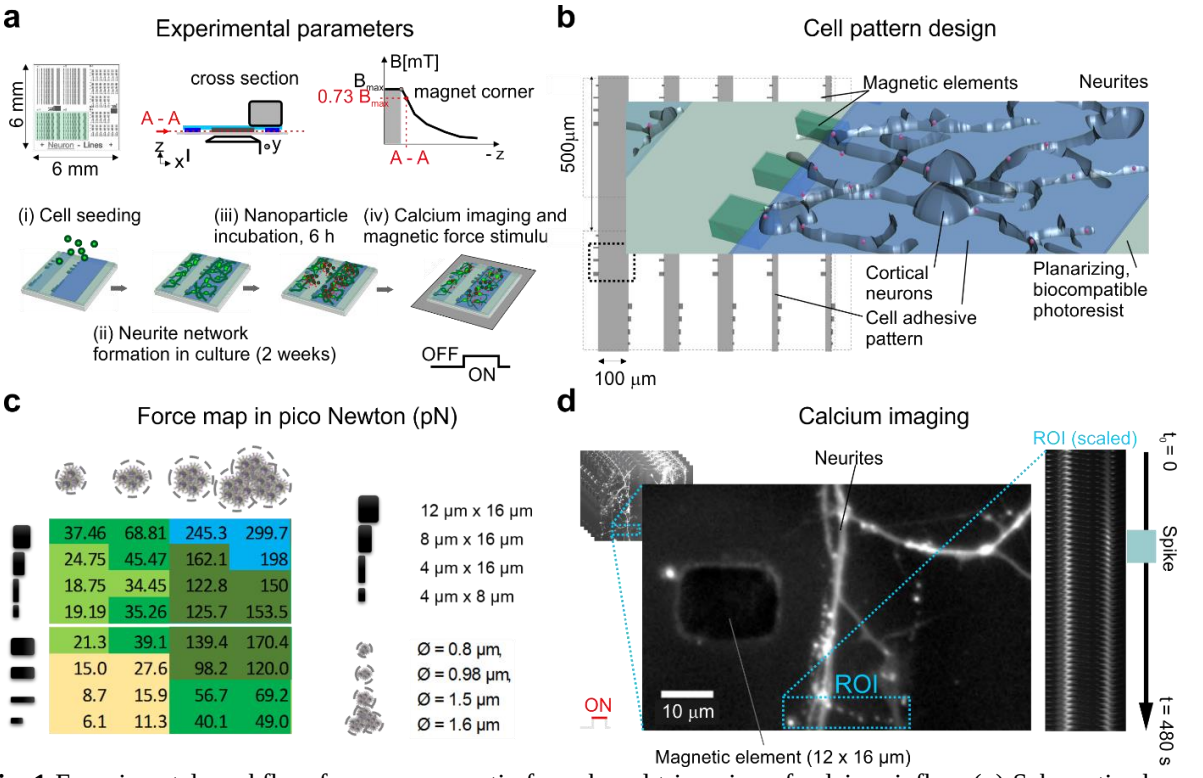

Fig. 1 Experimental workflow for nano-magnetic force-based triggering of calcium influx. (**a**) Schematic shows chip dimensions, experimental setup, applied magnetic field approximation (B_{max} = 150 mT: ON, B: 0 mT: OFF). At 1 µm above the permalloy elements, the magnetic field strength is ~0.73*B_{max} = ~110 mT as determined by monitoring movements of magnetic microparticles in applied magnetic fields. The workflow is composed of: (i) Seeding of neuronal cell (830,000 cells/cm^2) on spatially controlled cell adhesive patterns (PLL/Pluronics) on the magnetic chip, (ii) Formation of neurite networks over two weeks in culture, (iii) Incubation with ferromagnetic nanoparticles (MNPs, 54,000 x 10^6/mL) for 6 hr followed by subsequent washing and (iv) Loading with calcium dye (fluo-4) and stimulation with a permanent magnetic field (B_{max}: 150 mT). (**b**) Cell adhesive pattern design of 100 µm, 50 µm, and 20 µm width lines allows neurite network growth adjacent to magnetic elements on the magnetic chip over two weeks. Repetitive pattern design (here 500 µm spaced) supports parallelization of experiments (**c**) Force map shows estimated peak magnetic forces at 1 µm distance above the magnetic elements in combination with four different fMNP cluster diameters.[54] (**d**) On chip image acquisition of calcium activity (fluo-4 with probenecid acid). Extracted fluorescent signal from local regions of interest (ROI) exhibit stimulated calcium spike activity with starch-coated MNPs. Reproduced with permission from the American Chemical Society.

2.2.2 Characterization of starch and chitosan-coated MNPs

Starch-coated and chitosan-coated MNPs were used for this application due to their commercial availability and previous uses in neural-related applications with low cytotoxicity (**Appendix A Table 1**). The hydrodynamic sizes of the MNPs measured in conditioned media through dynamic light scattering were 209 ± 9 nm (starch) and 588 ± 31 nm (chitosan). The polydispersity index was similar for both MNPs in the range of 0.200-0.210. The zeta-potentials were -30.9 ± 2 mV

(starch) and -21.0 ± 7 mV (chitosan), highlighting high stability of the dispersion (**Appendix A Table 2**). We characterized the properties of the MNPs in conditioned media as we believe that cells can actively secrete molecules into the media or deplete molecules from the media in response to added nanoparticles. This would thus modify the protein corona on the MNPs,[156] thus impacting interaction with membrane proteins, endocytosis and intracellular fate of the MNPs.[157] There is also now increasing evidence that protein coronas can predict the interactions between nanoparticles and cells more effectively than size and surface charge[156].

2.2.3 Location and uptake of MNPs

To better evaluate the interactions between cortical neurons and MNPs, we determined the uptake of MNPs by the cortical neural network though flow cytometry. Following 24 hr incubation, 34.8% of the cortical neurons had uptake starch-coated MNPs while 68.4% had uptake chitosan-coated MNPs (**Fig. 2a**). Although the former has a smaller hydrodynamic diameter, its zeta potential is more negative, possibly leading to increased repulsion with negatively charged cell membrane[158] and lower uptake.

However, we recognize that a major limitation in using flow cytometry is the inability to differentiate whether the nanoparticles are localized inside the cells, on the cell membrane or at other parts of the cell (such as soma and neurites).[157] Therefore, we depleted the energy of the cortical neurons with sodium azide to inhibit endocytosis, an energy dependent process.[159] The addition of sodium azide reduced endocytosis of chitosan-coated MNPs by close to 90% but had no significant effects on starch-coated MNPs (**Fig. 2b**). This meant that most starch-coated MNPs were not internalized by the cortical neurons but were instead associated with the cell membranes. On the other hand, chitosan-coated MNPs were internalized into the cortical neurons.

Next, we performed confocal fluorescence imaging to identify whether there was a preferential localization of the MNPs on any particular structure of the cortical neural network. This was because we hypothesized that the nano-magnetic forces might activate mechano-sensitive Ca^{2+} ion channels which are found in higher density along the neurites.[160] We found that chitosan-coated MNPs tended to be internalized along the neurites (**Fig. 2d**). On the other hand, starch-coated MNPs preferred to localize at the membranes (**Fig. 2c**). While the reasons for these localization behaviors are still largely unclear, it has previously been reported that chitosan can bind to CD44 receptors of cancer stem cells[161] and a similar receptor-mediated mechanism may be responsible where the neurites may present membrane receptors that can bind to starch.

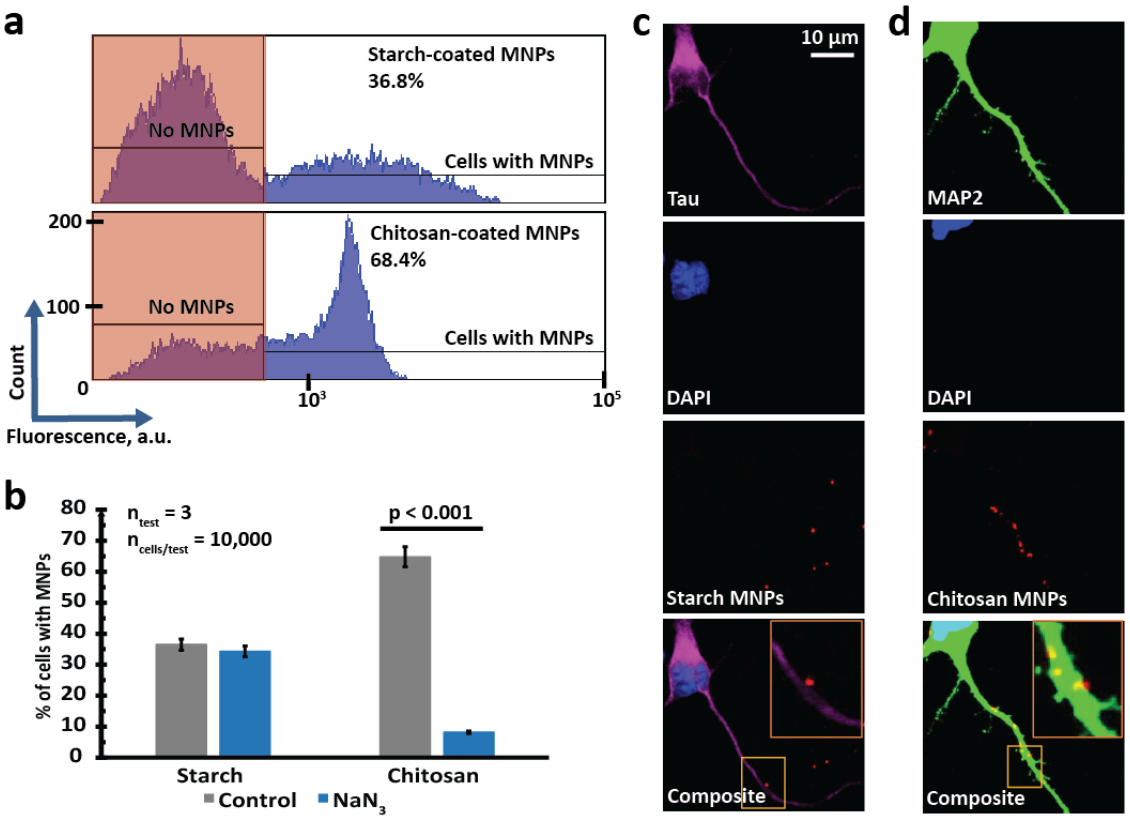

Fig. 2 Nanoparticles interacted different with cortical neural network. (**a**) Flow cytometry analysis showed that cortical neural network uptake less starch-coated MNPs than chitosan-coated MNPs. However, one limitation of flow cytometry is the inability to differentiate particles that are internalized or associated with the membranes. (**b**) Sodium azide (5 mg/mL) was added to inhibit endocytosis. Results from flow cytometry revealed that chitosan-

coated MNPs were internalized into cortical neural network *via* endocytosis but starch-coated MNPs were most likely associated with the membrane. (**c**) Fluorescent images confirmed that starch-coated MNPs were mostly associated with the neurites while (**d**) chitosan-coated MNPs were internalized and localized with lysosomes. Reproduced with permission from the American Chemical Society.

2.2.4 Nano-magnetic forces induce Ca^{2+} influxes

We first demonstrated that nano-magnetic forces could induce Ca^{2+} influx in cortical neural networks with starch-coated MNPs. The cortical neurons did not exhibit any significant change in viability even after incubation with the MNPs for up to 24 hr (**Appendix A Fig. 1**). Fluorescence intensity maps indicated that only cortical neurons stimulated with magnetic forces exhibited significant change in intracellular Ca^{2+} concentration (**Fig. 3a**). The $\Delta F/F_0$ (change in fluorescence over background fluorescence) for 30 selected neurons in different test conditions over 3 trials (color-coded) were plotted in **Fig. 3b**. In the presence of nano-magnetic forces, all the fluorescent intensity line traces were above background, with an average $\Delta F/F_0$ of 0.20. On the other hand, cortical neurons in all the other conditions without nano-magnetic forces did not exhibit significant deviation in their intracellular Ca^{2+} levels from the resting zero level. On closer examination, some fluorescent intensity line traces were below the resting zero level in the unstimulated conditions. This was due to the strong background fluorescence of the photoresist used for nano-magnetic chip fabrication and the limitation of bleach correction algorithm. Overall, 68% of the cortical neurons stimulated with nano-magnetic forces exhibited a $\Delta F/F_0 > 15\%$ while only ~3% of cortical neurons incubated with MNPs but without nano-magnetic force stimulation exhibited similar response (**Appendix A Fig. 2**).

To understand whether Ca^{2+} spiking was affected by the nano-magnetic forces, 40 neurons over 3 trials were selected from each test condition and their record of Ca^{2+} spikes over 5 minutes were tabulated with raster plots (**Fig. 3c**). Each cortical neuron was given an identity (ID) number

and their fluorescent intensities were traced over 5 minutes. We observed that nano-magnetic forces increased the frequency of Ca^{2+} spiking in cortical neurons much more significantly than all the other cases without nano-magnetic force stimulation. The number of spikes per cortical neuron at different time points (binned at 5 s) was also much higher in the stimulated cortical neural network (**Fig. 3d**).

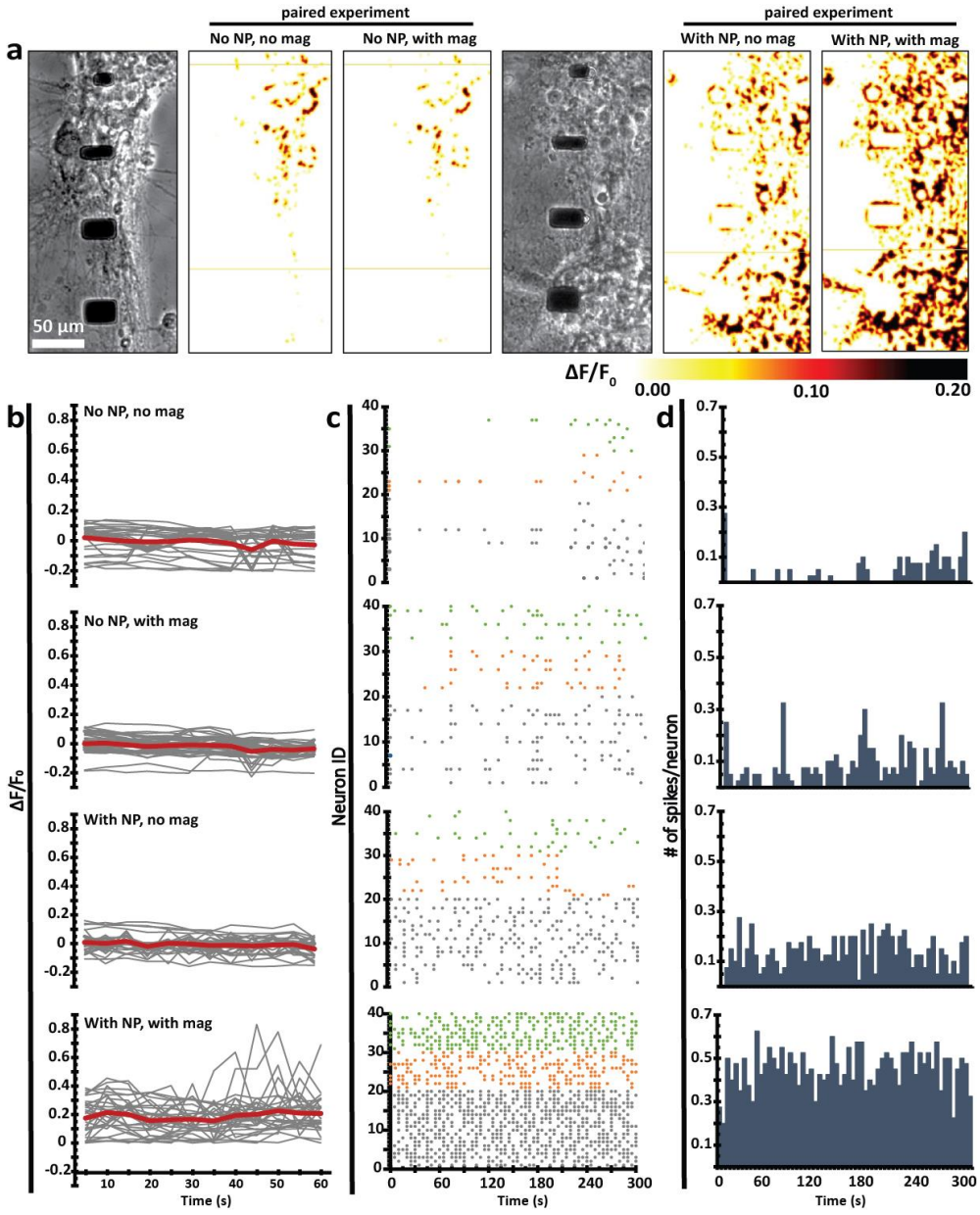

Fig. 3 Neurons that experienced nano-magnetic forces showed a larger change in calcium fluorescence intensity and spiking frequencies. **(a)** Color maps of fluorescence intensity change for different conditions. **(b)** Example fluorescence calcium concentrations ($\Delta F/F_0$) of 30 neurons for different conditions. **(c)** Raster plot of 40 neurons from three independent trials (1st trial: grey, 2nd trial: orange, 3rd trial: green). An increase in spiking frequencies were observed for neurons stimulated with nano-magnetic forces. **(d)** Peristimulus time histograms of the raster plots binned at 5 s. All experiments with and without MNPs were paired. Reproduced with permission from the American Chemical Society.

2.2.5 The location of MNPs affected the response of cortical neural networks to nano-magnetic forces

To determine whether the properties of MNPs could affect the response of the cortical neurons to nano-magnetic force stimulation, we also stimulated cortical neural network with chitosan-coated MNPs that tended to be internalized. Although a statistically significantly change in $\Delta F/F_0$ was observed with both chitosan and starch-coated MNPs (Student's t-test, $p < 0.05$) (**Fig. 4a-b**), $\Delta F/F_0$ in both cases differed by close to 9%. This difference could be due to the preferential localization of starch-coated MNPs at the cell membranes while the chitosan-coated MNPs tended to be internalized within intracellular compartments. More extensive interactions of starch-coated MNPs with membrane ion channels may result in larger Ca^{2+} influx.[152] It is also useful to note that in serum-free media like what we have used, nanoparticles were more likely to attach to the cell membrane, potentially allowing the MNPs to interact to a larger extent with membrane ion channels.[157]

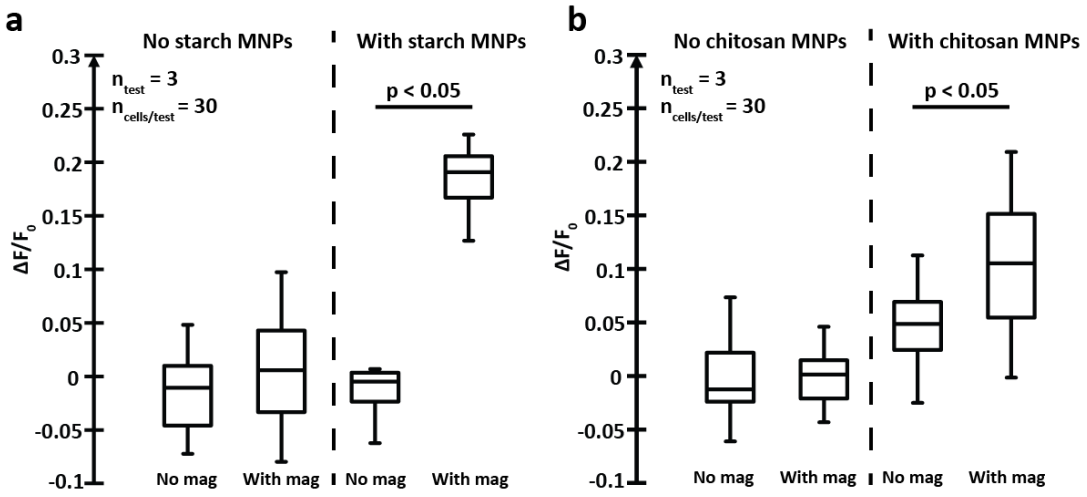

Fig. 4 Nano-magnetic force stimulation varies with functional-groups on MNPs. (**a**) $\Delta F/F_0$ (n = 360) indicated significant changes in calcium fluorescence intensity due to nano-magnetic forces from starch-coated MNPs. (**b**) $\Delta F/F_0$ due to magnetic forces from chitosan-coated MNPs was statistically compared to condition without nano-magnetic forces but had less effects than that for starch-coated MNPs. We hypothesize that the difference in the degree of activation might be due to the preferential localization of starch-coated MNPs at the membrane of the neurites. This might have increased interactions of MNPs with mechano-sensitive ion channels, giving rise to larger calcium influx. On the other hand, chitosan-coated MNPs tended to be internalized by the neural network and hence experienced less interactions with ion channels. Reproduced with permission from the American Chemical Society.

2.2.6 Mechanism of stimulation

We first investigated the source of Ca^{2+} influx and found that when extracellular Ca^{2+} was depleted with EGTA or when there was no extracellular $Ca^{2+,}$ the fluorescence signal was quenched whereas when intracellular Ca^{2+} was depleted with thapsigargin, there was only a delay in the increase in fluorescence intensities (**Fig. 5a**). This suggests that magnetically-induced Ca^{2+} influx was not G-protein mediated which typically involves release of Ca^{2+} from intracellular sources.[162] To further confirm, we also performed magnetic stimulation in the presence of 3 μM of bicuculline (EC_{50}), an inhibitor of γ-Aminobutyric ($GABA_A$) receptor which is expressed widely in the brain, and observed higher Ca^{2+} spiking frequencies in the neurons upon magnetic stimulation (**Fig. 5b**). These two experiments show that magnetically-induced Ca^{2+} influx was not modulated by G-protein and $GABA_A$ antagonist. We rationalized that if magnetic forces could increase $\Delta F/F_0$ in

the presence of bicuculline, it would also mean that magnetic stimulation did not inactivate inhibitory ion channels/receptors.

The next logical step was to determine if magnetic forces activated excitatory ion channels. We found that the amplitude of the magnetic forces (**Appendix A Fig. 3**) shared a skewed sigmoidal relationship to the Ca^{2+} fluorescence signals (**Fig. 5c)**. The amplitude of Ca^{2+} fluorescence signals is a product of the conductance (g), number density (N) and open probability (P_{open}) of the ion channel. In order to change the conductance of the ion channel, the permeation pore which is a highly conserved structure must be modified and structural changes usually result in blocking than enhanced permeability.[163] We also did not expect and observe any changes in the number density from acute stimulation as the time scale during stimulation (~5-10 min) is much less than the time (~ hr) needed for ion channel transcription/translation. Hence we reasoned that the applied forces enhanced the open probability of the ion channel, thereby facilitating Ca^{2+} influx which is supported by a previous studies.[164]

The sigmoidal relationship between force amplitude and calcium fluorescence signals has been previously observed in mechano-sensitive ion channels,[164] suggesting to us that magnetic forces might have activated mechano-sensitive Ca^{2+} channels especially concentrated at the boutons (**Fig. 5dii)**. This hypothesis was also motivated by our observation that starch-coated MNPs preferentially localized to the membrane rather than being internalized where the membrane-bound MNPs could have stretched the lipid membrane to open mechano-sensitive ion channels.

To show that our method of stimulation was not voltage-dependent, we first added 1 μM tetrodotoxin (TTX), a highly specific inhibitor of voltage-gated sodium channels involved in action potential propagation. We observed apparent stimulatory effects due to magnetic forces even with

TTX (**Fig. 5e**). We also administered 40 mM potassium ions (K^+) to induce action potentials and found that when magnetic forces were applied, there was still albeit a small increase in Ca^{2+} fluorescence intensity (**Fig. 5f**). Collectively, these two pieces of data suggest that our method of stimulation is not voltage-dependent.

As neurons express many types of mechano-sensitive ion channels (**Appendix A Table 3**), we thus attempted to identify the type of known channel that contributed most to the Ca^{2+} influx. We first inhibited the N-type mechano-sensitive calcium ion channels with a highly specific inhibitor i.e. ω-conotoxin GVIA (1 μM) and found that this completely quenched the stimulatory effects of magnetic forces (**Fig. 5g**). As L-type Ca^{2+} channel is reportedly mechano-sensitive but it undergoes rapidly reversible inhibition by ω-conotoxin GVIA,[165] we also performed a wash step, followed by subsequent monitoring of Ca^{2+} fluorescence signals. We did not observe any restoration of stimulatory effects of magnetic fields 10 mins after washing away the neurotoxin (**Fig. 5g**), suggesting that neural stimulation did not involve L-type Ca^{2+} channels.

We next performed magnetic stimulation at different temperatures and found that the $\Delta F/F_0$ was not heat-sensitive (**Fig. 5h**), hence ruling out that we are activating temperature-sensitive TRP ion channel which is also a major class of mechano-sensitive ion channel. This finding is also aligned with the knowledge that static magnetic field does not generate heat. The lower calcium influx at lower temperatures could be due to lower metabolism for uptake and intracellular trafficking of calcium indicators. Based on the literature review summarized in **Appendix A Table 3**, there are also a few other reasons why we believe we did not perturb TRP ion channels with magnetic stimulation: (1) TRP ion channels are mostly located on neurons in the dorsal root ganglion (DRG) where they play a role in touch/pain sensation while we cultured cortical neurons; (2) Chen et al. have shown that without genetically transfecting neurons to significantly increase

their expression of TRPV ion channels, there was no Ca^{2+} influx even with thermal stimulation;[81] (3) TRP ion channels possess intracellular Ankyrin domains that allow mechano-sensing by tethered channels and not the lipid bilayer model that we proposed.[166] One other class of mechano-sensitive ion channel that the magnetic forces might have perturbed is PIEZO2[82] which is a newly discovered ion channel without any specific inhibitor yet.[167] However, we reasoned that as they are mostly located on DRG neurons and have much lower expression in the cortices as compared to mechano-sensitive N-type calcium channels, their contribution to Ca^{2+} influx would be insignificant even if they were activated.

Lastly, we wanted to understand whether the age of neurons, which we have found to affect their interactions with MNPs,[168] could impact neural response to magnetic stimulation. We found that $\Delta F/F_0$ was lower for older neurons (**Fig. 5i**), possibly due to differences in ion channel expression such as reduction in expression of mechano-sensitive N-type Ca^{2+} channel with age.[169]

Together, our results support a mechanism whereby magnetic stimulation induced calcium influx through activating N-type excitatory Ca^{2+} channels which are mechano-sensitive. Our hypothesis is that the preferential location of starch-coated MNPs at the cell membrane could have led to membrane stretching and activation of these channels that are concentrated at the pre-synaptic terminals.

We, however, do not rule out the possibility that other mechano-sensitive ion channels might have contributed to the Ca^{2+} influx as there could be unknown ion channels or undiscovered properties of known ion channels. Furthermore, mechano-sensing either by conformational changes in the lipid membrane or by tethered channels might not be mutually exclusive[166] as magnetic forces might also indirectly induce cytoskeletal movements. Our argument is hence similar to thermo/magneto-genetics where it is expected that the applied heat or mechanical stimuli

might also activate intrinsic heat/mechano-sensitive ion channels.[170–173] Although there is a possibility that other mechano-sensitive ion channels might be activated by magnetic force-induced stretching of lipid membrane, we showed that the contribution by N-type Ca^{2+} channels was the largest (**Fig. 5g**). We understand that there is a possibility that the applied magnetic forces could activate excitatory mechano-sensitive TRPV4, PIEZO1 and NMDA receptors. Future work is needed to apply a consistent method to quantify the force sensitivity of these different channels/receptors to compare or construct a model. It has been shown that a force of 3 pN could enhance the opening probability of mechano-sensitive ion channels in the hair cells of ears through mechanical amplification,[174] suggesting that larger forces of 200-350 pN without amplification could be sufficient to generate the same effects on N-type Ca^{2+} channels present on each neuron. Recently, Wu et al. also found that a force of ~10 pN is needed to activate a single PIEZO ion channel. Consequently, the total force of 200 pN is only able to activate ~20 PIEZO ion channels which will be insufficient to generate the large calcium influx ($\Delta F/F_0$ = 20%) that we observed. Therefore, based on the expression density, location and responsive stimuli of the ion channels, we reasoned that it was most likely that magnetically-induced Ca^{2+} influx was largely through the N-type Ca^{2+} channels.

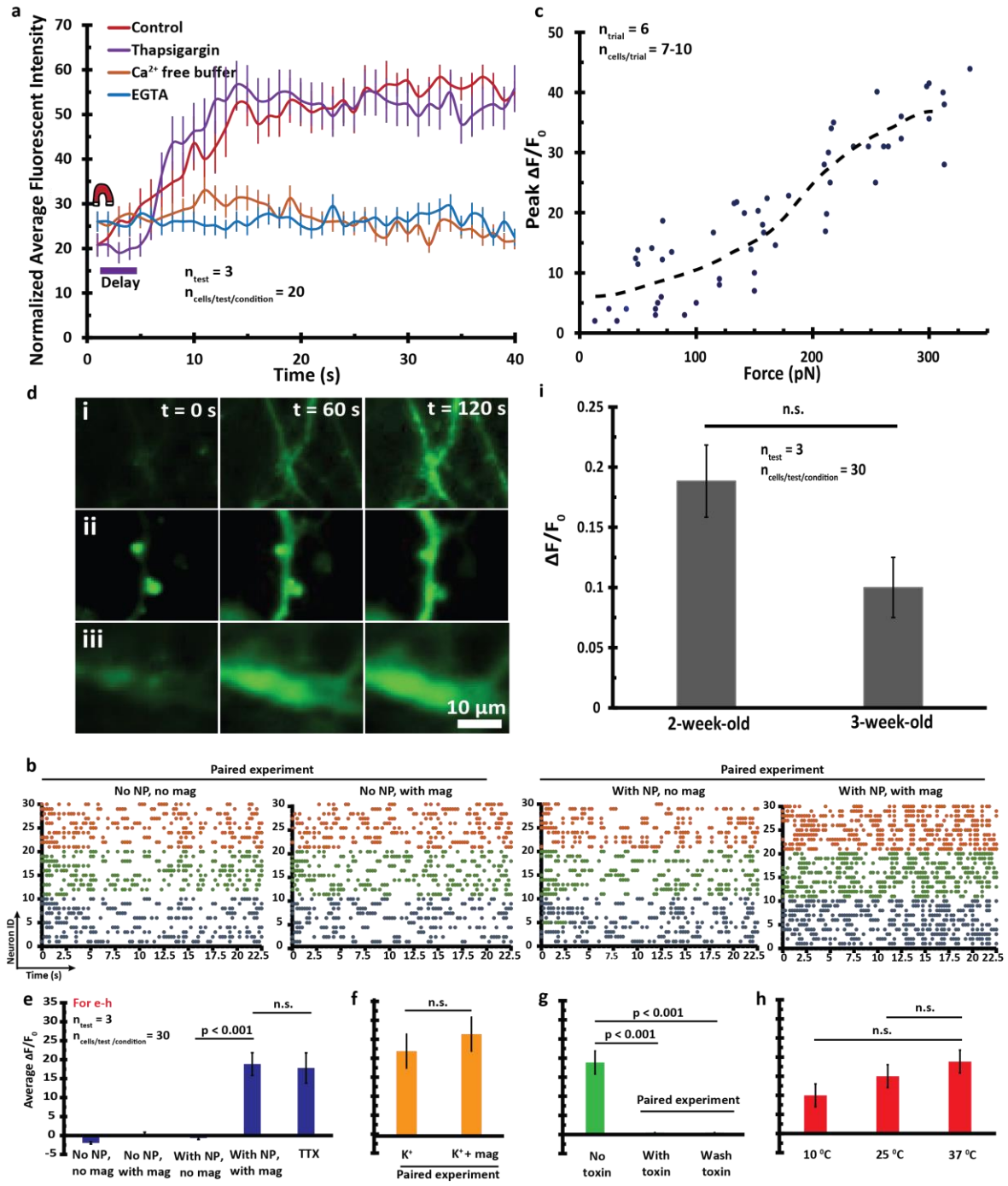

Fig. 5 Mechanism for magnetic stimulation of neural networks. (**a**) Magnetic stimulation leads to influx of calcium primarily from the extracellular environment. (**b**) Magnetic forces increased calcium spiking in the presence of bicuculline, suggesting that this technique is not neurotransmitter-mediated and does not inactivate inhibitory ion channels for calcium influx.) (**c**) The amplitude of the magnetic force shared a sigmoidal relationship to the peak $\Delta F/F_0$, suggesting the possibility of controlling stimulation dosage by changing the probability of ion channel opening. (**d**) Time-lapsed images show increase in calcium fluorescence signals in (**i**) dendrites, (**ii**) axonal boutons where pre-synaptic terminals are located and (**iii**) cell body. Magnetic stimulation induced ~20% increase in average $\Delta F/F_0$ even in the presence of (**e**) TTX and (**f**) K^+, showing that voltage-gated ion channels were not activated. (**g**) Inhibition with ω-conotoxin GVIA quenched calcium influx even after washing, supporting that mechano-sensitive

N-type calcium channels were involved. (**h**) Magnetic stimulations were not temperature-sensitive, hence ruling out the possibility of activating TRP ion channels which are heat/mechano-sensitive. (**i**) 3-week-old neurons experience less calcium influx with magnetic stimulation.

2.2.7 Lipid bilayer stretch model

There are currently two main models proposed for the gating process of mechanosensitive ion channels *i.e.* lipid bilayer stretch model and spring-like tether model[175]. In the lipid bilayer stretch model, mechanical stimulations of the lipid bilayer trigger conformational changes to the mechanosensitive ion channels, causing channels to open. In the spring-like tether model, a spring-like tether is associated with the mechanosensitive ion channels, and upon tether deflection, the channels will open. From **Fig. 2**, we observed that starch-coated MNPs preferentially localized at membranes but we did not observe their preferential localization along the axons where N-type calcium ion channels are mostly located[176]. Therefore, we ruled out the spring-like tether model where specific binding of starch-coated MNPs to proteins along the axons is needed for mechano-activation. A proposed model based on lipid bilayer stretching is shown in **Fig. 6** where nano-magnetic force stimulates the opening of mechano-sensitive N-type Ca^{2+} ion channels for Ca^{2+} influx.

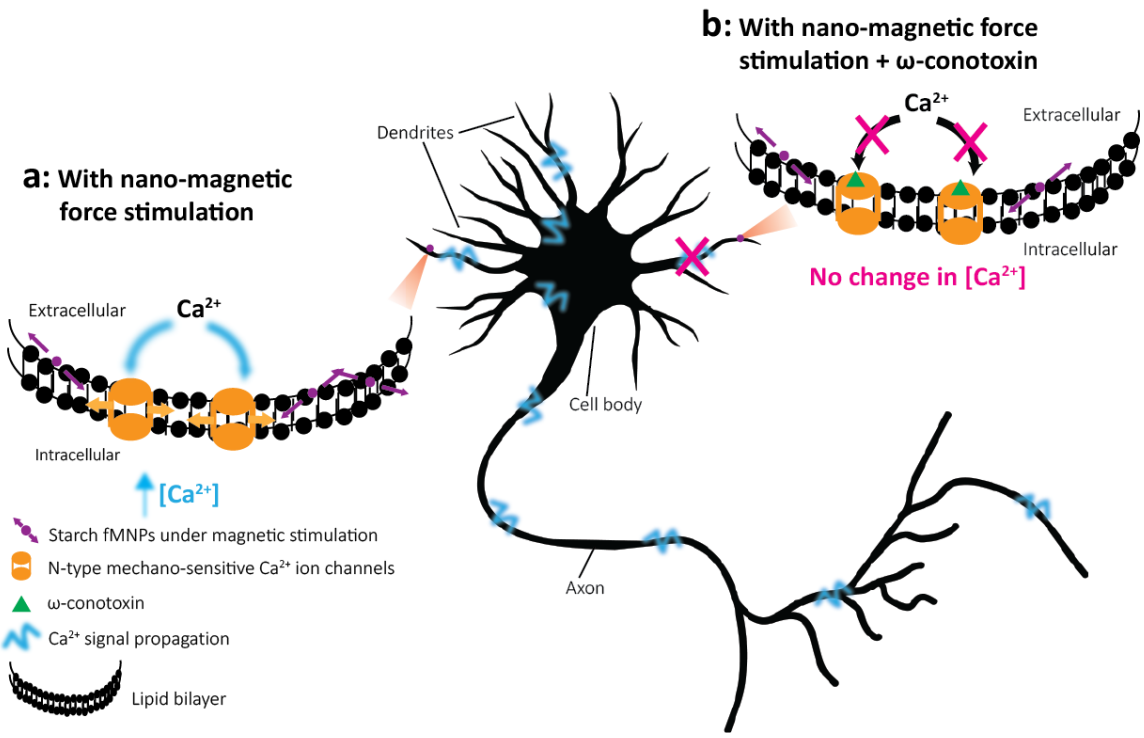

Fig. 6 Graphical illustration of proposed mechanism of nano-magnetic force stimulation. **(a)** In the presence of nano-magnetic forces, starch-coated MNPs localized at membranes could exert mechanical forces on the membranes, resulting in calcium influx through N-type mechanosensitive calcium ion channels. The calcium signals are then propagated through the neurons and throughout the cortical neural networks. **(b)** In the presence of ω-conotoxin GVIA, calcium influx is inhibited even with nano-magnetic force stimulation as N-type mechanosensitive calcium ion channels are blocked. Reproduced with permission from the American Chemical Society.

2.3 Conclusions

Biomedical applications of magnetic forces are becoming increasingly common. Magnetic forces have been reportedly used to improve transfection rates[177], gene therapy[178], stem cell differentiation[179] and tissue engineering.[180] For instance, Kriha *et al.* has previously described the production of electrospun fibers containing MNPs whose movements can be controlled to establish connections between hippocampal neurons to facilitate neural repair.[181] Similarly, Sakar and colleagues also utilized magnetic forces to manipulate the positions of neurons with micro precision and to deliver microgels to patterned neurons.[182] Xie *et al.* have also covalently linked nerve growth factor to magnetic nanotubes to induce differentiation in PC-12 cells.[183]

There are also a few other pieces of literature that directly described the effects of magnetic forces on neuronal growth and neurite development. Fischer *et al.* made use of MNPs conjugated with anti β-1 integrin to bind to neurons, followed by the application of magnetic forces to the neuron with a high gradient electromagnet.[184] Using this technology, the group better understood the force dependence of neurite initiation. They demonstrated the formation of synapses between axons and dendrites in about half the experiments with magnetic forces and found that as the neurons mature, it became increasingly less probable for magnetic forces to initiate neurite formation. Kim and colleagues also reported the use of static magnetic fields to elicit neurite outgrowth in PC-12 cells and the orientation of neurite growth was perpendicular to the direction of the applied magnetic field.[154] The team found that magnetic field could polarize the localization of actin and microtubules but did not change the levels of synaptotagmin responsible for synaptic formations. Nonetheless, in these papers, the authors recognize that they did not demonstrate a connection between signaling cascades and the reported morphological change in neurite outgrowth, which we attempt to answer in our piece of research.

From the work of Mannix and co-workers, the group demonstrated that nano-magnetic forces could be transduced into physiological cellular outputs.[185] Briefly, the team conjugated MNPs with monovalent ligands, allowing the MNPs to bind to membrane receptors on cancer cells. Nano-magnetic forces were then applied to aggregate the membrane receptors, resulting in elevated intracellular Ca^{2+} concentrations within 20 s after the magnetic field was applied. Nonetheless, this work could not be directly translatable to neurons which have different Ca^{2+} mediated signaling cascades as compared to cancer cells. Furthermore, the role of specific ion channels that elicit Ca^{2+} influxes was not investigated.

Utilizing tools from micro-fabrication and Ca^{2+} imaging, we demonstrate, to the best of our knowledge, the first time that nano-magnetic forces are able to induce Ca^{2+} influxes in cortical neural networks. We observed that the choice of coating on MNPs can affect their localization on the cortical neural network and subsequent strength of induction. Particularly, we saw that starch-coated fMNP had lower internalization than its chitosan-coated counterpart possibly due to its more negative zeta potential which is known to limit uptake.[158] Interestingly, the inhibition of endocytosis with sodium azide did not affect the uptake of starch-coated MNPs significantly, suggesting the possibility of this type of nanoparticle localizing on the cell membranes instead of being internalized, supported by our fluorescence imaging results.

We then compared the $\Delta F/F_0$ in Ca^{2+} signals of the cortical neural network between starch-coated and chitosan-coated MNPs and found that the former was able to elicit a larger response. We hypothesized that this could be due to more extensive interactions of the membrane bound starch-coated MNPs with membrane ion channels. To test our hypothesis, we inhibited the N-type Ca^{2+} ion channels with ω-conotoxin GVIA and found that even after washing away the toxin, the inhibitory effects were not rapidly reversible. These results supported our hypothesis that the applied nano-magnetic forces could be stimulating mechano-sensitive N-type Ca^{2+} ion channels[4] although other ion channels could be involved as well.[60] Nonetheless, based on the amplitude and the duration (in the minute scale) of the transients after nano-magnetic force stimulation, Ca^{2+} was most likely the main ion involved.[186]

In our work, we also demonstrated the remote activation of Ca^{2+} ion channels with high spatial resolution. Cortical neurons about 200 μm away from the magnetic elements did not experience significant change in intracellular levels. In human patients, the ability to spatially control the effects of magnetic field on Ca^{2+} influx may be achieved with precise implantations of

magnetic chips similar to common procedures for deep brain stimulation using electrodes.[187] The recent invention of an electromagnetic micro-needle actuator which even when placed externally, is capable of providing a high gradient magnetic field with deep penetration,[188] may remove the need for invasive implantations. Therefore, magnetic fields which are less attenuated by the body tissues compared to electric fields can provide greater efficacy in stimulating dysfunctional brain circuits.

The nano-magnetic force stimulation also elicited the propagation of Ca^{2+} influxes throughout the cortical neural network that was not demonstrated by recent work such as by Marino *et al.* who showed only a rise in intracellular Ca^{2+} levels in individual neurons.[60] The ability to demonstrate propagation of Ca^{2+} signals is significant as the neuroscience community increasingly advocates using neural networks instead of individual neurons as the paradigm for studying neuro-activities.[74]

Through extensive experiments, we also demonstrated that magnetic forces most possibly induced Ca^{2+} influx by mechanically stretching the lipid membrane to modulate the open probability of mechano-sensitive N-type Ca^{2+} channels. One of our future planned experiments is to perform single ion channel patch clamping with a customized non-magnetic recording apparatus to eliminate electrical noise from the magnetic field to better understand the effects of magnetic forces on channel conductance and probability of channel opening. One way to increase the specificity of acute stimulation with this technique is to coat the MNPs with antibodies targeting the N-type calcium ion channel as proposed by Souze et al.[189] although this might be incompatible with chronic stimulation as the functions of the ion channels might be adversely affected.

There are a few ways to boost the magnitude of Ca^{2+} influx to match findings reported in the literature for orthogonal techniques.[81] Firstly, as nanoparticle uptake is stochastic in nature,[190]

functionalized MNPs[191] can be used to target specific mechano-sensitive ion channels on neurons. For instance, MNPs with more negative zeta potential may localize better at negatively charged cell membranes[158]. Targeted MNPs may also provide a causal evaluation of the role of specific cells (excitatory *versus* inhibitory neurons) in the neural network. The same objective can also be achieved by increasing expression of N-type Ca^{2+} channels in the neurons similar to current practices in opto/thermogenetics or transfecting cells with constructs of genes encoding for magnetosomes from magnetotactic bacteria.[192] Next, steeper magnetic gradients or stronger magnets may find utility in inducing larger Ca^{2+} influx based on the observation that regions of neural network experiencing greater nano-magnetic forces also experienced greater $\Delta F/F_0$. Lastly, the use of ultrasensitive fluorophores such as GCaMPs[193] may also provide a better understanding on the time scale of the magnetic force-induced Ca^{2+} influx that were not captured by less sensitive fluo-4 and rhod-3 based fluorophores that we have used.

2.3 Materials and Methods

Fabrication of magnetic chips

Patterning of neurite networks was achieved on line shaped PLL/Pluronic cell adhesive/repellent surface coatings. PLL lines were designed to be 100 µm, 50 µm and 20 µm in width, adjacent to magnetic elements, which are embedded (1 µm deep) into a biocompatible photoresist and therefore shielded from the PLL surface. By monitoring the movements of microparticles, the magnetic field strength 1 µm above the magnetic elements is ~$0.73*B_{max}$ (applied magnetic field).[54] Fabrication of the magnetic chips is based on previously described protocol[54]. Briefly, fused silica wafers (d: 10 mm, University Wafer) were cleaned in piranha solution (4:1) for 30 min, and oxygen plasma (air, 100 ^{0}C, 200 W, 2 min). A 50 nm-Ti, 200 nm-Cu and 50 nm-Ti seed

layer was then evaporated onto the substrate. Microstructured SPR 220 photoresist formed 4 μm thick nickel-iron (NiFe, 80:20) alloys during electroplating. Residual titanium and copper layer was subsequently etched in 1% HF and copper etchant (5% acetic acid, 15% H_2O_2), respectively. The NiFe magnetic elements were passivated by 100 nm PECVD SiN and planarized by 5 μm of 1002F A second lithography layer (SPR 220-3) was performed on top of the planarizing 1002F4 layer to produce striped openings for cell adhesion patterning. Chips were stored at room-temperature shielded from light until further usage. Prior each neuronal cell seeding, opened 1002F structures were O_2 plasma activated (38 W, 45 s, 500 mTorr) and SPR 220-3 was removed through a 100% acetone rinse. A polymeric 0.05% (w/v) Pluronics, 25% (v/v) PLL in PBS solution was subsequently co-adsorbed to oxygen plasma activated surface, after 20 min UV sterilization for 16 h at 37 ^{0}C. Prior cell seeding, polymeric solution was aspirated, chips were washed with sterile water and culture medium (Neurobasal).

Cortical neural culture

Whole brain rats (E18, Brainbits) were transferred to PBS (33 mM glucose, 1% (v/v) Penicillin-Streptomycin (PenStrep from Gibco®), washed for 5 min and cortical hemispheres dissected[54]. Cortical tissues were then placed in Papain/Hibernate-E (pH 7.3, 10 % (v/v) Carica papaya, Roche) and dissociated for 15 min at 37 ^{o}C. 10% horse serum (Fisher Sci) in Neurobasal (Gibco®) was then added to quench the enzymatic activity of Papain and the dissociated tissues were triturated through a 1000 μL pipette tip and filtered a 40 μm cell strainer. Cell count was determined and 1 million cells were seeded onto each magnetic chip. After 2 hr of incubation (95% air, 5% CO_2, 37 ^{o}C), unattached cells were washed away with pre-warmed culture media.

Characterization of nanoparticle properties

ZetaPALS 90Plus particle size analyzer was used to determine the hydrodynamic diameter of the nanoparticles. Briefly, nanoparticles were suspended (54,000 x 10^6 nanoparticles/mL) and pipetted into a cuvette before measurement with a laser *via* dynamic light scattering. A smooth auto-correction/error function was obtained before data collection. Following which, the ZetaPLAS zeta potential analyzer with electrode probe AQ599 were used to determine the zeta potential of the nanoparticles. It is important to enter the right size of the nanoparticles to reduce fluctuations of the zeta potential readings.

Nanoparticle incubation

Cortical neurons were incubated with starch or chitosan coated fMNPs (Chemicell) for 2, 6 or 24 hr at 0.12% (v/v) in Neurobasal, 1% PenStrep, 1% GlutaMAX^{TM} and 2% B27 supplement. After which, the cells were gently washed for 3 times with Neurobasal media to remove excess of fMNPs. The fMNPs are composed of magnetite with either starch or linear chitosan randomnly distributed around the magnetite core. The density of the fMNPs is 1.25 g/cm^3. The size of the fMNPs according to the manufacturers is 100 nm. However, our measurement with dynamic light scattering shows that the hydraulic diameter of the fMNPs are in the range of ~200 nm (starch-coated) and ~400 nm (chitosan-coated). As fMNPs are also frequently used for localized heating, additional information on magnetic hysteresis can also be useful for readers. For interested readers: the TEM images and magnetic hysteresis curves of the iron oxide core can be obtained from Eggeman *et al.*[194]; the magnetic hysteresis curves of starch-coated and chitosan-coated fMNPs are also available from Cole *et al.*[195] and Kong *et al.*[196] respectively.

Calcium dye incubation and magnetic force stimulation

Cortical neurons were incubated with Fluo-4 Direct^{TM} calcium assay kit (Life Technologies) or Rhod-3 calcium imaging kit (Life Technologies) according to manufacturer's protocol with 5 mM stock solution of probenecid. Briefly, 5 mL of calcium assay buffer was mixed and vortexed with 100 µL of probenecid stock solution to create a 2x loading dye solution. The dye solution is then added to the cells with media in a 1:1 ratio and incubated for 1 hr before imaging. For magnetic force stimulation, calcium activity was monitored without a permanent magnetic field (OFF), and with a neodymium magnet (ON: B_{max} =150 mT, ½ inch x ½ inch x ½ inch, Apex Magnets) placed on top of an inverted chip. For experiments involving TTX (1 µM), K^+ (40 mM), ω-conotoxin GVIA (1 µM), thapsigargin (2 µM), EGTA (10 mM) and bicuculline (3 or 1.2 µM), the chemical was added during calcium dye incubation (1 hr). The use of EGTA is to completely chelate extracellular calcium. The method is to confirm that the source of calcium is from the extracellular environment as there is usually still some residual calcium from the neuronal media even after replacement with calcium free buffer. After imaging, the solution was replaced with fresh media and the cortical neural network was imaged again. For experiments involving ω-conotoxin GVIA, a wash step was also included to remove the neurotoxin and the neurons were imaged after 15 mins of waiting time.

Immuno-fluorescent labelling

Cortical neurons were washed with Dulbecco's PBS with magnesium and calcium (Gibco) and fixed with paraformaldehyde (4% v/v, Santa Cruz Biotechnologies), permeabilized with 0.1% Triton-x/DPBS and 3% BSA for 10 min and blocked with 3% goat serum in 1% BSA/DPBS. Primary antibodies were incubated overnight at 4 ^{o}C in 3% goat serum, 0.5% Tween-20 in 1%

BSA/DPBS and secondary antibodies were added. Finally 4',6- diamidino-2-phenylindole (DAPI, 300 nM in DPBS) was incubated for 15 min and additionally mounted on glass slides using pro ProLong ® Gold antifade reagent (Molecular Probes).

Cytotoxicity assay

Colorimetric MTT (3-(4,5-dimethylthiazol-2-yl)-2,5-diphenyltetrazolium bromide) assays were performed in 96 well plates where different functionalized fMNPs were added to each well seeded with cortical neurons. After each specific time interval, 20 µL of MTT (5 mg/mL) in PBS was incubated for 3 hr. Then the supernatant was aspirated and 200 µL of dimethyl sulfoxide (DMSO) was added. Each 200 µL sample in DMSO was spun down to remove MNPs in solution and the supernatant was read with a 96 well plate reader for absorbance at 550 nm.

Flow cytometry analysis

1.0×10^6 neurons were seeded in individual PLL-coated 12 well-plate (Corning) and allowed to grow for 2 weeks. Fluorescently labeled MNPs (green: ex (476 nm), em (490 nm); red: ex (578 nm), em (613 nm)) were then added at a concentration of 54, 000 x 10^6/ mL and incubated for 24 hr before triple washing with neural basal media. For experiment involving sodium azide, cortical neurons were also incubated with 5 mg/mL sodium azide solution for 24 hr. Neurons were then detached from plate surface using Accutase® (Stemcell Technologies, ref # A11105-01) for 10 min and centrifuge at 600 g for 6 min to collect the pellet. Cell pellet was then resuspended in 500 µL DPBS, stored at 4 ^{o}C and analyzed using BD LSRII flow cytometer at the UCLA Flow Cytometry Core Laboratory.

Image acquisition, analysis and statistical evaluations

Wide-field fluorescent and phase contrast images were acquired with an inverted fluorescent microscope (Nikon, 20x, 40x air, 60x air objective) or confocal microscope (Leica TCS SP5, 60x oil objective). The fixed and immune-stained samples were excited with 364 nm (blue/ DAPI), 488 nm (green/MAP2), 650nm (Cy5/TAU) and 532 nm (red/fluorescent fMNPs) laser lines.

Heat maps were generated with ImageJ plug-in HeatMap from Stack. Parameters (color min/max) were kept consistent for comparison of calcium fluorescence.

The relative fluorescence change $\Delta F/F_0$ of somatic fluorescence signals was acquired using ImageJ for all neurons within a particular trial. Calcium spike events were considered if they fulfilled two criteria: (1) the fluorescence increase was at least 5 standard deviation above baseline, which was defined as first 5 s of each trace and (2) if the event persisted more than 5 s. Raster plots were then generated from this method. Calcium videos were taken over 5 mins with a per frame period of 5 s.

Transmission electron microscopy (TEM) images of the starch-coated fMNPs were acquired with a T12 Quick CryoEM with exposure time of 0.5 s. Briefly, the starch-coated fMNPs ($45{,}000 \times 10^6$/ mL) were incubated with Neurobasal media for 6 hr and then centrifuged at 600 g for 6 min to collect the pellet. The pellet was resuspended in 50 µL deionized water. The starch-coated fMNPs were then adsorbed onto 400-mesh copper grid coated with carbon (Ted Pella Inc.). TEM was performed using 120 kV T12 Quick CryoEM with a point resolution of 0.34 nm. Imaging and data processing was performed at the UCLA CNSI Electron Imaging Center for NanoMachines (EICN).

Statistical significance in **Fig. 2b** was evaluated using Mann Whitney U Test with null hypothesis = 0 and n = 30,000 (3 tests, 10,000 cells/test). Statistical significance in **Fig. 5** and

Appendix A Fig. 1 was evaluated using Student's t-test after testing for normality using either one-way ANOVA, $p < 0.05$ (no rejection of normality), or nonparametric Kruskal-Wallis ANOVA, $p < 0.05$ (normality rejected) with n = 120 cells in **Fig. 5a** (3 tests, 4 conditions, 10 cells/test/condition), n = 120 cells in **Fig. 5b** (4 condition, 30 cells/condition), n = 42-60 cells in **Fig. 5c** (n_{trials} = 6, 7-10 cells/test), n = 60 cells in **Fig. 5e** (2 paired experiments, 3 tests, 10 cells/experiment), n = 30 cells in **Fig. 5f/g** (1 paired experiment, 3 tests, 10 cells/experiment), n = 60 cells in **Fig. 5h** (1 control and 1 paired experiment, 3 tests, 10 cells/experiment), n = 90 in **Fig. 5i** (3 conditions, 3 tests, 10 cells/experiment), n = 120 (2 conditions, 2 tests, 30 cells/test/condition) and n = 360 cells (4 groups, 3 trials and 30 cells/trial, n = 600 cells (6 test, 100 cells/test) in **Appendix A Fig. 1**.

Chapter 3: Chronic Neural Stimulation

3.1 Modulation of excitatory: inhibitory ion channel ratio in neurons with magnetic stimulation

In **Chapter 2**, I described the use of microfabricated magnetic substrate and magnetic nanoparticles for acute neural stimulation. Here, I explain how we employ the same tool for chronic magnetic stimulation for modulation of mechano-sensitive ion channel expression.

It is well-established that neurons in networks actively regulate their ratio of excitatory (such as N-type calcium channels) to inhibitory (such as GABA) ion channels/receptors to maintain activity homeostasis.[197–199] A suppression of activity leads to an increased number of excitatory ion channels/receptors in neurons while an enhancement of activity reduces the number of excitatory ion channels/receptors.

An off-balance ratio of excitatory to inhibitory ion channels/receptors has been observed in various neurological diseases[200] such as chronic pain and FXS, a human intellectual disability classified under the autism spectrum disorder.[201] The fragile X mental retardation protein (FMRP) increases the density of N-type Ca^{2+} channels, causing hyper-excitability.[202] The disease is also characterized by a deficiency of GABA receptors at the cortices of Fragile X mice,[203] contributing to epilepsy.[204]

We hypothesized that if our magnetic platform could activate excitatory N-type Ca^{2+} channels chronically, the neural networks might compensate by reducing the expression of these channels and increasing the expression of inhibitory ion channels/receptors.

We first showed that neurons treated with FMRP had enhanced expression of N-type Ca^{2+} channels as expected from the findings of Ferron et al.[202] and with age, there was a reduction in the expression of these channels (**Fig. 1a-b**) (Here, we will refer to neurons treated with FMRP as

neurons with elevated expression of N-type Ca^{2+} channels). **Fig. 1c** shows the experimental set-up for chronic stimulation. We cultured the neurons for 4 days before magnetically stimulating them for the next 4 days with increasing force daily (see rationale in **Appendix B Fig. 1**). The first 4 days gave the neurons sufficient time to establish their axonal and dendritic polarities. As neurite branching is highly regulated by N-type calcium channels, the first 4 days also allowed the expression of the ion channels to stabilize before activating them over the next 4 days.[205] After chronic stimulation, we either immuno-stained the neurons immediately or continued culturing them for 4 more days to observe whether the effects of neural networks were sustainable.

We found no significant difference in the expression of N-type Ca^{2+} channel among control neurons, control neurons treated with MNPs and magnetically stimulated control neurons although a decrease was observed in the latter (**Fig. 1d**). This could be because the N-type Ca^{2+} channels are essential for a range of neural functions and a minimum level of expression are needed for normal development.[205] Next, we found that stimulated neurons treated with FMRP had channel expression that were significantly lower (**Fig. 1f**) than FMRP treated neurons that were not chronically stimulated (**Fig. 1e**), demonstrating that chronic mechanical stimulation could affect the expression of mechano-sensitive ion channel.

Remarkably, we observed that chronic magnetic stimulation brought the expression of N-type Ca^{2+}channels in FRMP treated neurons down to a level similar to that of control neurons (**Fig. 1d**), supporting our hypothesis of magnetic force-mediated restoration of mechano-sensitive ion channel equilibrium. We also observed that the expression of N-type Ca^{2+} channels was similar in stimulated FMRP treated neurons at day 8 and 12 (**Fig. 1d**), showing that the effects of chronic magnetic stimulation were sustainable for at least 4 days. Next, we monitored the expression of TRPV4 which is the only type of mechano-sensitive ion channel other than N-type calcium

channel that has been reported for neural stimulation.[173] However, chronic stimulation did not affect the expression of TRPV4 (**Appendix B Fig. 2a-b**). We proposed a biophysical model to describe the mechanical sensitivity of different ion channels and how the application of different force magnitudes may specify the types of mechano-sensitive ion channels being stimulated (**Appendix B Fig. 2c**).

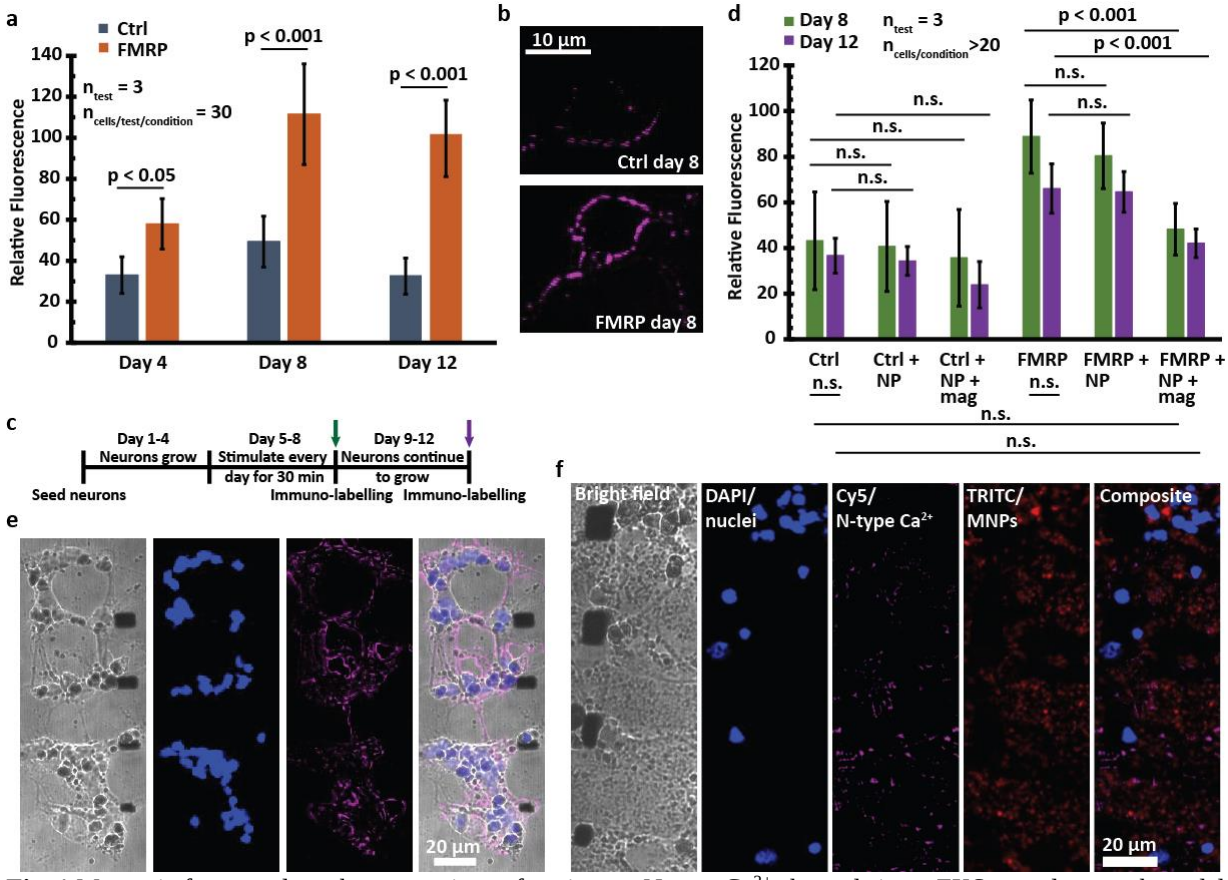

Fig. 1 Magnetic forces reduce the expressions of excitatory N-type Ca^{2+} channels in an FXS neural network model following chronic stimulations. (**a**) FXS model neurons express more N-type calcium ion channels and with age, there is a decrease in channel expression. (**b**) Confocal images show immuno-stained N-type calcium ion channels in the FXS model and control neurons. (**c**) Schematic shows the sequence of chronic stimulation. (**d**) FXS model neurons chronically stimulated with magnetic forces experience decrease in N-type calcium ion channel expression and the effects are sustainable for at least 4 days (day 8-12). Confocal images showing (**e**) FXS model neurons and (**f**) FXS model neurons after chronic stimulation. An evident decrease in N-type calcium ion channel florescent intensity is observed in the latter. Reproduced with permission from the American Chemical Society.

Patients with FXS typically have reduced expression of $GABA_A$ receptors,[201] resulting in network hyper-excitability as characterized by higher magnitude and frequency in calcium spikes (**Fig. 2**) in the presence of bicuculline. We wanted to investigate whether chronic magnetic stimulation could also modulate the expression of $GABA_A$ receptors. Although $GABA_A$ receptors are not mechano-sensitive, it has been shown that when excitatory (such as mechano-sensitive N-type Ca^{2+}) ion channels are chronically stimulated, the neural networks can compensate by increasing the expression of $GABA_A$ inhibitory ion receptors.[27] Interestingly, we found that FMRP treated neurons that underwent chronic magnetic stimulation did not have statistically significant different average (**Fig. 2a**) and peak $\Delta F/F_0$ (**Fig. 2b**) as compared to control neurons. The number of spikes per neuron at a given time was also reduced for chronically stimulated FMRP treated neurons compared to the non-stimulated FRMP treated neurons (**Fig. 2c**). These results show that magnetic force stimulation could have enhanced the expression of $GABA_A$ receptors, thus reducing the excitability (magnitude and frequency in calcium spikes) of FMRP treated neural networks in response to bicuculline (1.2 μM).

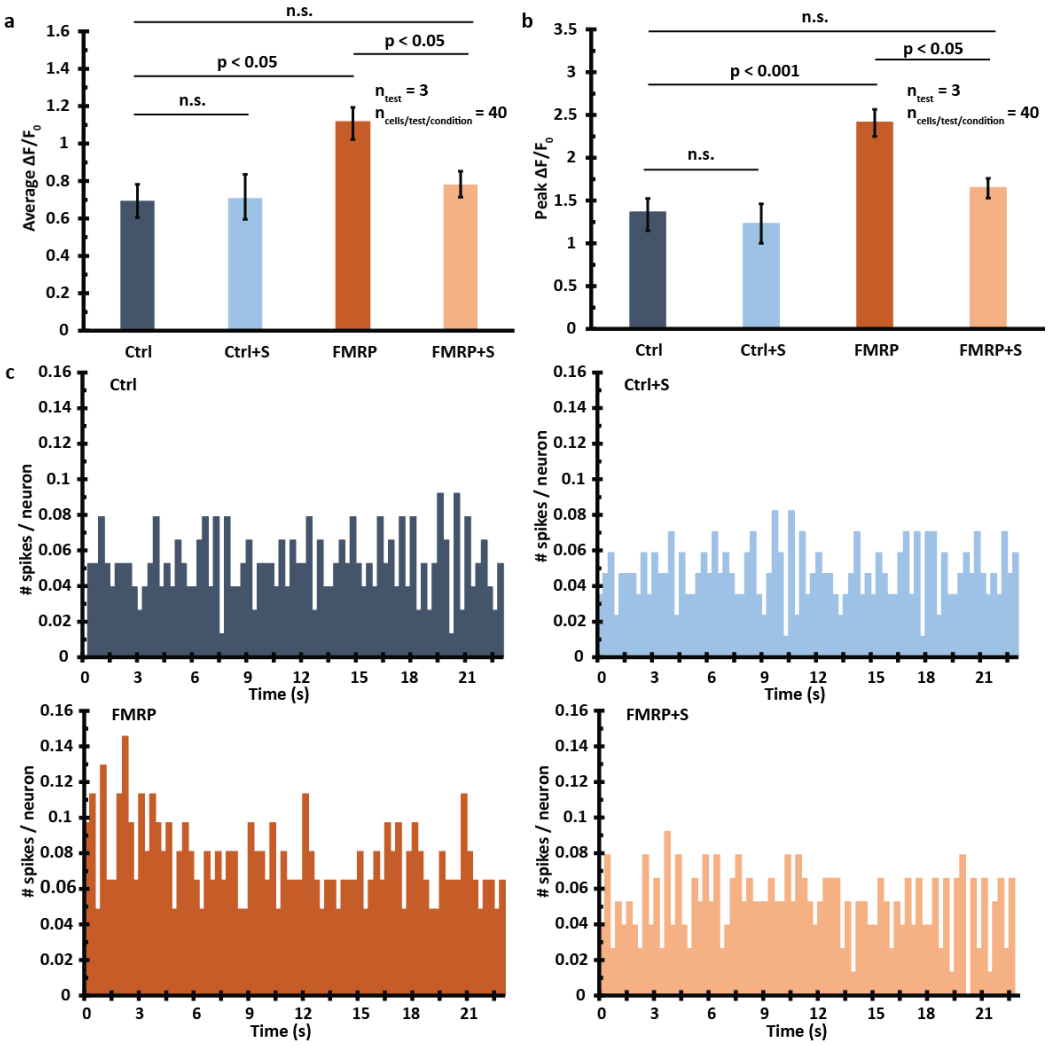

Fig. 2 Magnetic forces enhance the expression of inhibitory $GABA_A$ receptors in a day 12 FXS neural network model following chronic stimulation. Chronically stimulated FXS model neurons have lower (**a**) average and (**b**) peak $\Delta F/F_0$ and (**c**) calcium spiking frequencies than non-stimulated counterparts. This can be at least partially explained by enhanced expression of inhibitory $GABA_A$ receptors in the former which reduce excitability (magnitude and frequency of calcium spikes) of FMRP treated neural networks in response to bicuculline (1.2 μM). 'S' refers to chronically stimulated. Reproduced with permission from the American Chemical Society.

3.2 Conclusions

We showed that our technology can be employed to modulate N-type Ca^{2+} ion channel disequilibrium which is observed in FXS. It may be possible to combine our technology that has specific ion channel targeting - once significant challenges for *in vivo* use are addressed - with transcranial magnetic inhibition which is currently being employed to reduce cortical excitability

in patients.[206] The combined technology may also find utility as a non-invasive therapy in other neurological diseases by modulating the expression of endogenous mechano-sensitive ion channel density in cases like abnormal nociception where there is enhanced expression of N-type Ca^{2+} ion channels[207] and patients have to undergo highly invasive spinal injections with modified conotoxin.[208]

We also want to highlight that one advantage of our technique over other emerging techniques is that it does not require genetic manipulations, which still face the challenge of consistent transfection efficacy and heterogeneous expression, as N-type Ca^{2+} channels are relatively abundant on different classes of neurons as compared to TRPV ion channels. Nonetheless, as N-type Ca^{2+} channels are involved in many important neural activities (although N-type gene knockout mice develop healthily, with normal lifespan, behavior and motor functions[209]) and its expression reduces with age, more work is needed to enhance calcium influx with our technique for use in *in vitro* neural culture of different ages and *in vivo* brain study. Lastly, this technology can also be employed to investigate the effects of biomechanical forces on mechano-sensitive ion channel expression during neuronal development.[210]

3.3 Materials and Methods

Quantification of magnetic forces

The exact method is as described in.[54] A particle with a magnetic dipole within a magnetic flux density gradient, referred as magnetic gradient in the main text (∇B), experiences magnetic forces (eq. 1) due to its magnetic moment (m).

$$F = \nabla(m \cdot B) \qquad \text{eq. 1}$$

Superparamagnetic micro- and nanoparticles in high gradient magnetic fields exert forces based on the number i of aggregated particles with a particle volume (V_p). The resulting force (F) is due to a combination of parameters where $M_{p,sat}$ is the particle magnetization under magnetic saturation, $\nabla H(x, y, z)$ the gradient of the magnetic field strength and μ_0 the vacuum permeability (eq. 2).

$$F = \mu_0 \sum_{i=1}^{n} V_{p,i} M_{p,i,sat} \nabla H(x, y, z) \qquad \text{eq. 2}$$

The force magnitudes due to our magnetic elements (MEs) were characterized using fluorescently labeled 1 μm diameter superparamagnetic iron oxide beads. We extracted magnetic forces based on the steady-state motion of the bead moving in an aqueous medium (PBS, $\eta = 1 \cdot 10 - 3$ Pa s) within a magnetic gradient. Given the proximity to a surface, we used a Faxen's Law coefficient $\lambda_{Faxen} = 2.29$ in the viscous drag (eq. 3) to calculate force along trajectory positions.

$$F_{stoke} = -6\, \lambda_{Faxen}\, \pi \eta r_{h,}\, v_{=} \qquad \text{eq. 3}$$

Based on the exponential decay of the gradient field, and the linear relation between field and force, estimated forces were assumed to scale exponentially with distance from the MEs.

Chronic magnetic force stimulation

4-day-old cortical neurons were incubated with MNPs for 1 day or over 4 days for 6 hr daily and then magnetically stimulated. The neurons were either immuno-stained at day 8 or day 12. During

chronic magnetic force stimulation, the magnetic substrate was inverted in a petri dish and a 150 mT magnet was placed on top of the glass slide.

Statistical significance

Statistical significance was evaluated using Student's t-test after testing for normality using either one-way ANOVA, $p < 0.05$ (no rejection of normality), or nonparametric Kruskal-Wallis ANOVA, $p < 0.05$ (normality rejected) with, $n = 540$ cells in **Fig. 1a** (6 conditions, 3 tests, 30 cells/test), $n > 720$ cells in **Fig. 1d** (12 conditions, 3 tests, >20 cells/test) and $n = 480$ cells in **Fig. 2a-b** (4 conditions, 3 tests, 40 cells/test).

Chapter 4: Phenotypic selection of *Magnetospirillum magneticum* (AMB-1) using Magnetic Ratcheting

4.1 Introduction

In the previous chapters, I highlighted the utility of magnetic nanoparticle (MNP)-based neural stimulation techniques. However, it is important to acknowledge the limitations of these techniques such as heterogeneity in MNP properties and our poor understanding of protein corona formation on MNPs. This chapter aims to tackle some of these limitations by generating magnetotactic bacteria over-producers as a source of high quality MNPs.

Chemically synthesized magnetic nanoparticles (MNPs) have great utility in diverse biomedical applications including Magnetic Resonance Imaging (MRI), cancer hyperthermia therapy and neural stimulation as outlined in **Chapter 2-3**.[211] To be useful for these applications, ideally, MNPs should possess the following properties: (1) uniform sizes for consistent results, (2) high stability in aqueous solutions to reduce aggregation, (3) high thermal stability for controlled rise in temperature, (4) low cytotoxicity for interfacing with biological entities and (5) high flexibility for surface chemistry to enable drug and biological polymer conjugation.[212] Although advances in nanotechnology such as microfluidic-assisted nanoparticle synthesis have made some of these properties possible,[213] it usually comes with a compromise on the manufacturing costs and time that can be prohibitive for industrial production and research/medical use of MNPs.[214] Remnants of organic and inorganic solvents used to chemically synthesize MNPs does not yield a long-term green manufacturing solution and can also result in high cytotoxicity.[215] Lastly, large scale production of MNPs is still a challenge due to the stringent requirements for narrow size distribution and development of tailored protocols for surface functionalization either to reduce cytotoxicity or to increase specificity for biomedical use.[216]

Magnetotactic bacteria (MTB) were first scientifically described in 1975 by Blakemore[212] and since then, there has been an increasing number of publications on this class of bacteria that can reportedly sense the Earth's magnetic field for magnetoaerotaxis. Making use of a unique biomineralization process, MTB are able to assemble and precipitate linear chains of magnetite ($Fe(II)Fe(III)_2O_4$) NPs with different shapes (spherical, bullet, etc.) and sizes (35-120 nm) bound in lipid membranes known as magnetosomes specific to their strains[217] (Note: for easier comparison to chemically synthesized MNPs, we will now refer to magnetosomes as biologically synthesized MNPs). MNPs produced by MTB are superior to chemically synthesized MNPs as the former have homogeneous sizes and crystallography, possess high thermal stability, have low aggregation and can be easily functionalized using conventional surface chemistry techniques.[211]

However, MTB are fastidious prokaryotes that grow slowly even with optimized culture conditions[218] as compared to other micro-organisms commonly used in industry. As an example, the doubling time of MTB is ~4-6 hr[219] as compared to 20 min for *Escherichia coli.*[220] Kolinko et al. attempted to address the growth limitation by transferring 30 key genes from *Magnetospirillum (M.) gryphiswaldense* to *Rhodospirillum rubrum*, a faster growing prokaryote, and first demonstrated the possibility of endogenous magnetization in non-magnetic organisms using synthetic biology.[218] In addition, Lohβe et al. recently demonstrated the use of targeted gene editing to create MTB mutants that produce ~2 fold more MNPs, highlighting the usefulness of genetic variations to generate MTB over-producers that overproduce MNPs.[221]

The directed evolution of MTB is, however, limited by the lack of a selection platform. The current methods to select for MTB mutants are electron microscopy and color inspection of colonies or C_{mag}[222] which are slow, laborious, non-quantitative and subject to users' biases. A

selection platform that facilitates quantitative and high throughput selection of MTB mutants of interest can accelerate the process of directed evolution.

Conventional methods for magnetic separation involve pull down of objects with a magnetic dipole or induced dipole in response to a magnetic field gradient. There are a few technologies namely, batch magnetic separators, flow-through magnetic separators and magnetically stabilized fluidized bed separators to isolate particles based on their differences in magnetic content.[223] However, as MTB are motile by means of flagella,[224] their motion complicates the separation process. Several groups have also described the use of microfluidic devices to deflect particles across streamlines and into different outlets based on their different magnetic contents.[225,226] In these systems, we observed that bacteria motility is also a challenge. These techniques also face several other limitations as they (1) require precise fluid flow rates and magnetic field positioning to generate controlled magnetophoretic forces, (2) have low throughput due to their use of weak bulk magnetic field gradients and (3) offer a low output concentration in the form of diluted particle suspension.

Here, we describe the development of a magnetic ratcheting platform that facilitates automated, quantitative, and high throughput and resolution separation of AMB-1 of interest generated with random chemical mutagenesis. Using this technology, we generated AMB-1 over-producers producing 2-fold more MNPs than control AMB-1 with just 5 cycles of mutation and selection. The MNPs produced by the over-producers were also comparable in terms of size, shape and magnetic properties to those produced by the control AMB-1, making them equally valuable for diverse biomedical applications.

4.2 Results and Discussions

4.2.1 Random chemical mutagenesis generated AMB-1 overproducers

To diversify the genome of AMB-1, we performed random chemical mutagenesis using 10 μg/mL 5-bromo-uracil (5-BU) to interfere with the DNA replication cycle of the bacteria (See **Appendix C Fig. 1** for the rationale of using 10 μg/mL of 5-BU). Although random mutagenesis is less commonly used for directed evolution due to biases in the mutation spectrum (i.e. different rates in transitions and transversions genetic substitution),[227] it is arguably more suitable for our case as the genetic pathways regulating biomineralization are still largely unknown. A recent publication also highlighted the genetic complexity of MTB by reporting on accessory genes outside of the magnetosome islands that help to regulate biomineralization.[221] The approach of random chemical mutagenesis is also supported by the observation that frequent deletions and rearrangements in the magnetosome gene island (MAI) can be induced by metabolic stresses and ultraviolet irradiation.[228]

We showed that random mutagenesis generated AMB-1 with a wider range of MNPs/bacterium (**Appendix C Fig. 2A**) without affecting the size and the shape of the MNPs significantly (**Appendix C Fig. 2B-C**). This effect was not observed or noticeable from long-term culture of AMB-1 (up to 60 days) in normal media. As expected, this random chemical mutagenesis was also biased in generating mutants. Most of the AMB-1 had compromised biomineralization abilities while there was only ~3±2.2% more AMB-1 with ≥25 MNPs/bacterium. Although this method generated a small percentage of desired AMB-1, we performed magnetic ratcheting selection with ~10^6 of MTB/selection cycle, hence allowing us to harvest sufficient numbers of desired AMB-1 for downstream cultivation. **Appendix C Fig. 2D** compares the number of days of mutagenic treatment and its impact on mutant generation. Based

on the motivation for fewer days for a mutation-selection cycle and higher percentage of AMB-1 with >25 MNPs/bacterium generated by the treatment, we chose 8 days of 5-BU treatment.

4.2.2 Development of magnetic ratcheting platform

Our magnetic ratcheting platform consisted of arrays of permalloy (i.e. alloy of nickel and iron with exceptionally high magnetic permeabilization) micro-pillars with increasing horizontal pitches (spacings between micro-pillars) to enable rapid magnetophoretic equilibrium separation.[229] The platform is also comprised of a mechatronic device to continuously generate a cycling magnetic field that created strong moving magnetic potential wells to trap AMB-1 and to negate the effect of bacterial motility (**Fig. 1A**). The transport of AMB-1 across the ratcheting chip is governed by the balance between magnetic force *i.e.* MNP number (and size) and Stokes drag *i.e.* size of the bacterium (**Appendix C Equation 1-5**). As the size of all the AMB-1 was similar, AMB-1 can thus be separated in an equilibrium fashion based on their magnetic content.

AMB-1 ratcheted at a given frequency can traverse the arrays of horizontal permalloy pillars when it has enough velocity imparted by the magnetic force to traverse to the next pillar over a magnetic field cycle. When it reaches the critical pitch where the magnetic force does not provide sufficient force, the AMB-1 is trapped and will oscillate with the cycling field instead of ratcheting further to higher pitch regions. The critical ratcheting frequency for trapping AMB-1 for increasing pitch length is shown in **Appendix C Fig. 4.** This system is also applicable for another popular MTB strain i.e. Magnetospirillum gryphiswaldense (MSR-1) which is also spiral in shape.[212]

The steps for the mutation-selection cycle are shown in **Fig. 1B**. Each cycle took about 13-20 days with 8 days for chemical mutagenesis followed by 5-12 days of culture. We chose to

cultivate the AMB-1 in media with 5-BU for 8 days as we wanted the selection pressure to be based on both magnetosome number (through magnetic ratcheting selection) and growth rate as a slower growing AMB-1 would be out-competed. With each ratcheting cycle, we could isolate 50-350 desired AMB-1. Considering an 8-day mutation period and an average of 3.1 cell divisions/day (normally, cell division occurs every 4-6 hr but we gave a lower estimate as we grew AMB-1 in mutagenic media where 20% of the AMB-1 would perish, giving us an average $2^{4*(0.80\text{^}4)}$ cell divisions/day = 3.1 cell divisions/day), we could generate [2^{8*3} * 50 (number of starting AMB-1) * 0.0016 (estimated mutation efficiency with 5-BU although it could change with concentration of 5-BU and repair pathways of AMB-1)[230] * 0.95 (upper limit of reversion of mutant to wild-type state ~5%)[231]], the maximum number of unique AMB-1 we could generate was 1.27 million. Nonetheless, from literature on random chemical mutagenesis, we expect that most of the AMB-1 (99.99%) would be undesired due to their compromised activities like cell division/metabolism.

Our next step was then to cultivate the AMB-1 (10 µL suspension) for an additional 5-12 days to allow the desired AMB-1 (higher MNPs number and metabolism) to out-compete the non-desired ones. Note that the AMB-1 were not grown in a single tube (2 mL Eppendorf) for the entire duration but were transferred to a new tube for expansion every 3 days. The content in the tubes were then pooled together and processed through the ratcheting platform. This step was important to ensure that the AMB-1 did not experience growth stagnation due to media depletion or over-crowding. The cultivation period was lengthened progressively as we imposed increasingly stricter magnetic selection criterion (**Appendix C Table 3**) and isolated fewer numbers of desired AMB-1 over time. **Fig. 1C** shows the ratcheting chip with SYBR-green stained AMB-1 separated across the micro-pillar array with increasing horizontal pitches. AMB-1 at different regions were

collected for transmission electron microscopy (TEM) imaging to validate that AMB-1 over-producers could be isolated based on their magnetic content (**Fig. 1D**).

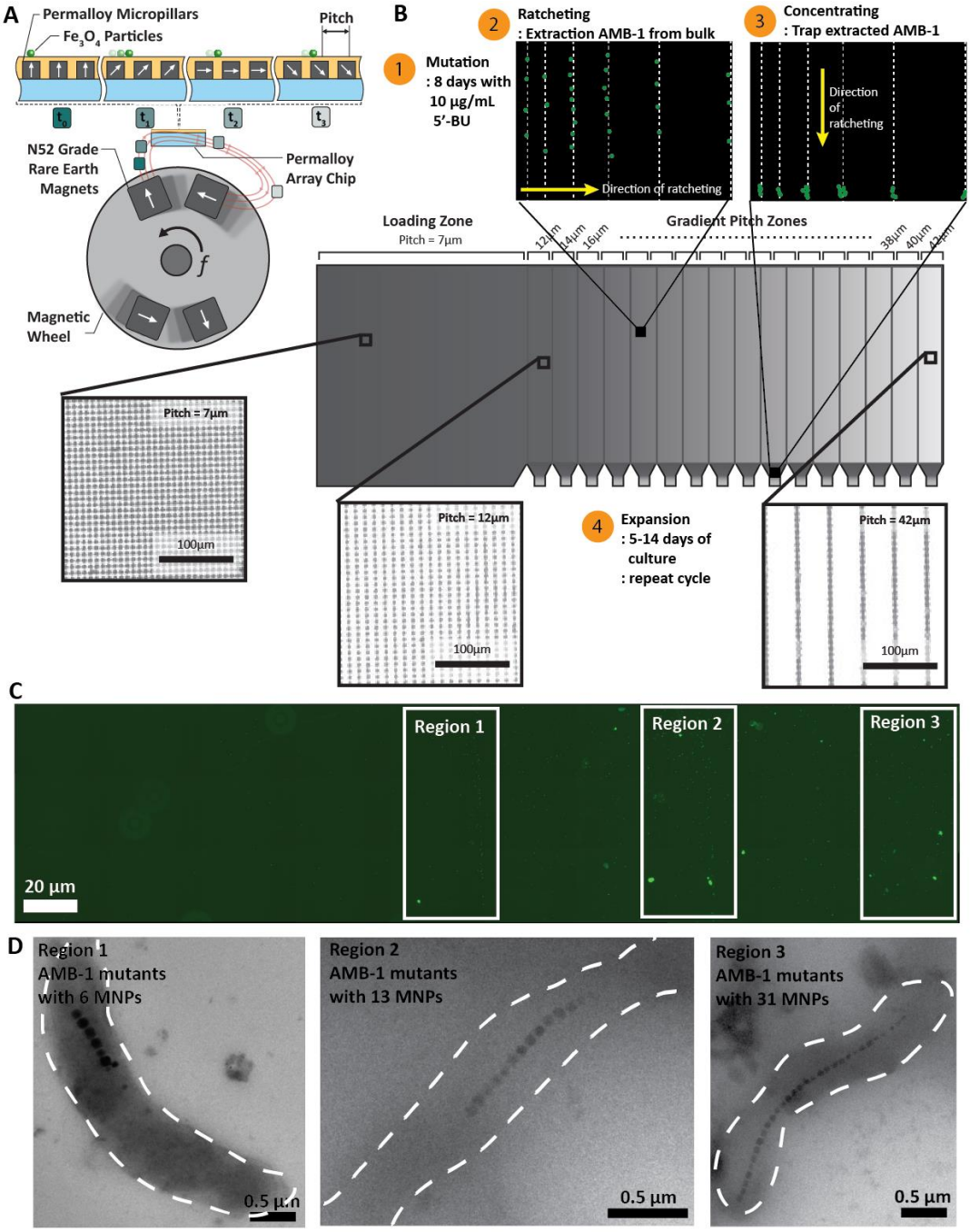

Fig. 1 Schematic and operation of selection process based on magnetic content. (**A**) Schematic of the ratcheting platform. (**B**) Process of the mutation-selection cycle and design of magnetic ratcheting chip with increasing widths in horizontal pitches. (**C**) Magnetically separated AMB-1 stained with SYBR-green in different regions on the ratcheting chip. Cells with higher magnetic content can ratchet further to the right to regions of higher pitch between

permalloy elements. (**D**) AMB-1 are separated based on their magnetic content. AMB-1 in region 1 had the lowest number of MNPs/bacterium while those in region 3 had the highest number of MNPs/bacterium.

4.2.3 Selection of AMB-1 overproducers with magnetic ratcheting

AMB-1 generated after one mutation-selection cycle from region 3 (**Fig. 1D**) were collected, cultured and imaged. The average number of MNPs/ bacterium in the selected population was 17.0 $\pm$ 4.0 while that of the control population was 11.2 $\pm$ 3.7 (**Fig. 2A**). The C_{mag} value of the selected population was also higher (**Fig. 2B**), showing that this population was more magnetic. The size (**Fig. 2C**) and shape (**Fig. 2D**) of the MNPs for both populations were similar. Our magnetic ratcheting platform hence isolated AMB-1 based on their number of MNPs as both size and shape which are known to affect the magnetic properties of MNPs were not significantly different in this case. Through this observation, we also speculate that the genes regulating MNP number may also be more susceptible to chemical mutagenesis than those controlling MNP shape and size. This may be because there are more genes such as in the *mamAB* operon[232] and other accessory genes regulating nitrate metabolism that influence the number of MNPs/bacterium while so far, only the *mamGFDC* operon has been implicated, albeit in a small role, in regulating the size/shape of MNPs.[233]

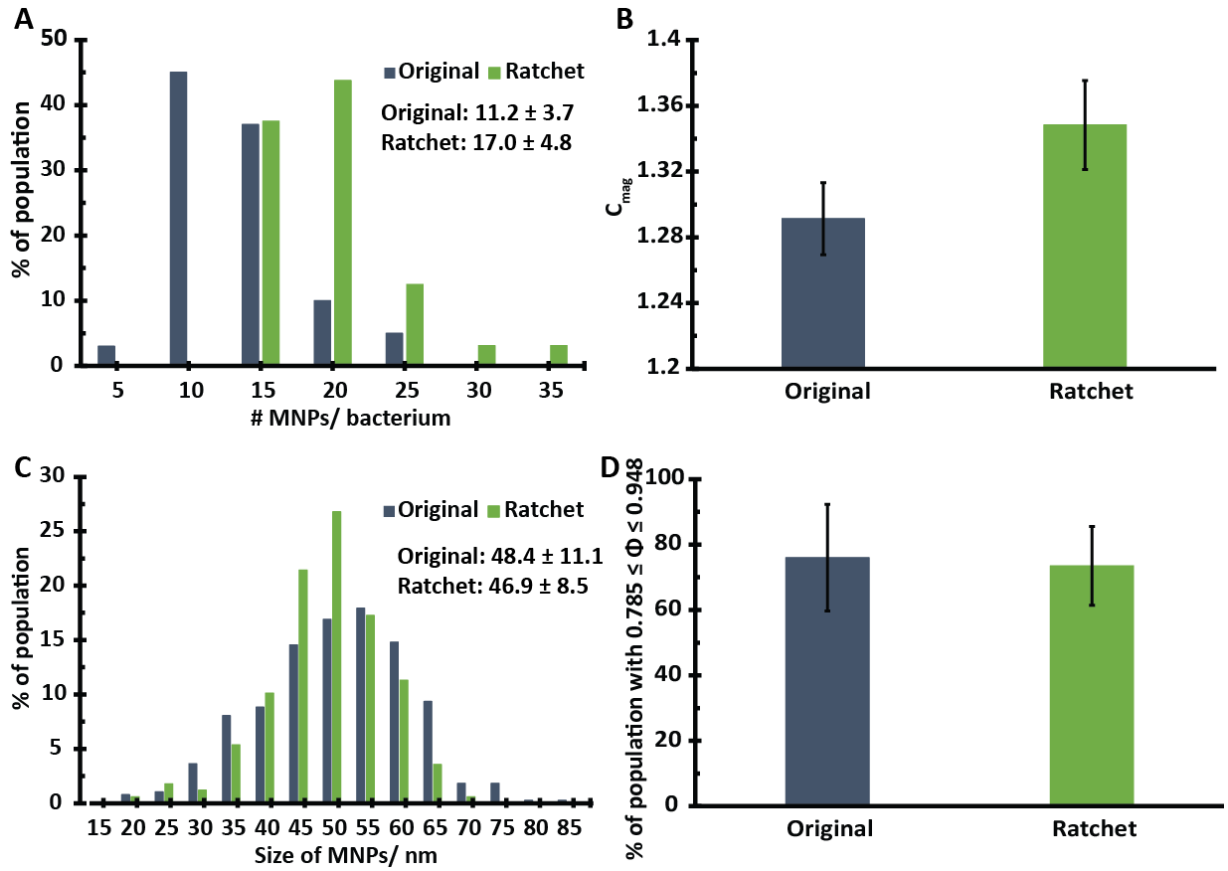

Fig. 2 Magnetic ratcheting platform facilitated selection of sub-populations of AMB-1 with greater magnetic content. (**A**) Population histogram showed that AMB-1 selected through a single cycle of ratcheting following mutagenesis contained an average 6 more MNPs/ bacterium. (**B**) The C_{mag} value showed an increase in bulk magnetic properties of selected AMB-1. (**C**) Ratcheting selection did not significantly affect the average size of the MNPs and it decreased the deviation in size distribution. (**D**) Average circularity of the MNPs was unaffected by the ratcheting experiment.

4.2.4 Generation of AMB-1 library with magnetic ratcheting

The magnetic ratcheting platform also allowed us to collect AMB-1 of interest from region 1 (**Fig. 1D**) with no MNPs (**Fig. 3A**). As there is significant interest in studying genes regulating the biomineralization pathways, the AMB-1 producing no MNPs can be used to screen for such genes using our platform. Compared to targeted genetic manipulation, AMB-1 produced by random chemical mutagenesis have larger genetic diversity, allowing higher throughput in identifying genes in the magnetosome islands or accessory genes responsible for MNP production with our platform.

With 5 cycles of mutation-selection, we generated a library of AMB-1 producing an average of 25 MNPs/ bacterium which we validated with electron imaging and C_{mag} measurements (**Fig. 3B**). The AMB-1 over-producers continued to produce more than 2-fold more MNPs than wild-type AMB-1 after 2 months of culture, showing stable phenotypes (**Appendix C Fig. 6B**). This observation also demonstrates that chemical mutagenesis allowed us to generate stable AMB-1 and our method was truly selecting for desired AMB-1 and not non-mutated AMB-1 with naturally higher number of MNPs/bacterium. Nonetheless, we note that due to the randomness and low efficacy of chemical mutagenesis in generating over-producers, there was an efficacy reduction to increase the number of MNPs/bacterium overtime. However, we expect that this problem could be overcome by combining targeted genetic manipulations, magnetic ratcheting selection and lower cost next-generation sequencing after more is understood about the MTB genome.

4.2.5 The properties of magnetosomes produced by overproducers were similar to wild-type

While it is important to generate AMB-1 that overproduce MNPs, it is highly crucial that the properties of the MNPs are maintained. This can be a concern in our work as we employed random chemical mutagenesis which might have disrupted genes regulating the aqueous stability, size, shape and magnetic properties of the MNPs.

We first investigated the aqueous stability of the magnetosomes and found that those produced by AMB-1 over-producers did not aggregate (**Fig. 3C-D**). This is an important property as iron oxide MNPs possess high surface energy and are prone to aggregation which can reduce the efficacy of their use.[234] Next, we found that over the multiple cycles of mutation-selection, the size of the MNPs increased slightly which was also observed by Lohβe et al.[221] (**Fig. 3E**). The

shape of the MNPs were, however, similar across the AMB-1 isolated in the cycles. It is advantageous to maintain the cubo-octahedral shape of the MNPs as it is known that the shape of MNPs can affect their magnetic/thermal/catalytic properties[235] and also interactions with biological processes such as endocytosis[236] and cytotoxicity.[237]

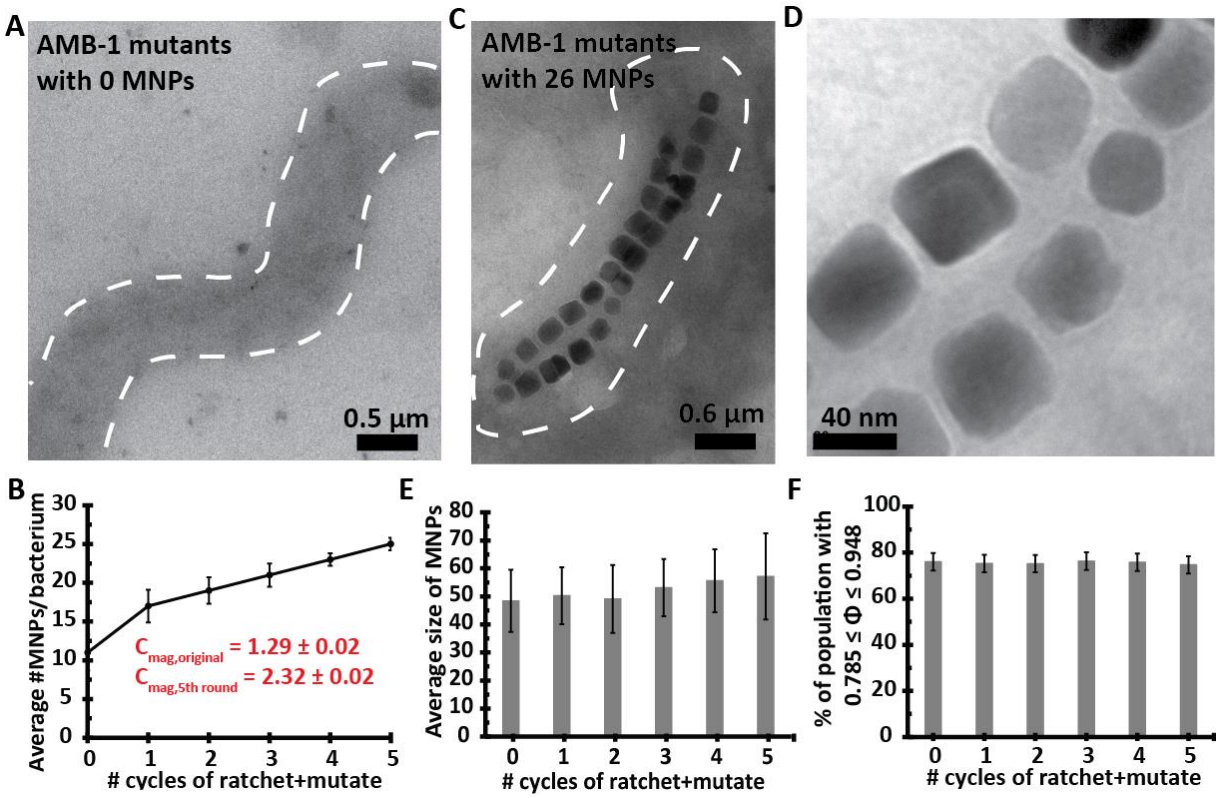

Fig. 3 Library of AMB-1. With the ratcheting platform, we isolated (**A**) AMB-1 without any MNPs and also (**B-C**) over-producers that produced 2 fold more MNPs compared to the original population. n = 30 per TEM/selection cycle. (**D**) High aqueous stability of the MNPs produced by over-producers. The (**E**) size and (**F**) shape of the MNPs produced by over-producers were also similar to the control AMB-1 population.

We next investigated the elemental composition of the MNPs as MNPs composed fully of magnetite are more useful for biomedical applications such as cancer hyperthermia. To understand whether the process of directed evolution affected the compositional purity of the MNPs produced by our AMB-1 over-producers, we performed high resolution TEM and compared their corresponding crystal lattice to wild-type AMB-1. **Fig. 4A** shows that for all lattice fringes that

could be resolved, the MNPs produced by AMB-1 over-producers were determined to be magnetite. Lastly, we determined the functional properties of the MNPs through SQUID measurement and found no significant difference between the AMB-1 wild-type and over-producers, supporting that MNPs produced by the latter maintained their ferromagnetic properties (**Fig. 4B**).

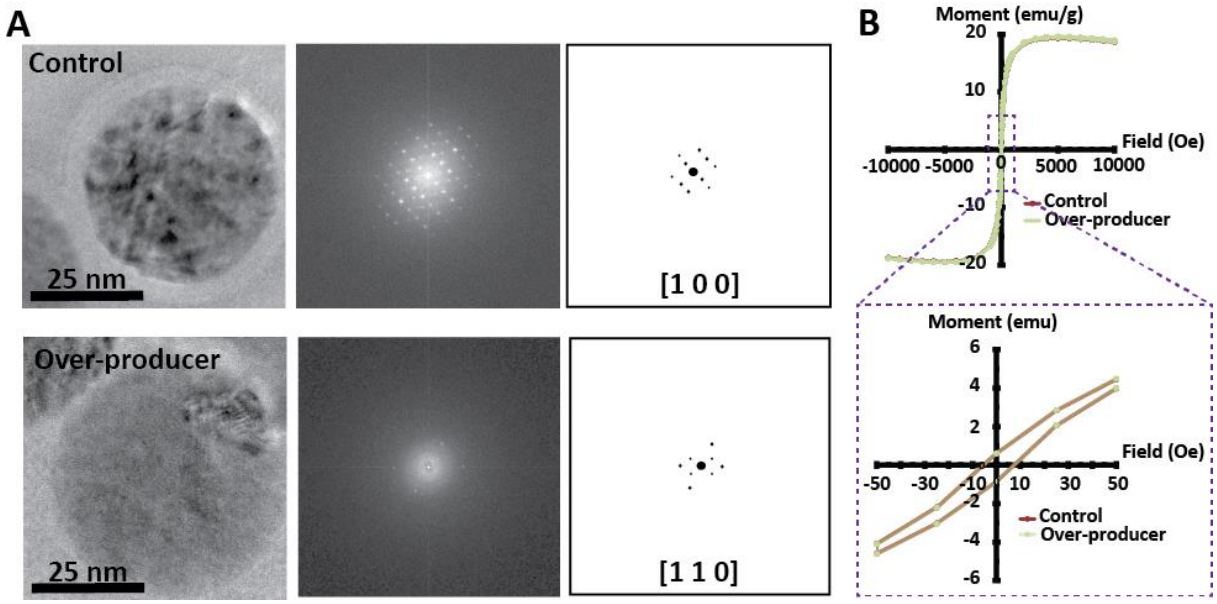

Fig. 4 Magnetic properties of the MNPs produced by AMB-1 over-producers were similar to that of control AMB-1. (**A**) High resolution TEM showed that for all resolvable fringes, the MNPs produced by both AMB-1 control and over-producers were determined to be composed of magnetite. (**B**) SQUID analysis showed that the long moment of the MNPs produced by AMB-1 over-producers were highly similar to that of AMB-1 control. Bottom: The line transparency of the mutant MNPs is reduced to reflect the overlap with that of the control.

4.3 Conclusions

Here, we described the combination of random chemical mutagenesis and phenotypic selection using a magnetic ratcheting platform for enrichment of AMB-1 over-producers. Through this system, we generated AMB-1 with 2-fold more MNPs/bacterium than the original population. This number is similar to the highest reported increase in number of MNPs/bacterium[221] but the time taken to generate the over-producers was significantly less.

Moving forward, we plan to perform whole genome sequencing of our over-producers after single colony isolation to potentially discover novel functions of genes regulating biomineralization. Nonetheless, we must acknowledge that this is not a trivial task. Takeyama group attempted to sequence the whole genome of AMB-1 but there are regions with missing sequences and more than 2290 open reading frames are unknown and useless for functional predictions.[238] The problem is also compounded that the AMB-1 sequence has not been independently verified for compliance with the finishing standard for error rates. Hence, while gene dissection is a great complement to this paper for generating MTB over-producers, practically, this endeavor requires significantly more time and resources beyond our current means in the absence of collaborations.

It is also important to highlight that the scope of this result is to present a magnetic platform to enrich MTB over-producers that produce functional MNPs for biomedical applications. While gene sequencing is important for subsequent targeted genetic manipulations to generate MTB over-producers, here, we would like to emphasize, arguably, the greater utility of phenotypic selection, especially for our goal of enriching MTB over-producers for their high quality MNPs. Firstly, over-expression of key genes responsible for biomineralization does not necessary generate mutants producing MNPs with the same useful properties as MNPs from wild-type MTB. For instance, the *Rhodospirillum rubrum* mutant generated by Kolinko et al. did not produce MNPs with uniform size and magnetic properties as MTB.[218] In addition, Taoka et al. increased the number of MNPs/bacterium in AMB-1 that over-expressed *mamP* but the shape/size of MNP became highly heterogenous.[239] To the best of our knowledge, all existing studies that tried to generate MTB over-producers with targeted genetic manipulations did not show comprehensive evidence that the magnetic properties of MNPs produced by over-producer mutants were similar

to wild-type.[240] This is especially true as HRTEM was not performed to determine whether the MNPs from mutant over-producers are still composed of 100% magnetite useful for biomedical applications or iron sulphide that has been reported elsewhere and are not as useful as they do not respond to both static and alternating magnetic fields. On the other hand, our AMB-1 over-producers generated MNPs with size distribution and shape of the MNPs similar to wild-type, supporting the utility of MNPs for intended biomedical applications where size/shape factors can affect processes such as cytotoxicity and endocytosis. Through high resolution electron microscopy and SQUID, we also determined that the MNPs produced by the AMB-1 over-producers had high compositional purity of magnetite and similar magnetic properties to the wild type. It is important to highlight that as the ratcheting platform selects for over-producers not only based on their magnetic contents but also that the MNPs were ferromagnetic (and hence composed of 100% magnetite) for the bacteria to experience substantial magnetic forces. As the goal of our project is to generate functional MNPs, we argue that the properties of the MNPs from our over-producers are a more useful indicator than the discovery of novel genes to assess the utility of our magnetic ratcheting platform.

Secondly, targeted modifications of the genome may not necessarily be associated with the phenotypes of interest. With increasing evidence from single cell analysis, it is becoming clear that cells can harbor huge variations in genome which are not expressed in phenotypes or have the same genome but different phenotypes due to reason such as stochastic expression of genes.[241] One particularly good example is the mutant produced by Lohβe et al.[221] where there is double copy of genes in the MAI. While the mutant over-produced 2-fold more MNPs/bacterium, through discussion with the Schüler's group, we learnt that the mutant is extremely prone to losing its over-producer phenotype due to the extra set of genes needed for replication during cell division. This

is not a new problem in molecular biology where it is frequently observed that cells face selection disadvantage to uptake and integrate large plasmids into their genomes. Most notably, as there are frequent deletions and rearrangements in the MAI,[228] the stability of MTB mutants produced by targeted genetic manipulations is also lower than most other bacteria. On the other hand, our AMB-1 over-producers maintained their stable phenotypes for up to 60 days which was not reported by other existing papers, showing that magnetic ratcheting generated sufficient selection pressure for over production of MNPs.[221]

One limitation in this paper is the use of random chemical mutagenesis which did not provide a high yield of over-producers consistently. As we learn more about the AMB-1 genome, it may become feasible to combine targeted genetic manipulations with our magnetic ratcheting platform to generate AMB-1 over-producer strains better than what we have reported here and elsewhere. We envision the utility of our magnetic ratcheting system and targeted genetic manipulation to generate MTB over-producers with known genetic make-up and stable phenotypes.

MNPs produced by MTB have numerous advantages over their chemically synthesized counterparts. However, there is currently no suitable selection technology to boost the production of biologically synthesized MNPs by MTB. We believe that the magnetic ratcheting system described here provides an automated, quantitative and high throughput avenue to facilitate biotechnological breakthroughs using MTB including single cell analysis, magnetic content quantification and enrichment of over-producers.

4.4 Materials and Methods

Culture Conditions

AMB-1 (ATCC700264) was grown in magnetic Sprillum growth media (MSGM) supplemented with ferric malate (30 μM) as previously described.[217] For clone selection, AMB-1 was plated onto 0.7% agar. Cultures for C_{mag} measurements or TEM were grown in 10 mL MG medium containing 25 mM HEPES buffer (pH 7.2) and ferric malate under a 10% oxygen atmosphere at 30°C in sealed tubes. Mutagenic media also contained 10 μg/mL 5-bromouracil. Relative growth rate was determined as a ratio of OD_{600} measured with an Agilent 8000 UV-Visible spectrophotometer.

Characterization of cellular magnetization (C_{mag})

The Cmag was determined as previously described.[242] Briefly, OD400 nm was measured on an Agilent 8000 UV-Visible spectrophotometer with a magnet parallel or perpendicular to the spectrometer beam and the ratio ($Cmag = A_{400\ nm,\ perpendicular}/A_{400\ nm,\ parallel}$) was calculated. The Cmag measurements were performed in biological triplicates from three independent growths.

Isolation of magnetosomes

AMB-1 were re-suspended in 10 mM Tris-HCl buffer and sonicated for 40 mins with an alternating sonicator pulse (1 s 'ON', 1s 'OFF') at 15 W to extract the magnetosome chains. After sonication, the solution containing the extracted magnetosome chains was placed against a 450 mT magnet and the supernatant was removed. The supernatant was removed after 30 min of magnetic treatment and this was repeated 3 times before re-suspending the magnetosomes in 20 μL Tris-HCl for high resolution TEM.

SQUID Characterization

Magnetic properties of the MNPs were measured using SQUID (superconducting quantum interference device). Briefly, the hysteresis curve was obtained from measuring the magnetic moment as the field is changed from 10000 Oe to -10000 Oe and then back to 10000 Oe at 298 K.

Chip Fabrication

Polished borosilicate glass (Fisher) slides were cleaned with piranha solution (30 min), washed in DI water and dried before deposition of 50-nm-Ti, 200-nm-Cu and 50-nm-Ti seed layer using a CHA Mark 30 E Beam Evaporator. SPR 220 photoresist was spun and processed according to specification to form electroplating molds for nickel-iron alloy. Ti was etched in 1% HF, and NixFey was electroplated in a custom plating setup to a ~ 4μm thickness. Photoresist was stripped and both the Ti and Cu layers were etched completely. The chip was sealed by deposition of 100 nm SiN (PECVD). Spin on polystyrene was spun to a thickness of ~1μm above the pillars. Before use, substrates were immersed in 2% by volume Pluronic F127 for 45 minutes.

Automated Ratcheting System and Particle Experiments

The automated ratcheting system consists of a radial array of N52 grade rare earth neodymium ferrite magnets (KJ Magnetics), with a quasi halbach array arrangement (strength ranged from 20-200mT), driven by a custom designed mechatronic system and Labview® interface. Streptavidin coated 1 μm iron oxide particles with 17% iron oxide content (Invitrogen), were functionalized with biotinylated FITC fluorescent probes (Invitrogen) to collect data for model in **Sup Fig. 3**. Particles were diluted to working concentrations between 0.5~1 x 10^6 particles/mL. PDMS interface chips (Dow-Corning) were fabricated using scotch tape lithography and clamped to the ratcheting chips using a custom made polycarbonate clamp. Separation experiments were executed

by inverting the chip on the stage of a Nikon Eclipse Ti fluorescent microscope and positioning the ratcheting system above it.

Electron microscopy

An aliquot of cell culture (100–500 µL) was pelleted by brief centrifugation (14,000 × g) for 10 min aerobically at room temperature and resuspended in MSGM (~10 µL). The cells were adsorbed onto 400-mesh copper grid coated with Formvar/Carbon (TedPella Inc.). TEM was performed using 120 kV T12 Quick CryoEM with a point resolution of 0.34 nm. High resolution TEM was performed using Titan S/TEM at 200 kV with 0.19 nm resolution. Imaging and data processing was performed at the UCLA CNSI Electron Imaging Center for NanoMachines (EICN). Electron diffraction simulation was performed using crystal maker software.

Chapter 5: Magnetic Microfluidic Separation for Estimating the Magnetic Contents of Magnetotactic Bacteria

5.1 Introduction

In **Chapter 4**, I described the use of magnetic ratcheting system. Nonetheless, the platform does not allow continuous enrichment of MTB over-producers in a long-term sterile condition. In this chapter, I detail the development of a magnetic microfluidic system that can overcome the limitations of magnetic ratcheting system using Δ*fla* MTB. I also present a proof of concept design that a parallelized version of the magnetic microfluidic system can be coupled to a bioreactor for high volume sorting of MTB based on their magnetic content.

Current tools for selecting MTB based on the quantity of magnetic material per cell are limited. The available tools used for MTB selection are electron microscopy, C-mag and color inspection of the bacterial colonies.[222] These methods are slow, subjective, non-automated and non-quantitative. Tay et al. overcame some of these limitations by describing a magnetic ratcheting system for directed evolution of MTB as described in **Chapter 4**. However, the setup is non-sterile and cannot be integrated with a bioreactor for continuous selection/enrichment of MTB of interest (**Appendix D Table 1**).

Microfluidic flow has been exploited for cell separation based on cellular properties like size, deformability, surface antigen expressions and also magnetic contents.[243] The micro dimensions of microfluidic channels allow steep magnetic fields to be established locally to generate significant magnetic forces to deflect the motion of MTB mutants by their number of ferromagnetic magnetosomes as they flow through the micro-channels.

Here, we describe a magnetic microfluidic device for fast selection and estimation of magnetic content of MTB i.e. *Magnetospirillum magneticum* (AMB-1). To overcome bacterial

flagella motion, we transiently treated AMB-1 with cold temperature (10 ^{o}C) at pH 8.5 which did not affect their long-term cell division and magnetosome production rate. Next, using previously generated AMB-1 mutants with average number of magnetosomes/bacterium of 3.0 $\pm$ 0.5, 11.2 $\pm$ 3.7 and 25.0 $\pm$ 3.5, we demonstrate the potential of the magnetic microfluidic chip to perform estimation of magnetic content in the AMB-1 mutants. In addition, we applied this device for processing another popular MTB strain, *Magnetospirillum gryphiswaldense* (MSR-1) for cell cycle synchronization. We believe microfluidic technology can greatly facilitate biological applications with MTB from selection to analysis.

5.2 Results and Discussions

5.2.1 Design of magnetic microfluidic device

The magnetic microfluidic device consists of 2 inlets, top for media and the bottom for MTB suspension, and 2 outlets i.e. selection (top) and waste (bottom) (**Fig. 1a**). A neodymium magnet is placed adjacent to the micro-channel to generate a local magnetic field. An incision approximately the dimension of the magnet is made ~0.9 cm away from the microchannel to hold the magnet firmly in place. AMB-1 flow through the bottom inlet and experienced different magnitudes of magnetic forces based on their magnetic contents which determine whether they exit through the selection or waste outlet. The cross-stream migration of AMB-1 is determined by the balance between Stokes' drag and magnetic forces (**Appendix C Equation 1 and 4**). AMB-1 having more magnetosomes experience greater magnetic forces which increases their terminal velocity (y-axis) for crossing the stream (**Fig. 1b**).

5.2.1 Optimizing flow ratio with particles

To understand the initial streamlines occupied by AMB-1 under flow in micro-channels, we first characterized the motion of 3 μm non-magnetic beads which is about the average size of AMB-1 (**Fig. 1b**). This process is also useful for us to pinch the bottom stream as the positions of the AMB-1 along the z-axis parabolic velocity profiles also affect their transit time for crossing the stream. As expected based on conservation of mass, with a higher flow ratio between the buffer and particle inlets, particles focused closer to the bottom channel wall.

We observed behavior at a flow ratio of 0.5 to 10 (media inlet/MTB inlet) with the flow rate of the MTB inlet set at 10 μL/min. **Fig. 1c** shows tighter focusing of the beads to the bottom channel wall as the flow ratio increased. Tight focusing is useful for us to minimize low magnetic content AMB-1 being collected at the selection outlet. Since we create flow with syringe pumps, we also found that when the combined inlet flow rates were below 10 μL/min, the flow was highly unstable and slight disturbances to the device disrupted the focusing behaviors of the beads.

Next, we characterized the deflection of 1 μm magnetic beads under different magnetic field strengths 0-450 mT at a flow rate of 10 μL/min (MTB inlet). As the distance between the magnet and microchannel is kept constant, a stronger magnet provided a steeper field gradient to generate stronger upward forces (**Appendix C Equation 1**). The average number of magnetosomes/AMB-1 bacterium is 11-20 and based on the magnetic properties of the magnetosomes, a chain of 20 magnetosomes is expected to experience a similar magnetic force as a 1 μm magnetic bead due to their similar magnetic volumes (**Appendix D Table 2**). We found that a neodymium magnet providing a magnetic field of 373 mT (**Appendix D Fig. 1**) and 450 mT is sufficient to deflect ~70% and ~80% of 1 μm magnetic beads into the selection outlet

respectively (**Fig. 1d**). This characterization allows us to establish the threshold magnetic field/force to isolate AMB-1 mutants of interest i.e. those with ≥ 20 magnetosomes/bacterium.

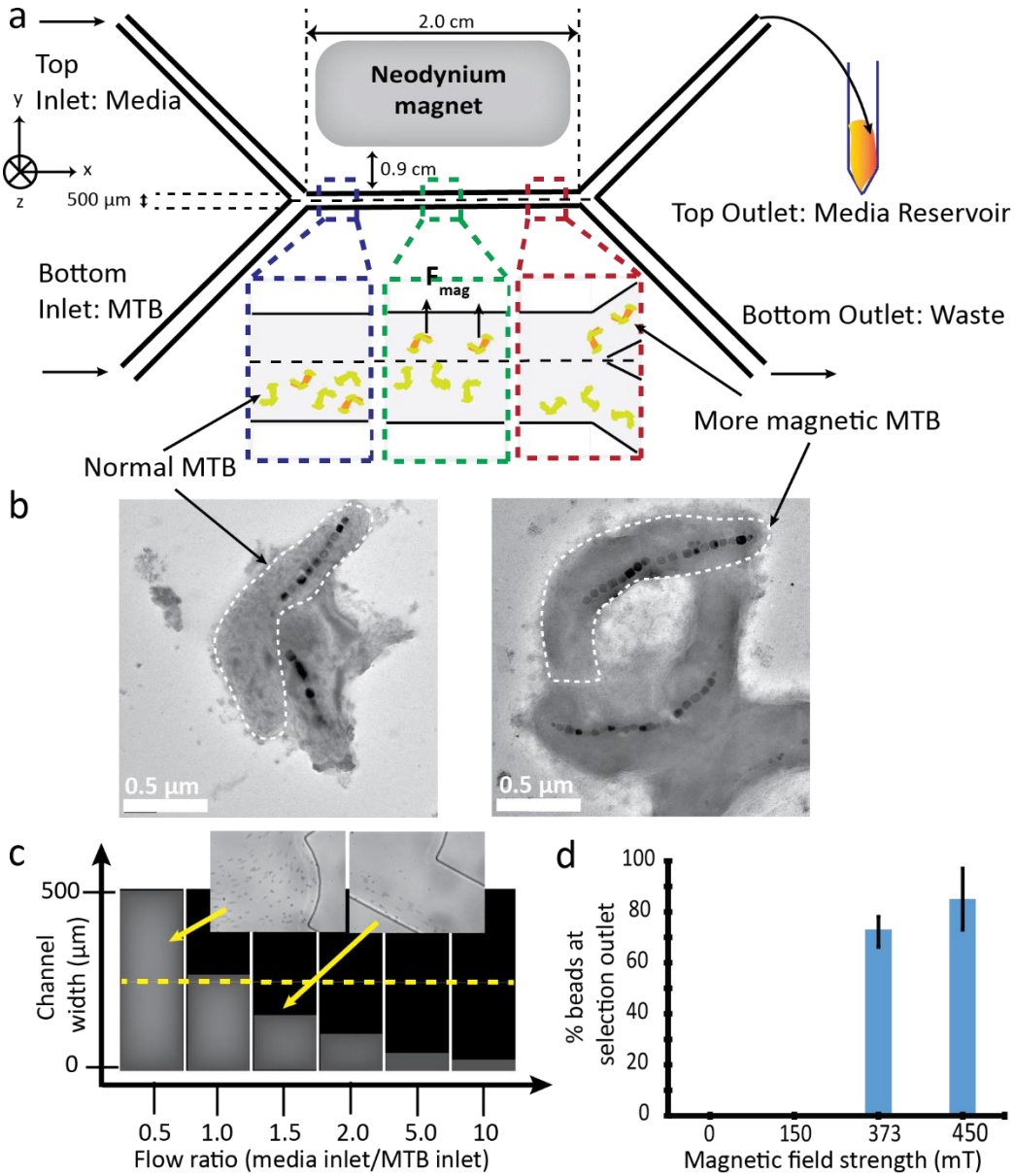

Fig. 1 Optimizing parameters for micro-channel flow. (**a**) Design of microfluidic device for magnetic deflection. (**b**) AMB-1 with different number of magnetosomes. The average length of AMB-1 is about 3 µm. (**c**) Focusing behaviors of 3 µm beads at different flow ratios. A minimum flow ratio (buffer inlet/ MTB inlet) of 1.5 is needed to completely focus all the non-magnetic beads into the waste outlet. The white-colored areas represent the widths filled by the 3 µm beads. Inserts: focusing widths of the 3 µm beads. (**d**) Deflection of 1 µm magnetic beads at different magnetic field strengths. A magnetic field strength of 300 mT is sufficient to deflect ~70% of 1 µm magnetic beads.

5.2.3 Minimizing flagella motion

We observed that at the optimized flow rate of 10 μL/min for the MTB suspension, the bacterial flagella motion could overcome magnetic forces, thus reducing the isolation efficiency and purity. We hence evaluated flagella motion under different conditions and sought to modify the operation environment to minimize flagellar movements. We tracked the motion of the AMB-1 at 4 ^{o}C, 10 ^{o}C, 25 ^{o}C, 37 ^{o}C and 50 ^{o}C, and found that as the temperature increased, the normalized root mean square (RMS) speed increased, possibly due to greater bacterial metabolic rates (**Fig. 2a**). We also tracked the flagella motion from pH 7.5 (their typical growth media condition) to pH 10 with 0.5 step increment. Consistent with the knowledge that the flagellar motion is powered by the proton pump,[244] we observed that as the pH becomes less acidic i.e. less available protons, the normalized RMS speed of the AMB-1 decreased (**Fig. 2b-c**). Interestingly, at pH 9.5 and 10, the trend reversed which we hypothesize might be due to activation of stress responses in AMB-1. Another way to remove flagellar motion is to knock out the fla gene encoding for flagella which was shown not to affect the growth and magnetosome production rates in MTB.[245]

Next, we assessed the growth and magnetosome production rate of AMB-1 that have been transiently treated with 10 ^{o}C media at pH 8.5 for 45 min. The treatment time was determined based on the maximum time the AMB-1 had to be under these environmental conditions during microfluidic flow (**Appendix D Table 3**). We found no significant difference in the optical densities after 3 days of culture in normal culture media and number of magnetosome per cell (**Fig. 2d**) in AMB-1 that were subject to the cold/alkaline treatment.

Lastly, we measured the magnetic properties of AMB-1 transiently treated with 10 ^{o}C media at pH 8.5 for 45 min and found that consistent with literature,[246] the treated AMB-1 still displayed ferromagnetic properties (**Fig. 2f**). This property allowed us to magnetize AMB-1 and

deflect the mutants of interests as they flow through the micro-channel even after cold/alkaline treatment. We also noted that the magnetic saturation of the AMB-1 was around 60 Oe (*i.e.* 6 mT) and that our choice of magnetic field strength of 373 mT is sufficient to induce saturation to generate maximum magnetic forces to deflect the AMB-1.

Based on the previous characterization conditions, all our later experiments were performed with AMB-1 suspended in 10 ^{o}C, pH 8.5 media flowing in micro-channels in the presence of a 373 mT magnetic field. However, MTB does not grow optimally under the cold/alkaline environment so instead, we propose to use this magnetic microfluidic device for quantitative estimation of the magnetic contents in MTB. However, in **Section 5.2.6**, I will show a proof-of-concept how we can still use the platform for large scale MTB cultivation using Δ*fla* MTB.

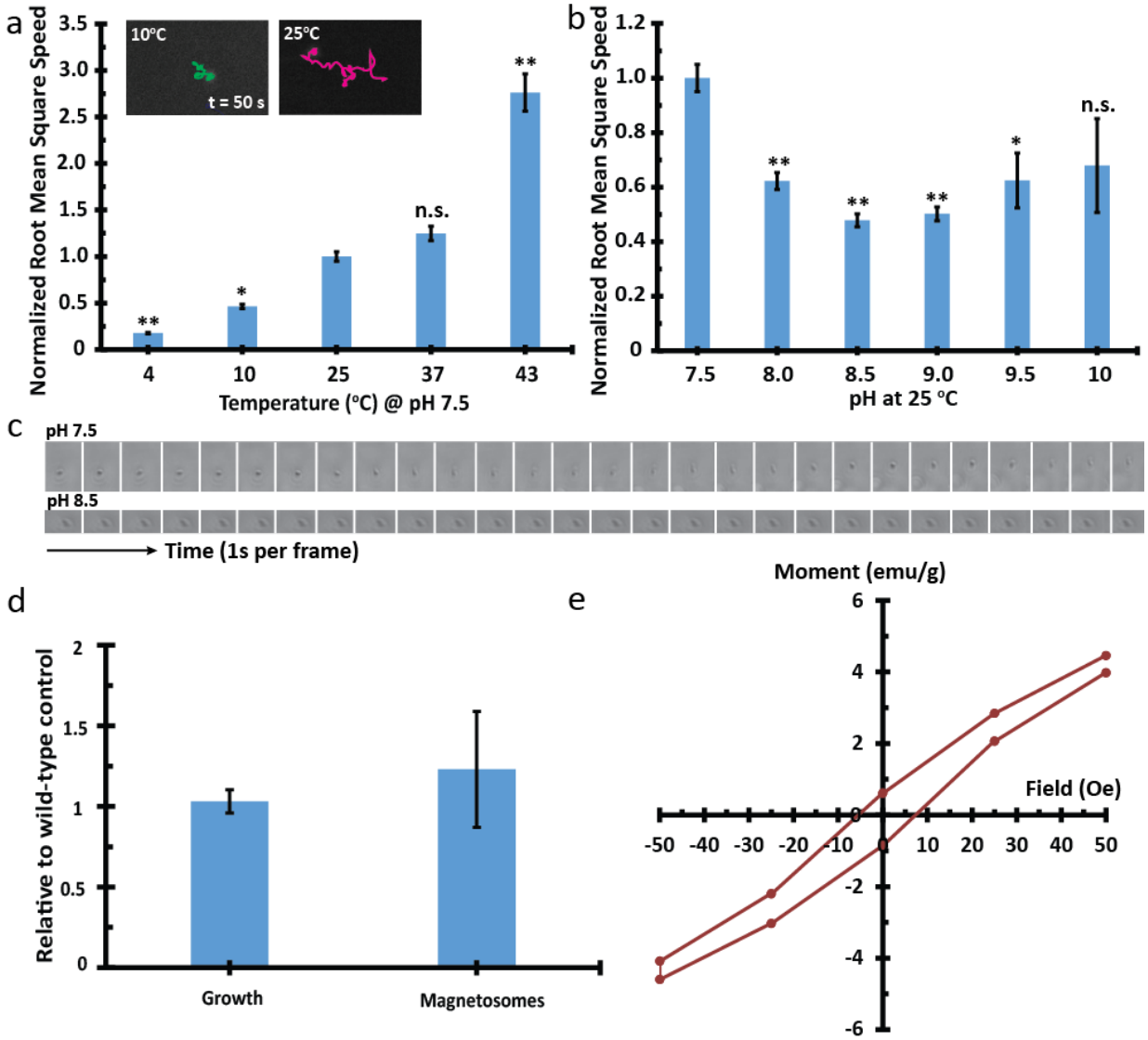

Fig. 2 Modification of flow environment to minimize flagella motion. (**a**) Normalized root mean square speed of AMB-1 at 25 ºC, pH 7.5, and different temperatures. Inserts: tracked trajectories of the AMB-1 at 10 ºC and 25 ºC showing significantly reduced motion in the former condition. n = 20 for each condition. (**b**) Normalized root mean square speed of AMB-1 (to 25 ºC, pH 7.5) at different pH. n = 20 for each condition (**c**) Time lapse image of AMB-1 at pH 7.5 and 8.5 showing reduced motion at the latter condition. No significant difference in (**d**) optical densities after 3 days of culture in normal media and number of magnetosome per cell in AMB-1 treated with 10 ºC media at pH 8.5 for 45 min. (**e**) Hysteresis curves showing AMB-1 are still ferromagnetic even after transient cold/alkaline treatment. (**a-b**) * $p < 0.05$, ** $p < 0.001$ relative to condition at 25 ºC and pH 7.5. **Note**: AMB-1 were cultivated at 37 ºC but normalization was performed at 25 ºC and pH 7.5 as microfluidic cell sorting was performed at this temperature.

5.2.4 Assessing the precision of quantitative estimation of magnetic contents in AMB-1 mutants

We show in **Chapter 4** that by combining random chemical mutagenesis and selection using a magnetic ratcheting platform, we could generate AMB-1 mutants with average (A) 3.0 $\pm$ 0.5, (B)

11.2 ± 3.7 and (C) 25.0 ± 3.5 magnetosomes/bacterium with representative bacteria from these population shown in **Fig. 3a**.

Next, we wanted to characterize the isolation efficiency of the AMB-1 mutants with varying numbers of magnetosomes/bacterium. We found previously with TEM that ~0 % of the AMB-1 mutants with 3.0 ± 0.5 magnetosomes/bacterium, ~15 % of the AMB-1 mutants with 11.2 ± 3.7 magnetosomes/bacterium and ~95% of AMB-1 mutants with 25.0 ± 3.5 magnetosomes/bacterium have more than 20 magnetosomes/bacterium (mutants generated in **Chapter 4**). Hence we expect the same respective percentages of AMB-1 at the selection outlet. **Fig. 3c** shows that the experimentally obtained results, where the locations of 30 individual AMB-1 mutants per condition were tracked from image frames captured with a high-speed camera, were similar to theoretical expectations of ~0 % of the AMB-1 mutants with 3.0 ± 0.5 magnetosomes/bacterium, ~15 % of the AMB-1 mutants with 11.2 ± 3.7 magnetosomes/bacterium and ~95% of AMB-1 mutants with 25.0 ± 3.5 magnetosomes/bacterium.

Lastly, we wanted to determine the isolation efficiency of the microfluidic device in a mixed population of AMB-1 mutants with 11.2 ± 3.7 magnetosomes/bacterium (A) and 25.0 ± 3.5 magnetosomes/bacterium (B) in ratio of 9:1 and 19:1. We then calculated the percentage of cells going to either outlets by tracking the motion of individual AMB-1 (**Fig. 3d**). Cold/alkaline treatments did not affect the growth or magnetosome production rates of these mutants (**Appendix D Fig. 2**). Theoretically, we would expect ~10% and ~5% of the AMB-1 mutants at the selection outlet based on the ratio of (A:B) 9:1 and 19:1 respectively. Experimentally, we observed 13% and 7% of the AMB-1 mutants exiting through the selection outlet which were close to the respective theoretical estimates. This data supports the utility of our magnetic microfluidic platform to

quantitatively estimate magnetic contents in different AMB-1 populations in a fast, cheap and convenient manner.

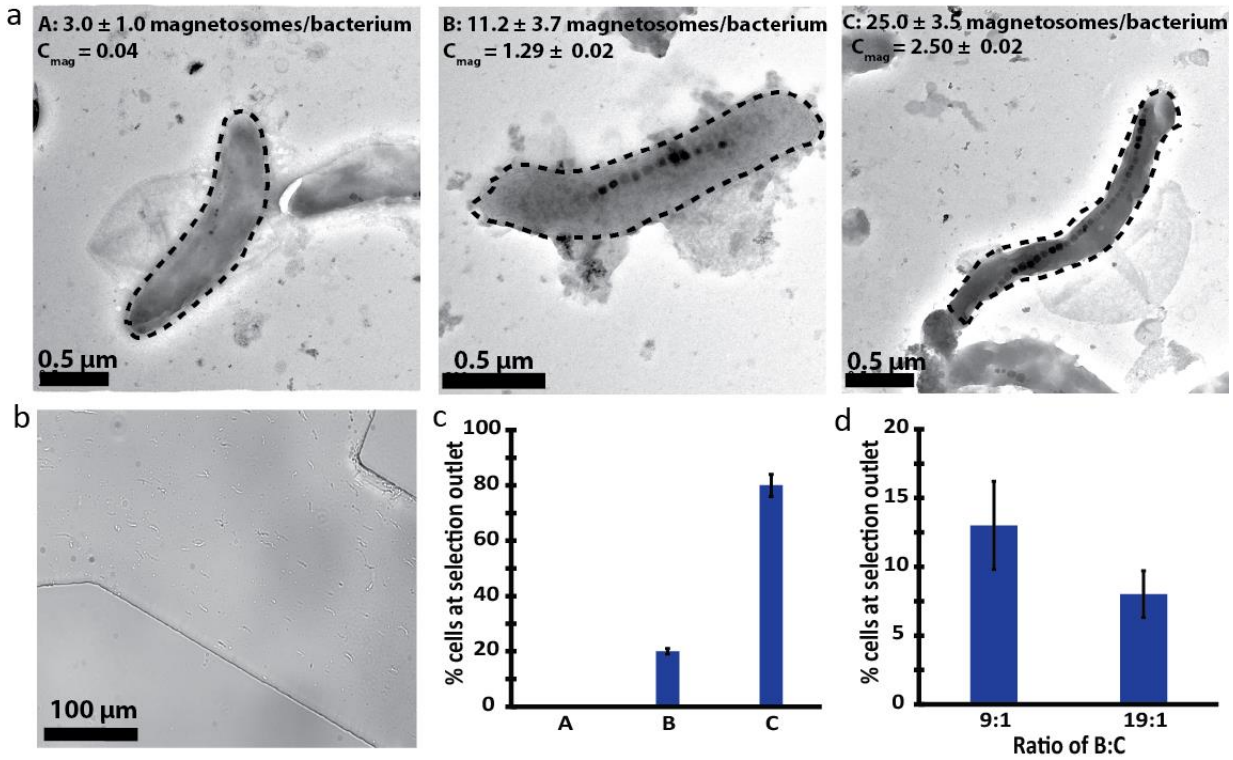

Fig. 3 Assessing the accuracy of quantifying the magnetic contents in AMB-1 mutants. (**a**) Library of AMB-1 mutants with various number of magnetosomes/ bacterium. (**b**) Left: example bright-field image of AMB-1 flowing into the waste outlet for AMB-1 mutants in group A. (**c**) Experimentally obtained results of % of AMB-1 in different groups at the selection outlet (n = 30 each condition). (**d**) Experimentally obtained results after isolating mixed populations of AMB-1 mutants (n = 50 for each condition). A: AMB-1 mutants with 0 ± 0.5 magnetosomes/bacterium. B: AMB-1 mutants with 11.2 ± 3.7 magnetosomes/bacterium. C: AMB-1 mutants with 25.0 ± 3.5 number of magnetosomes/bacterium.

5.2.5 Sorting fluorescent wild-type magnetic MSR-1 from ΔmamAB non-magnetic MSR-1

We also show that the technology can be translated for use with MSR-1 (see experimental conditions in **Appendix D Table 5**), another popular MTB strain. We inhibited flagellar motion of MSR-1 with the cold, alkaline condition and processed the samples through the magnetic microfluidic platform. **Fig. 4a** shows that the MSR-1 population could be distinguished from the 5 µm beads and that most of the MSR-1 were at the dividing/growing phase as they were smaller

than 5 μm. Wild-type (WT) MSR-1 can be isolated at the selection outlet with 71% (WT-GFP) and 80% (WT-mCherry) efficiency while ΔmamAB which do not have magnetic nanoparticles[247] are largely absent from the selection outlet (**Fig. 4b**). Next, we mixed equal numbers of WT and ΔmamAB MSR-1 (at the same optical density, OD) of different fluorescent colors together and sorted them. The isolation purity was high, yielding more than 95% of the WT populations at the selection outlet (**Fig. 4b**). **Fig. 4c** shows the flow cytometry results when WT-mCherry was mixed with ΔmamAB-GFP MSR-1. The population at the selection outlet had 93.7% of WT-mCherry MSR-1 while the waste outlet had 95.3% of ΔmamAB-GFP MSR-1.

5.2.6 Cell cycle synchronization of non-motile ΔflaA MSR-1

MSR-1 populations at the same phase of the cell cycle can provide a better understanding of processes like magnetosome synthesis and segregation. Cell cycle synchronization is typically performed with chemical agents such as Nocodazole or exploiting physical differences in cells like density. However, chemicals can be toxic and affect metabolism in subsequent cell generations.[248] Current physical method such as density centrifugation and counterflow centrifugal elutriation are also not sensitive enough and can exert unnecessary shear stresses on the cells.[248] The method involving continual media change to keep MSR-1 at the growth phase is time-consuming.[249] Longer MSR-1 at the stationary phase are expected to have difficulty overcoming Stokes drag (**Appendix D Table 6**). We show that our technology was able to isolate sub-populations of ΔflaA MSR-1 without flagella (**Appendix D Fig. 3**) with different average lengths (**Fig. 4d, g**) i.e. shorter at the selection outlet (**Fig. 4e**) and longer at the waste outlet (**Fig. 4f**). The OD_{565} of the MTB at the waste outlet after 4 hr (sufficient time only for 1 cell division) were also higher than that in the

selected outlet, showing that a greater proportion of cells in the waste outlet was in the stationary phase (**Fig. 4h**).

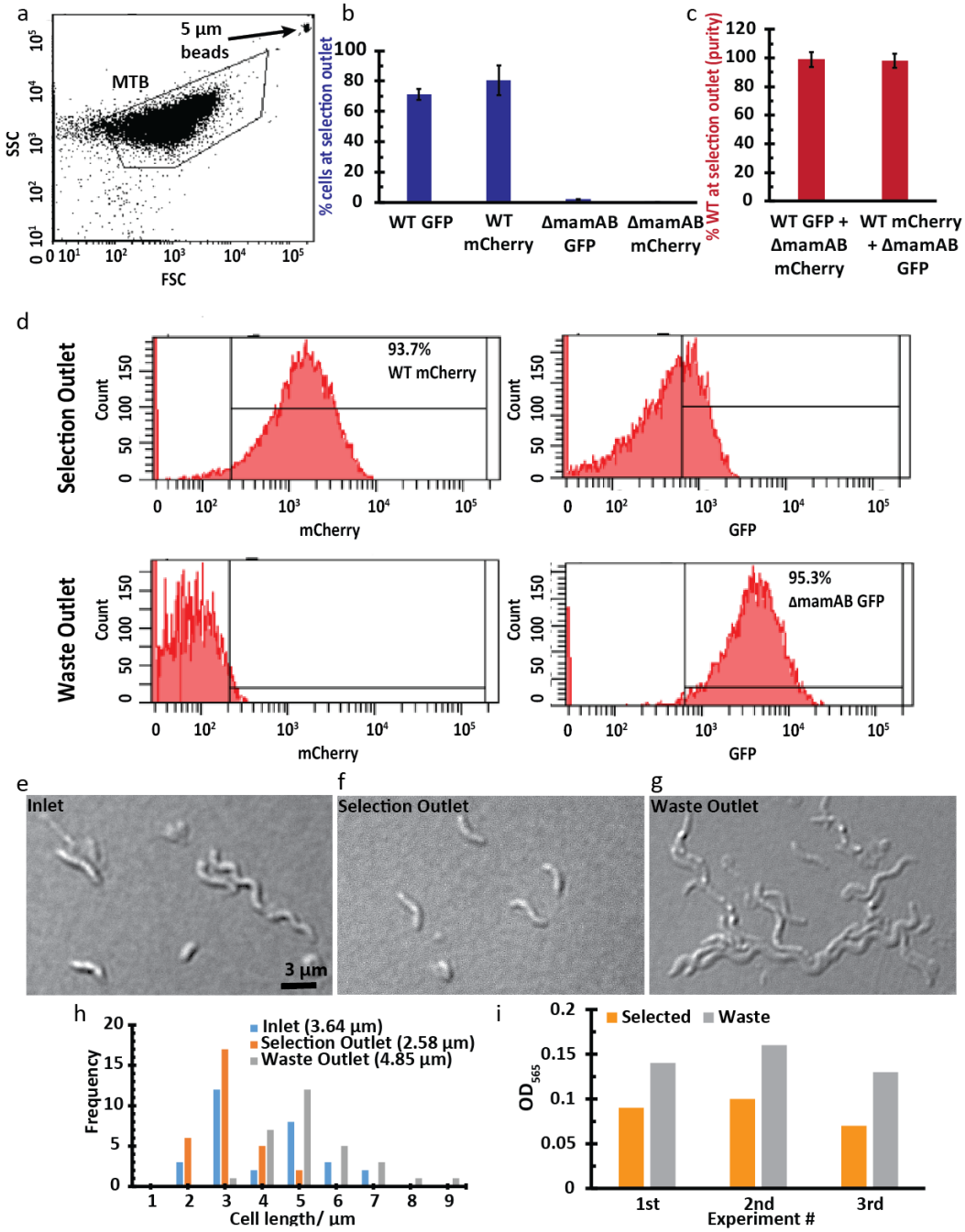

Fig. 4 Applying magnetic microfluidic device for use with MSR-1. (**a**) The gating of MTB population can be distinguished from 5 µm beads and the MTB existed at the dividing phase of cell cycle. (**b**) WT magnetic MSR-1 can be isolated from the selection outlet at high yield (~70-80%) while ΔmamAB non-magnetic MSR-1 are excluded from the selection outlet. A: WT-mCherry mixed with ΔmamAB-GFP; B: WT-GFP mixed with ΔmamAB-mCherry. The isolated cell population at the selection outlet also had >95% of WT MSR-1. (**c**) Example of flow cytometry data from A. Note that as there was bleaching of mCherry signals into GFP signals, it seemed

that there were a high percentage of ΔmamAB-GFP MSR-1 in the selection outlet which was not true. The selection outlet contained 93.7% WT-mCherry MSR-1 while the waste outlet contained 95.3% ΔmamAB-GFP MSR-1. (**d-g**) Cell cycle synchronization of MSR-1. Longer MSR-1 at the stationary phase experience more Stoke's drag and are preferentially isolated at the waste outlet. The length of 30 MTB was measured for each condition. (**h**) OD_{565} of the MSR-1 at waste outlet was higher than that in the selected outlet 4 hr (sufficient time only for 1 cell division) after microfluidic processing.

5.2.7 Parallelized design for microfluidic bioreactor

Multiplexing of microfluidic channels is now a common way to increase the throughput of cell sorting for applications such as cell sorting in a bioreactor where large volume processing is necessary. **Fig. 5** presents a simple design showing how parallelized version of the magnetic microfluidic system may work. This application would also be advantageous as labs are trying to culture MTB in large scale to harvest their magnetosomes for biomedical applications.

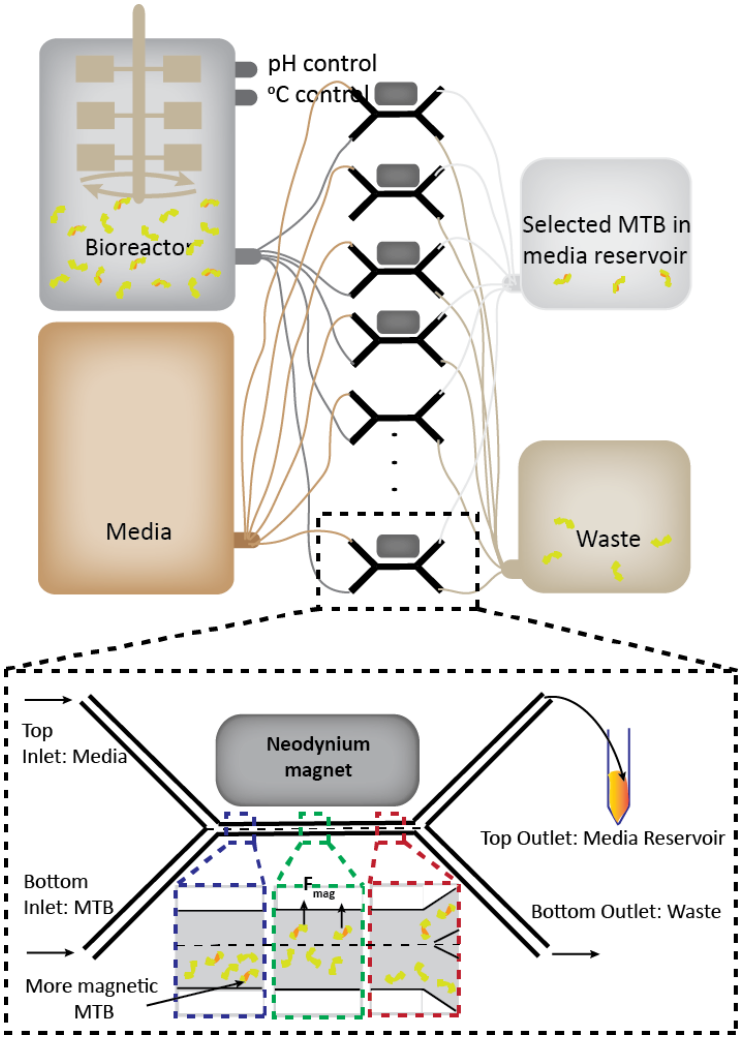

Fig. 5 Design of a microfluidic bioreactor. The magnetic microfluidic platform can be parallelized for large volume cell sorting.

5.3 Conclusions

Here, we designed a simple microfluidic chip for cheap, rapid, semi-automated, objective and quantitative estimation of magnetic content and cell cycle synchronization of MTB. There are a few reasons why we believe this technology can be suitably adopted in microbiology laboratories. Firstly, the device has dimensions with >20 μm dimensions, which makes micro-fabrication simple. Next, there is no need for any sophisticated instruments or protocols to run the process as only syringe pumps are needed to control the flow rates. Therefore, laboratories working on

different MTB strains can modify the flow rates and magnetic field strengths for their specified interests although higher flow rates may reduce the selection efficiency of MTB and require higher magnetic field gradient. We also acknowledge that to serve as a tool for quantitative estimation of magnetic contents in MTB, the operating parameters of the magnetic microfluidic device must first be characterized with a known or physically similar (e.g. shape and size) MTB strain.

The device can also be useful as a means for single cell analysis. By using a slow flow rate in the micro-channel and a diluted MTB suspension, single MTB of interest may be isolated into individual wells in a well-plate for subsequent culture and downstream assays like genome sequencing. We also envisage a highly-parallelized version of this platform to be coupled to a bioreactor for large scale, continual enrichment/selection of MTB mutants of interests.[248] This system would also be useful to investigate the effects of culture environment such as stirring, presence of iron chelator and poly-ethylene-glycol (PEG)[250] and genetic manipulations[221] on magnetosomes production rates.

5.4 Materials and Methods

Micro-fabrication

The mold with its specific channel dimensions (length: 2 cm, width: 500 µm, height: 23 µm) was designed and fabricated using a conventional microfabrication technique.[251] The microfluidic biochips were fabricated by casting a degassed polydimethylsiloxane (PDMS) polymer (mixed in a ratio of 10 : 1, Sylgard 184, Dow Corning, USA) on the patterned wafer and subsequently baking for 2 h at 70 °C. After curing, PDMS was peeled off from the patterned wafer and access holes (0.5 mm) for fluidic inlets and outlets were punched using a Uni-Core™ puncher (Sigma-Aldrich Co. LLC.); then, the PDMS devices were irreversibly bonded to glass using an oxygen plasma

machine (Harrick Plasma) to complete the channels. The assembled device was finally placed in an oven at 70 °C for 2 h to further enhance bonding.

Device characterization with beads

The microfluidic devices were mounted on an inverted phase contrast microscope coupled with a high-speed CCD camera (Phantom v9, Vision Research Inc., USA). The microfluidic chip was primed with buffer (1× PBS, 2 mM EDTA supplemented with 0.5% BSA) using a syringe pump (PHD 2000, Harvard Apparatus, USA) for 2 min at a flow rate of 500 μL min^{-1}. During testing, the beads (1 μm magnetic beads to imitate AMB-1 with 20 magnetosomes and 3 μm polystyrene beads to imitate the size of AMB-1) were filled at a concentration of 1 x 10^7/mL into 10 mL syringes and pumped through the microfluidic device *via* PEEK tubing (0.020'' x 1/32'' x 5, IDEX Health & Science). The flow rate was varied to find the optimized flow ratio and the external magnetic field strength was also varied to optimized selection purity.

Magnetic field measurements

Magnets were set up on Magnetic Cleanliness Chamber and magnets were adjusted to a height such that it is aligned with the center of the Hall magnetometer sensor. The magnetic field strength was then recorded at difference distances.

Culture conditions

AMB-1 (ATCC700264) was grown in magnetic Sprillum growth media (MSGM) supplemented with ferric malate (30 μM) as previously described.[217] For clone selection, AMB-1 was plated onto 0.7% agar. Cultures for C_{mag} measurements or TEM were grown in 10 mL MG medium containing

25 mM HEPES buffer (pH 7.2) and ferric malate under a 10% oxygen atmosphere at 30°C. Mutagenic media also contained 10 µg/mL 5-bromouracil. Color inspection was performed on AMB-1 cultured on agar plate supplemented with ferric malate. AMB-1 treated with 10 ^{o}C media at pH 8.5 for 45 min was centrifuged and re-suspended in normal media. Relative growth rate was determined as a ratio of OD_{600} measured with an Agilent 8000 UV-Visible spectrophotometer. To ensure validity in comparing the isolation efficiency of different AMB-1 mutants, the mutants were all subject to the same growth conditions and processed through the microfluidic device in their growth phase (average length of 3 µm).

All strains of MSR-1 was cultured in hung-gate tube with 2% O_2 in standard MSR-1 media.[252] For cell cycle synchronization experiment, MSR-1 WT was treated with 10 ^{o}C media at pH 8.5 for 45 min to minimize flagella motion, and was centrifuged and re-suspended in normal media before processing through the magnetic microfluidic chip. It is important to have a relatively diluted sample as the MSR-1 have spirillum shapes and may be clustered together which affect the balance of the forces.

Trajectory tracking

AMB-1 was tracked using TrackMate plugin[253] (DoG (difference of Gaussian) detector, 2.0 µm blob diameter, linking: 2 µm, filter: paths shorter than 50 frames were rejected, $\Delta t = 60$ s, $\tau = 1$ s). The raw data was then exported into an excel sheet calculated for root mean square speed (RMSS) using the formula: $RMSS = \frac{1}{\Delta t} * \frac{1}{p-\tau} \sum_{i=\tau}^{i=p-\tau} \sqrt{|(x_{i+1} - x_i)|^2 + |(y_{i+1} - y_i)|^2}$.

Microscopy

MSR-1 was isolated according to the experimental conditions stated in **Appendix D Table 4**. The samples were then centrifuged at 14,000 rpm for 10 min followed by resuspension in leftover media. Liquid agarose (700 µL) was pipetted onto a glass slide and allowed to gel for 30 mins. 5 µL of the sample suspension was then pipetted onto the glass slide before bright field imaging with Olympus IX81 microscope (100x).

Electron microscopy: An aliquot of cell culture (100–500 µL) was pelleted by brief centrifugation (14,000 × g) for 10 min aerobically at room temperature and resuspended in MSGM (~10 µL). The cells were adsorbed onto 400-mesh copper grid coated with Formvar/Carbon (TedPella Inc.). TEM was performed using 120 kV T12 Quick CryoEM with a point resolution of 0.34 nm. High resolution TEM was performed using Titan S/TEM at 200 kV with 0.19 nm resolution. Flagella was visualized after staining with uranyl acetate. Imaging and data processing was performed at the UCLA CNSI Electron Imaging Center for NanoMachines (EICN).

Statistical analysis

Statistical analysis on the mean square speed of the AMB-1 at different temperatures and pH (n = 30 for each condition) was performed using Student's t-test after testing for normality by plotting the data as a bell-shaped histogram. Statistical analysis on the C_{mag} of MSR-1 Δ*flaA* was performed by first testing for equality in variances with F-test followed by using the appropriate t-test for testing differences in mean.

Chapter 6: Outlook for Magnetic Neural Stimulation Techniques

In the previous chapters, I discussed the use of magnetic nanoparticle (MNP)-based technique for acute and chronic neural stimulation, followed by using magnetic ratcheting/magnetic microfluidic platforms for selecting magnetotactic bacteria over-producers for generating high quality MNPs. Nonetheless, the uniformity of MNPs properties is only one of the challenges to overcome to translate magnetic techniques for *in vivo* animal and clinical use. This chapter addresses the other challenges and propose strategies to overcome them.

To deliver magnetic nanoparticle-based neural stimulation technologies for translational research and clinical applications, innovations should be made in three main areas *i.e.* (i) reporters to measure electrophysiological activity in the presence of magnetic fields, (ii) nanotechnology to transduce signals with minimal side effects and (iii) devices to deliver energy with high spatiotemporal resolution.

6.1 Reporters of magnetic stimulation

The first step to validate the usefulness of neural stimulation techniques is to monitor cellular responses during stimulation. The 'gold' standard to monitor electrophysiological activities of neurons is the patch clamp technique. Based on the patch clamp configuration, the activity of single or multiple ion channels can be measured at a time.[19] The solution in the patch pipette can also be modified to contain neurotoxins to block specific ion channels to increase the specificity of the measurement. However, there are major drawbacks in patch clamping.[210] Firstly, it requires an expensive set-up. Next, it has a steep-learning curves as different models and rigs can pose challenges even to the most experienced users. Thirdly, it has extremely low throughput. Although multi-cell patch clamps and microfluidic-based patch clamp electrodes are available, the

throughput is still low compared to newer genetics-based techniques.[254] Lastly, the set-up for patch clamping is not always compatible with the described technologies for remote control of neuronal activities. For instance, any alternating magnetic field that is applied to the neurons leads to interference with the readings from the patch clamp amplifier electronic components.[172] Hence there has been efforts to shift away from patch clamping with major progress in the development of genetically-encoded calcium or voltage sensors.

As intracellular calcium levels are responsible for controlling numerous signaling cascades,[186] there has also been substantial interest to develop indicators with faster response time or fold change in signals. There are various commercially available fluorophores such as fluo-4 and Rho-3 to monitor intracellular calcium levels but they are a few fold less sensitive than GCaMP, a genetic indicator of calcium designed by Chen et al.[193] Different versions of the GCaMP indicators have been used for *in vitro* and *in vivo* studies.[255] There are also other recently developed genetically encoded calcium indicators that offer higher fold change in fluorescence than GCaMP upon calcium binding and they also have shorter response time.[256] Recently, Berlin and co-workers utilized a rational design strategy to develop an even more sensitive photo-cleavable genetically encoded calcium indicators that they claimed can be transferred to other fluorescent proteins using circularly permutated GFP.[257] However, genetically encoded calcium indicators may affect calcium dynamics by buffering calcium, thus affecting processes such as cellular signaling.[258] They are also biased to suprathreshold signals and cannot capture small subthreshold events that affect membrane voltage. Finally, calcium dynamics are confounded by the diffusion rates of calcium.[259]

One other way to correlate electrophysiological responses with remote stimulation is to use genetic indicators of voltage. The Cohen lab has generated a library of genetically encoded voltage

indicators such as QuasAr1 and CheRiff that can be effectively integrated with microscopy to monitor cellular responses.[260] Akemann et al. have also developed fluorescence resonance energy transfer-based voltage sensitive fluorescent proteins that are targeted to the cell membrane for reporting changes in membrane potential.[261] The team has demonstrated the utility of the voltage indicators in the cortices of primary neurons, brain slices and mice models. Nonetheless, there are still challenges to overcome to design better voltage reporters.[259,262] Firstly, as the plasma membrane is thin, the density of embedded voltage indicators is limited. This can limit the fold change in signal. The problem is further complicated by the vulnerability of membrane to disruption due to strong light sources. Secondly, many membranes in the cells are internal membranes and if the chromophores bind indiscriminately to membrane, the background noise will be very high. Next, as the plasma membrane undergoes active remodeling, the addition of chromophores may affect its biophysical properties. Lastly, there is also a challenge to correlate optical signals to voltage signals as there is insufficient knowledge about the biophysical mechanism of voltage sensitivity.

6.2 Nanotechnology

Once the usefulness a magnetic-enabled neural stimulation technique is validated, it is critical to further optimize the properties of the MNPs that are used to generate heat and exert mechanical forces. The main challenges in nanotechnology include synthesizing MNPs with homogenous size, thermal and magnetic properties, minimal aggregation and cytotoxicity, high specificity and ease in crossing the blood brain barrier (BBB).

6.2.1 Microfluidics for magnetic nanoparticle synthesis

Microfluidics technologies can help synthesize NPs with narrower size distributions and reduced batch-to-batch variability.[263–265] The properties of NPs in bulk synthesis may not be uniform as it is difficult to control the mixing time of reagents, reaction temperature and reaction time.[266] However, microfluidic platforms enable rapid mixing with external actuators like stirrers and electric fields and even without external actuators such as by using flow focusing.[213] Furthermore, solvent flow rates and channel geometry can also be modified to optimize NP synthesis in micro-channels.[213] The high spatiotemporal control in microfluidic platforms also facilitate synthesis of NPs with uniform properties necessary for heating[81] or piezoelectric[60] functions.

Another advantage of using microfluidic system is that it uses a low volume of toxic, inorganic solvents and expensive reagents such as antibodies.[267] This can reduce the levels of remaining toxic chemicals and lead to cost savings. This advantage is extremely relevant for biomedical applications where cytotoxicity and specificity of the NPs are important.

However, there are still some challenges to be overcome for using microfluidic systems for NP synthesis.[213] Firstly, the substrate for the microfluidic device is usually composed of poly-dimethly-siloxane (PDMS) that may be not compatible with the temperature and solvent used in NP synthesis. Other substrates such as glass may be considered. Also, although microfluidic systems can potentially be parallelized and perform continuous NP synthesis, their throughput is still limited compared to batch reactors. Therefore, microfluidic platforms may find greater utility for synthesizing specialized NPs such as those for clinical use where there are stricter requirements.

6.2.2 Magnetotactic bacteria for magnetosomes and magnetic nanoparticles

Magnetotactic bacteria (MTB) was first scientifically described in a widely circulating journal in 1975 by Blakemore[268] and since then, there has been increasing number of publications on this class of bacteria that can sense the Earth's magnetic fields for magnetoaerotaxis. Making use of a unique biomineralization process, MTB are able to assemble and precipitate linear chains of magnetite ($Fe(II)Fe(III)_2O_4$) NPs with different shapes (spherical, bullet etc) and sizes (35-120 nm) bound in magnetosomes[217]. Magnetosomes are lipid bilayer-bound organelles that potentially can be used directly to modulate neuronal activities. The diverse chemical groups on the lipid membranes facilitate surface chemistry to increase biocompatibility and specificity.[269]

On the other hand, MNPs can also be released from magnetosomes with mechanical perturbations such as via a French press machine, or treatment with acid or detergent,[270] with steps all possibly performed on a microfluidic chip.[213] MNPs produced by MTB are also reportedly superior than chemically synthesized MNPs as the former have homogeneous sizes and crystallography, possess high thermal stability, have low aggregation and can be easily functionalized using conventional surface chemistry techniques or through genetically-encoded protein fusions in magnetosome-associated protiens.[211]

To tap into the research and commercial potential of biologically synthesized MNPs, the Schüler group manipulated the genetic material of MTB to produce GFP-tagged[271] and antibody functionalized MNPs[214]. However, MTB grow at a slow rate (doubling time of ~4-6 hr[219] compared to 20 min for *Escherichia coli*[220]) and in fastidious conditions[218] as compared to other micro-organisms commonly used in industry. Kolinko et al. attempted to address the growth limitation by transferring 30 key genes from *Magnetospirillum (M.) gryphiswaldense* to *Rhodospirillum rubrum* and first demonstrated the possibility of endogenous magnetization in non-magnetic

organisms using synthetic biology.[218] A similar feat was also demonstrated by Zurkiya et al. who cloned magA into human cell line to endogenously produce MNPs for MRI.[272] Nonetheless, this method has low efficiency as large gene clusters have to be transferred, inserted at appropriate sites and expressed. Furthermore, the cycle of transfection and selection is laborious and has low throughput.[273] Most importantly, the efficiency of this technique relies heavily on our current knowledge on the biomineralization process[273] that remains sparse due to its genetic complexity.[218]

The main drawback of using MTB-produced MNPs is the low production rate. Although various bioreactor designs and media conditions have been created to optimize their growth, the production rate of these biologically produced MNPs is still much lower than chemical synthesis.[212] This has motivated some groups to make use of MTB-inspired method for chemical synthesis of NPs.[274] Gao and co-workers utilized hydrogels as nano-reactors, similar to magnetosome vesicles, for *in situ* fabrication of MNPs.[275] The negatively-charged hydrogel networks facilitate uniform distribution and adsorption of cationic iron ions, followed by subsequent co-precipitation of iron oxide nanoparticles. Further improvements in this technique can boost the production rate while maintaining high quality in MNPs.

6.2.3 Magnetic nanoparticles for crossing the blood brain barrier

In many of the existing magnetic stimulation techniques, MNPs used for *in vivo* work are introduced via cranial windows in mice models or injected directly into the brains of other model organisms. However, for remote control of neuronal circuits to work in *in vivo* and clinical settings, the MNPs should be introduced into the blood stream. The MNPs would then have to cross the blood brain barrier (BBB). The BBB is a passive largely impermeable cellular barrier that is composed of endothelial cells, pericytes and astrocytes that separates the blood from brain

interstitial fluid. The size[276] and surface charge[277] of NPs have been shown to affect their passage through the BBB. Unfortunately, even after optimization, the transport efficacy is still low[278] as the nanoparticles must first be internalized by the endothelial cells followed by intracellular transport and export for uptake by neighboring neural cells.

This has motivated research in the area of receptor-mediated nanoparticle transport where nanoparticles are functionalized with specific peptides to cross the BBB. For instance, Qiao and co-workers coated iron oxide MNPs with poly-ethylene-glycol that was claimed to increase endothelial permeability.[279] The nanoparticles were then coupled with transferrin antibodies that facilitated transcytosis through the BBB. Wiley and colleagues investigated the tradeoff between size (surface area) of the nanoparticles and the number of transferrin molecules on the nanoparticles for sufficient interactions with the transferrin receptors.[280] This research introduced a rational design strategy to optimize nanoparticle composition for transport through BBB. Recently, Clark and Davis also created an acid-cleavage linkage between transferrin and nanoparticles for increased transport of nanoparticles in the brain tissues (parenchyma).[281] In this case, the MNPs would be internalized, transported and exported out of the endothelial cells while the transferrin antibodies remained bound to the receptors. Once inside the endothelium, the transport of the nanoparticle was no longer restricted by the presence of the transferrin peptides that might interfere with transport due to non-specific interactions, size and surface charge. Innovation is definitely warranted in the creation of multi-functional magnetic nanoparticles coated with biocompatible polymers, ferritin and other ion channel specific antibodies to simultaneously reduce cytotoxicity, increase brain uptake and specificity for interfacing with the brain.

Capitalizing on the magnetic properties of MNPs, a few groups have also demonstrated the possibility of guiding MNPs through the BBB with magnets.[282] Kong and co-workers made use of magnets from companies namely Dexter Magnetic Technologies and K&J Magnetics, Inc. to influence the spatial distribution of MNPs in the brain tissues.[283]

Another way to overcome the issue of BB is to produce iron-based MNPs intracellularly. The possibility of this strategy was first demonstrated by Stanley et al.[170] who genetically engineered cells to express superparamagnetic ferritin fusion proteins that localized near the cell membrane. Upon stimulation proinsulin release could be induced. Recently, the same group made use of this strategy to manipulate glucose sensing neurons respond to induce/inhibit feeding behaviors in mouse.[172]

6.2.4 Minimizing cytotoxicity from magnetic nanoparticles

While MNPs may induce cytotoxicity, various strategies may be employed to minimize or overcome this problem: (**1**) MNPs may be coated with biocompatible polymers such as PEG,[81] chitosan and starch that have been shown to minimize cytotoxicity or even confer neuro-protection.[58] It will be challenging but extremely useful to create multi-functional MNPs that minimize cytotoxicity, facilitate targeting to specific cells and enable crossing of the blood brain barrier;[284] (**2**) The size of the MNPs is also known to influence cytotoxicity, with smaller MNPs being more cytotoxic.[285] This may be a concern for thermal-based neural stimulation techniques which typically exploit the superparamagnetic properties of MNPs in the 10-50 nm range to generate heat.[80] However, magnetic-based techniques normally utilize MNPs in the 100-250 nm range which is known to be less cytotoxic than their smaller counterparts.[58] It is also well-documented that the size of MNPs affects their renal clearance, supporting that it is a good

parameter to optimize to minimize cytotoxicity;[286] (**3**) Many other properties of the MNPs (zeta potential, compositional purity etc) and cell types (presence of specific surface antigens etc) are also known to influence MNP-cell interactions, and thus cytotoxicity. Recently, Tay et al. found that older neurons have poorer metabolism for exocytosis and intracellular trafficking of MNPs, resulting in higher net localization of MNPs with lysosomes.[168] This led to increased intracellular free iron ion concentration and cytotoxicity, highlighting the age-dependence of nano-therapeutics. MNP-associated cytotoxicity is a highly interesting and biologically relevant field of study to advance the use of MNPs beyond laboratories. However, due to the focus of this review, we can only briefly mention some of these strategies and we encourage readers to refer to more extensive reviews on this topic:[287–289]

6.3 Energy delivering devices

Finally, it is important to consider the technology to deliver alternating or static magnetic fields to activate MNPs for remote modulation of neuronal activities. The approved human exposure limit to static magnetic fields by the US Food and Drug Administration is 4 T for the entire body which allows for a sufficient magnetic field gradient to be established for clinical applications.[290] This is crucial to overcome the weak interaction between magnetic fields and biological molecules.[58]

There are a few possible configurations to generate strong, localized magnetic field gradients for deep tissue penetration. Beside the use of electromagnet coil, a Halbach array consisting of a matrix of permanent magnets can be employed to augment the localized magnetic force.[291] Current advancement in device designs often deals with modelling the penetration and interaction of magnetic fields due to various magnet arrangement or coil designs through the brain. A useful resource would be to look at the devices that magnetic resonance brain imaging and

transcranial magnetic stimulation are using. Bonmassar and colleagues created a micro-magnetic stimulation coils to generate specific neural responses based on the magnitude and orientation of the coils.[292] Recently, Oxley and co-workers fabricated a passive stent recording array within a vein to stimulate and monitor brain activity using electric fields. A similar concept using their fabrication techniques but to generate high magnetic gradient locally can be applied for MNP-based neural stimulation.[293] **Fig. 1** shows the summary of the challenges of progress of MNP-based neural stimulation techniques.

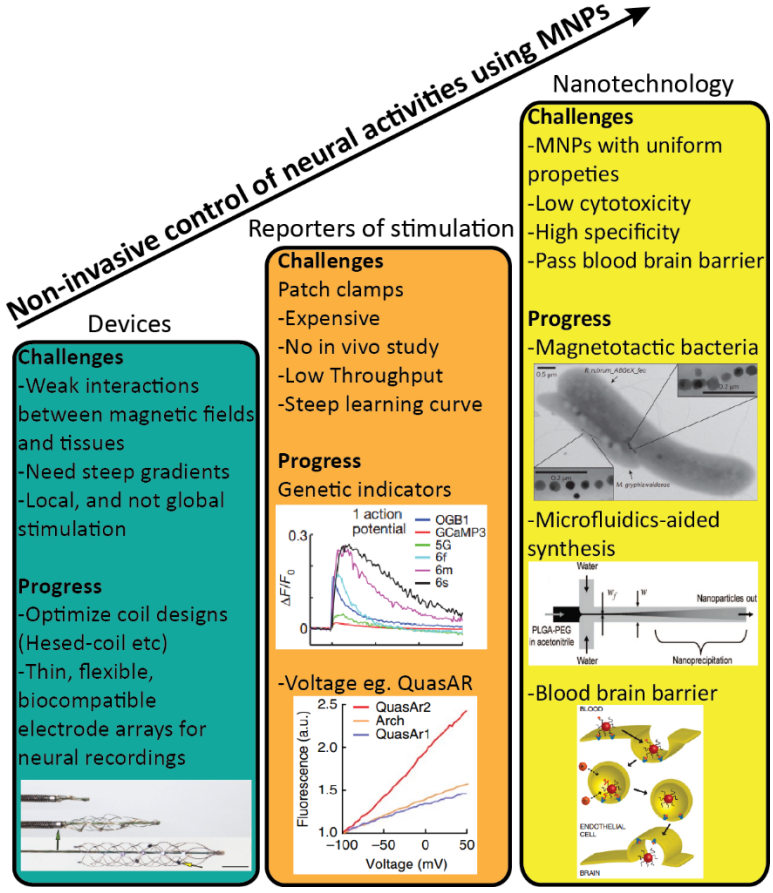

Fig. 1 Challenges and progresses for MNP-based neural stimulation techniques. Innovations can be made in 3 main areas *i.e.* device designs to provide localized stimulation, validation tools with genetically encoded calcium and voltage indicators to increase measurement throughput and nanotechnology for well-controlled synthesis of MNPs with uniform properties, low cytotoxicity and high localization specificity in the brain. Reproduced with permission from [293, 193, 260, 218, 265, 281] in order (left to right, top to bottom).

6.4 Conclusions

Magnetic platforms for remote modulation of neuronal circuits can enable study of brain development and diseases that further our understanding of the complexity of the brain. MNPs can be combined with different energy sources to stimulate neurons with high spatiotemporal resolution and usually with controllable dosage. To further develop the described platforms, it is paramount to correlate stimulation with electrophysiological states of the neurons with patch clamp or genetically encoded voltage or calcium sensors. Furthermore, the synthesis of MNPs can also be improved using microfluidics and genetically modified MTB to produce multi-functional MNPs with narrower size distribution, uniform thermal and magnetic properties, low cytotoxicity, high specificity and ease of traversing the blood brain barrier. Although these challenges are not easy to overcome, great progress has been made in areas like antibody functionalization to facilitate specific cell targeting and passing of blood brain barrier, and controlling the size/zeta potential/coating of MNPs to minimize cytotoxicity. These successes demonstrate the feasibility of *in vivo* neural stimulation mediated by MNPs. With rising investments in brain-related initiatives worldwide, the field of wireless magnetic control of neuronal activities is expected to attract more attention as we gain greater knowledge in genetics, nanotechnology and neuroscience.

Appendix A

Supporting information for Chapter 2

Table 1 Starch/chitosan coated NPs for brain research

Nanoparticles	Use	Ref
Chitosan-coated	Reduce damage to membrane integrity, secondary oxidative stress and lipid peroxidation in neurons following acrolein-induced cell injury	294
	Delivery of estradiol for brain stimulation	295
	siRNA delivery for neurodegenerative diseases	296
Starch-coated	Contrast agent for magnetic resonance imaging with low cytotoxicity	297

Chitosan- and starch-coated iron oxide magnetic nanoparticles (MNPs) were chosen for a variety of reasons. Firstly, they are commercially available at different sizes, fluorescently labeled and can form stable, monodispersed suspensions even in cell media. Secondly, the properties of the nanoparticles used here have been well characterized by other authors (chitosan[54,298–300], starch[53,54,301]) for drug delivery and phagocytosis. Lastly, chitosan and starch coated nanoparticles have been suitably employed in brain-related biomedical interventions as shown in **Table 1**.

Table 2 Characterization of MNPs

Nanoparticle	Condition	Hydraulic diameter (nm)	Poly-dispersity index	Zeta potential (mV)
Starch-coated 100 nm	PBS	166 ± 10	0.187	73.0 ± 11
	Media	150 ± 2	0.232	-33.0 ± 9
	Conditioned media	209 ± 9	0.203	-30.9 ± 2
Chitosan-coated 100 nm	PBS	468 ± 16	0.186	-35.5 ± 20
	Media	442 ± 14	0.138	-32.3 ± 5
	Conditioned media	588 ± 31	0.213	-21.0 ± 7

Zeta potential measurements were made at pH 7.01 and at least 5 readings to calculate the average values

Interestingly, although chitosan-coated MNP had a larger hydraulic diameter than its starch-coated counterpart, the cortical neural network had larger uptake of the former as confirmed with flow cytometry (**Fig. 2a**) and microscope imaging. This could be attributed to the zeta potential of the chitosan-coated MNP being less negative and had more favorable interactions with negatively charged cell membrane.[158] In light of this observation, we propose the importance of measuring the properties of the NPs in conditioned media as the cells might secrete proteins into the media that influence the protein corona[157] (as evident in the difference in hydraulic diameter and zeta potential as shown in **Table 2**), and ultimately, endocytosis.

Table 3 Properties of different mechano-sensitive ion channels

	TRPV1	**TRPV4**	**TRPA**	**TRPC**	**TRPM**	**PIEZO2**	**KCNK**	**N-type calcium channel**
Role in neurons	Nociception	Osmo/pain-sensing	Nociception	Sensation	Nociception	Hearing, touch, pain	Neurite elongation	Dendritic branching
Related neurological diseases	Pain, neuropathy	Seizures,	Pain neuropathy	Late onset Alzheimer's	Pain neuropathy	Marden-Walker syndrome	Epilepsy	Fragile X syndrome
Ion selectivity	No	No	No	No	No	No	K^+	Ca^{2+}
Location in brain or type of neurons	DRG (thalamus)	DRG (thalamus)	DRG	Purkinje cells	DRG	DRG	All neurons	Synaptic terminals and cell bodies
Density in brain	Low	High	Low	High	Low	Low	High	High
Location out of brain	Bladder, lungs, skin	Bladder, lungs, skin,	Hair cells	Intestines, heart, retina	Eye, kidney,	Kidney, bladder,	Retina, spinal cord	N.A.
Inhibitors	Ruthenium red, GSK compounds	GSK219837, RN1747, HC067047	Ruthenium red, AP18, HC030031	2-APB, SKF96365, hyperforin	Sphingosine, FTY720	Phosphoinosisitides, GsMTx4	Serotonin, low pH, halothane	ω-conotoxin
Heat sensitivity	Yes	Yes	Disputed	Unknown	Yes	No	Yes	No
Light sensitivity	No	No	No	Yes	Yes	No	No	No
Acid sensitivity	Yes	Yes	Yes	No	No	No	Yes	No
Voltage sensitivity	No	No	No	Yes	No	Yes	Yes	Yes
Mechanical sensitivity	Unknown	Yes	Unknown	Unknown	Unknown	Yes	Yes	Yes
Activation by (A) tether or (B) lipid bilayer or (C) unknown	A	A	A	A, B	A	B	B	C
References	[302], [303], 166	[303], [304]	[303], [304]	[303], [304], [305]	[303], [304], [306], [307]	[308], [309], [310]	[311], [312]	207

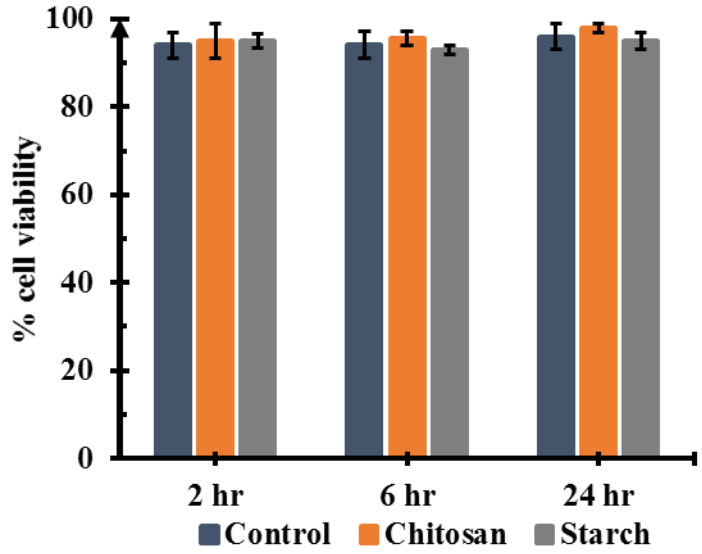

Fig. 1 A live-dead assay for measuring cell viability of 2-week-old cortical neural networks as a function of time. Chitosan- and starch-coated fMNPs had minimal cytotoxic effects on cell viability up to 24 hr. Reproduced with permission from the American Chemical Society.

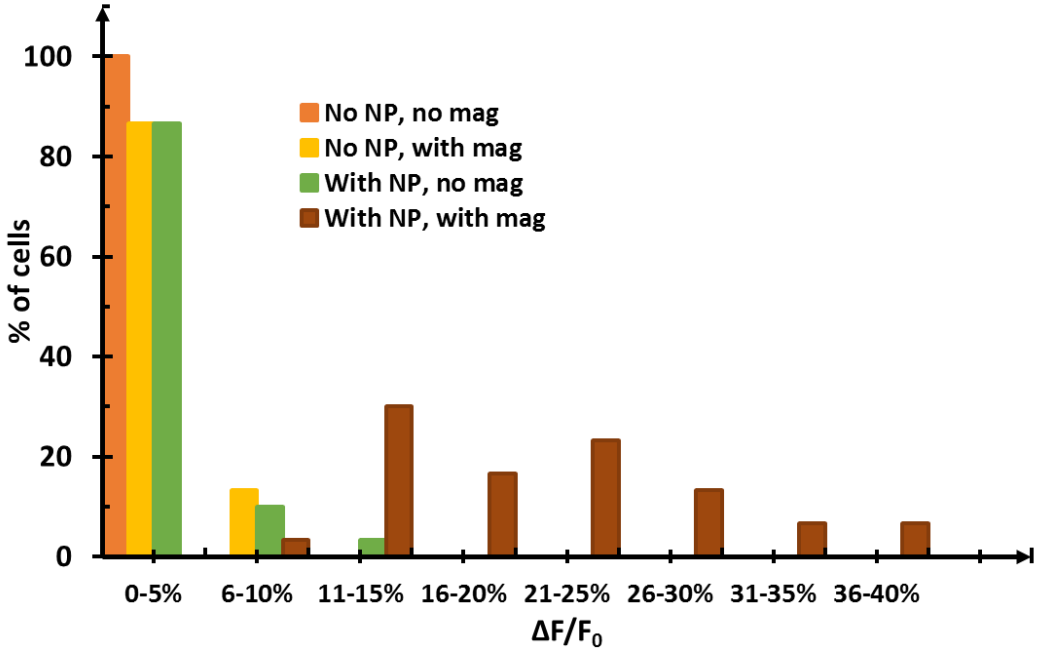

Fig. 2 Population study of 120 neurons from 3 trials. A larger % of the neuron population stimulated with nano-magnetic forces showed greater % $\Delta F/F_0$ compared to unstimulated neurons. Reproduced with permission from the American Chemical Society.

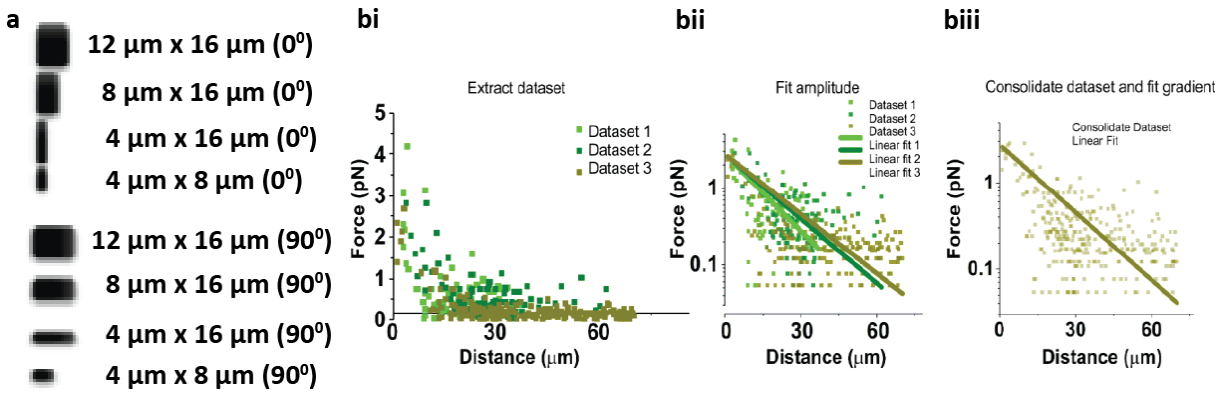

Fig 3 Calculations for magnetic forces. (**a**) Schematic for the size and orientation of magnetic elements. (**b**) Logarithmic fit showing in (**i**) the experimentally obtained values, (**ii**) logarithmic fitted values for individual color-coded dataset shown in (**i**) to show minimal standard deviation and (**iii**) logarithmic fit for consolidated dataset (Note: y axis is logarithmic scale). As there is significant decay of magnetic field, we only considered magnetic forces on cell bodies of neuron within 20 µm away from the magnetic elements. **Fig. 3b** is reproduced with permission from American Chemical Society. Reproduced with permission from the American Chemical Society.

Example to calculate magnetic force

As the MNPs-induced forces are calculated based on measurements with 1 µm micro-particles (MMPs), we can use equation 1 for scaling the force conversion.

$$F_{MNP} = F_{MMP} * \frac{M_{sat,MNP}.\rho_{MNP}.\%core_{MNP}.r_{MNP}{}^3}{M_{sat,MMP}.\rho_{MMP}.\%core_{MMP}.r_{MMP}{}^3} \qquad \textbf{Equation 1}$$

	Commercial name	**% iron in core**	**Density**	**M_{sat}**
NMP	screenMAG	63	1.25 g/cm^3	41.5 mT
MMP	nano-screenMAG	45.5	2.25 g/cm^3	3.8 mT

In supplementary information (**Fig. S4**) of **ref [54]** (reproduced as **Fig. 3b** in this document), Kunze et al. showed that **equation 2** provided the best fit for magnetic force calculation between experimental and fitted values where A_0 is the vertical axis intercept *i.e.* at 0 µm away from the magnetic elements (dimensionless) with the logF axis and C the force gradient over µm.

$$\log \frac{F(x)}{pN} = A_0 + \frac{C}{\mu m} x \qquad \textbf{Equation 2}$$

The table below shows the value for f and C with the highest R-squared value for a logarithmic fit.

Size (rotation) of magnetic elements	**A_0**	**C/ µm**	**R-squared value for regression fit**
12 µm x 16 µm (0^o)	0.44	-0.0260	0.6561
8 µm x 16 µm (0^o)	0.35	-0.0509	0.6561
4 µm x 16 µm (0^o)	0.15	-0.0322	0.7056
4 µm x 8 µm (0^o)	-0.10	-0.0076	0.6400
12 µm x 16 µm (90^o)	0.70	-0.0394	0.5329
8 µm x 16 µm (90^o)	Pattern was not magnetized as was not characterized. No force calculation was made based on this element.		
4 µm x 16 µm (90^o)	0.28	-0.0388	0.6241
4 µm x 8 µm (90^o)	0.40	-0.0308	0.6084

Now, we consider the force acting on the cell body of a neuron 10 µm away from the magnetic element 12 µm x 16 µm (0^o) due to a single 1 µm MMP.

From **equation 2**, we can calculate $F(x)$ where x is 10 µm, this gives us:

$$\log F(x)/pN = 0.44 + (-0.0260/\mu m)(10)$$

$$F(x = 10\ \mu m) = 10^{0.44-0.26}$$

$$F(x = 10\ \mu m) = 1.514\ pN$$

Next, consider that the MNP cluster on the cell body of the neuron to be 1.6 µm .We can then make use of **equation 1** to know the magnetic force due to the MNPs.

$$F_{MNP} = F_{MMP} * \frac{M_{sat,MNP}.\rho_{MNP}.\%core_{MNP}.{r_{MNP}}^3}{M_{sat,MMP}.\rho_{MMP}.\%core_{MMP}.{r_{MMP}}^3}$$

$$= 1.514 * \frac{41.5*1.25*0.63*(1.6)^3}{3.8*2.25*0.455*(1.0)^3}$$

$$= 1.514 * 34.4$$

$$= 52\ pN$$

Lastly, we can add up the magnetic forces due to each MNP cluster on a cell body of a neuron and create the graph shown in **Fig. 5c**.

Note that with this method, we did not consider that magnetic forces acting on the neurites as the neurites are extensively branched and it was not possible to identify individual neurite. Additionally, the cell body with a larger volume could accommodate more calcium entry and typically, calcium ions from the cell body are transported to the neurites. Therefore, summing the magnetic forces only of the cell bodies and relating them to the respective change in fluorescent calcium signals is a reasonable way to understand the relationship between forces and degree of calcium influx.

Appendix B

Supporting information for Chapter 3

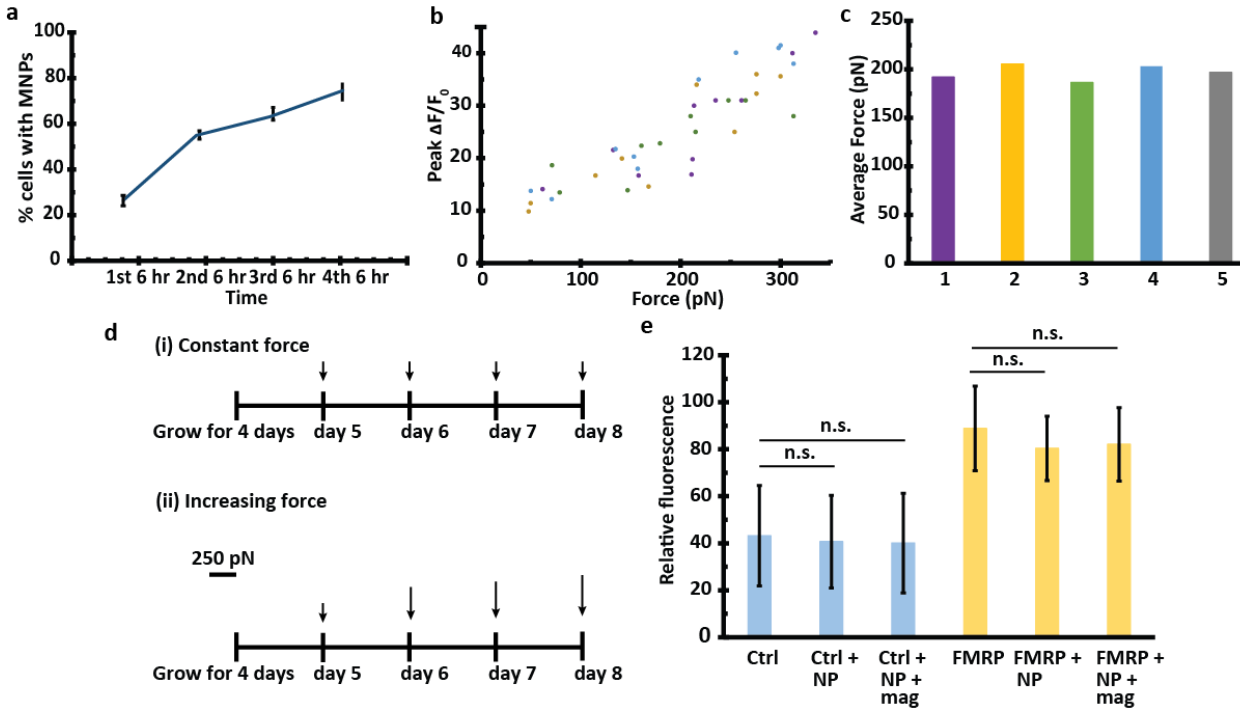

Fig. 1 Average force calculation for chronic magnetic stimulation. (**a**) Neuron-MNP association over time was determined by flow cytometry. (**b**) The plot of peak $\Delta F/F_0$ against forces for different color-coded trials. (**c**) Average force for each color-coded trial in (**b**) was calculated and the average of the averages was ~200 pN. This force was calculated based on neurons incubated with MNPs for 6 hr. (**d**) Schematic for different configurations of chronic magnetic stimulation. (**i**) Neurons were incubated for 6 hr with MNPs once and then stimulated for the next 4 days with an average force of 200 pN. (**ii**) Neurons were incubated for 6 hr daily before stimulation with a magnet for 4 days. At day 5, the average force was 200 pN when 34.8% of the neurons interacted with MNPs. At day 8, when 75.5% of the neurons interacted with the MNPs, the average force on the network was 75.5/34.8 * 200 = 434 pN. (**e**) Chronic stimulation of the neurons with constant magnetic force did not lead to significant change in ion channel expression, possibly because the force amplitude was too low. We hence introduced a new configuration i.e. chronic magnetic stimulation with increasing force (**dii**) which we used in **Fig. 1-2**. We also found that when we stimulated the neurons with 600 to >1000 pN of force daily (with a stronger magnet and/or increased MNP dosage), cell viability decreased significantly due to induced cytotoxicity[168] or there was cell displacement in the former. Reproduced with permission from the American Chemical Society.

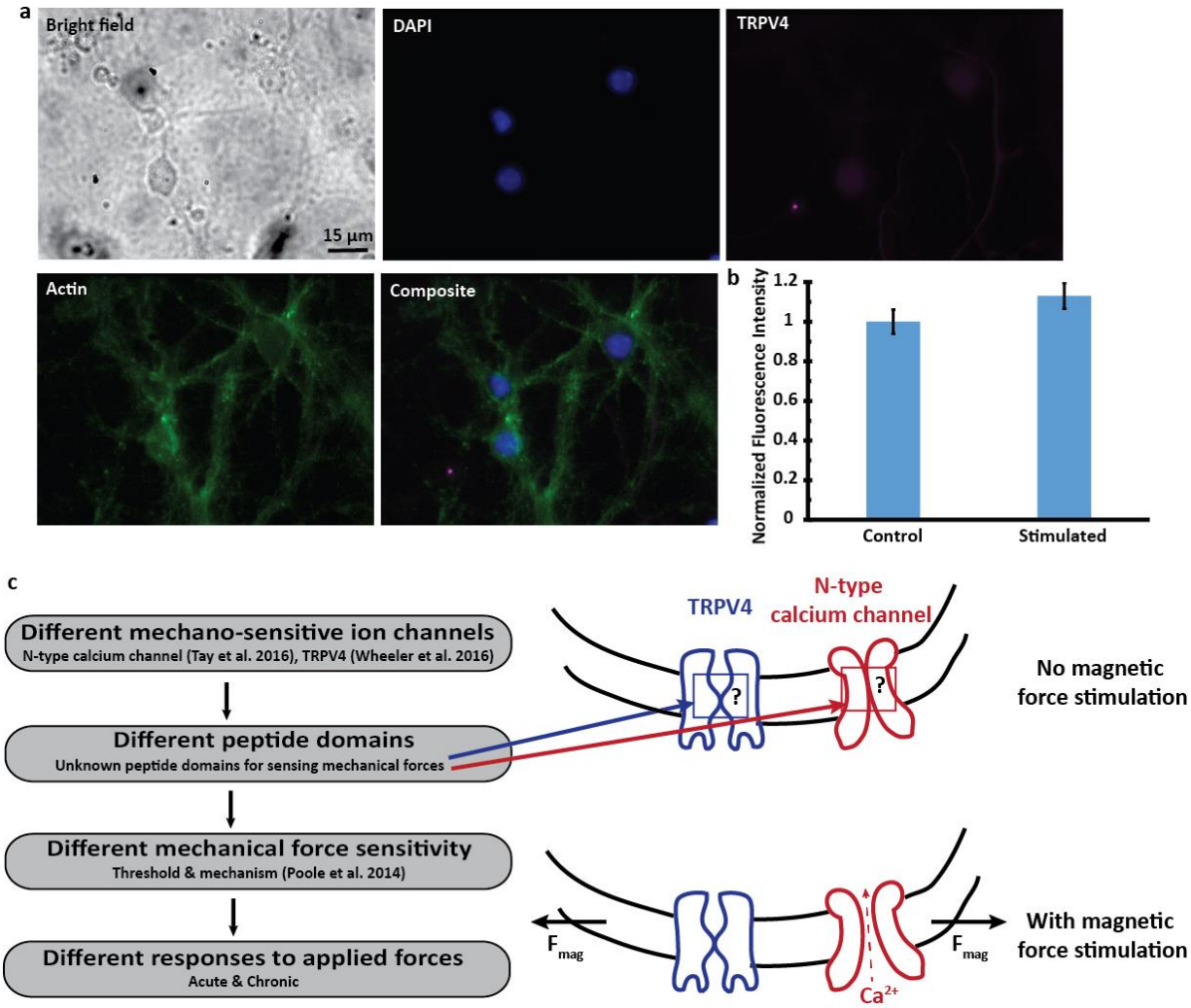

Fig. 2 Model for magnetic stimulation. (**a**) Cortical neurons express a low number of TRPV4 ion channels. (**b**) Chronic stimulation did not affect the expression of TRPV4 ion channels at day 12. (**c**) The only 2 types of mechano-sensitive ion channels that have been reported for use in magnetic neural stimulation are N-type calcium channels[58] and TRPV4.[313] Currently, the peptide domains responsible for sensing mechanical stimuli are unclear. In addition, the threshold and mechanism for activating different mechano-sensitive ion channels are not known. These ion channels may respond to mechanical stress in or out of plane which may be investigated by using the micro-fabricated substrate described in [[314]]. These investigations can then allow us to understand the differences amongst mechano-sensitive ion channels and offer room for ion channel specific mechano-activation. Reproduced with permission from the American Chemical Society.

Appendix C

Supporting information for Chapter 4

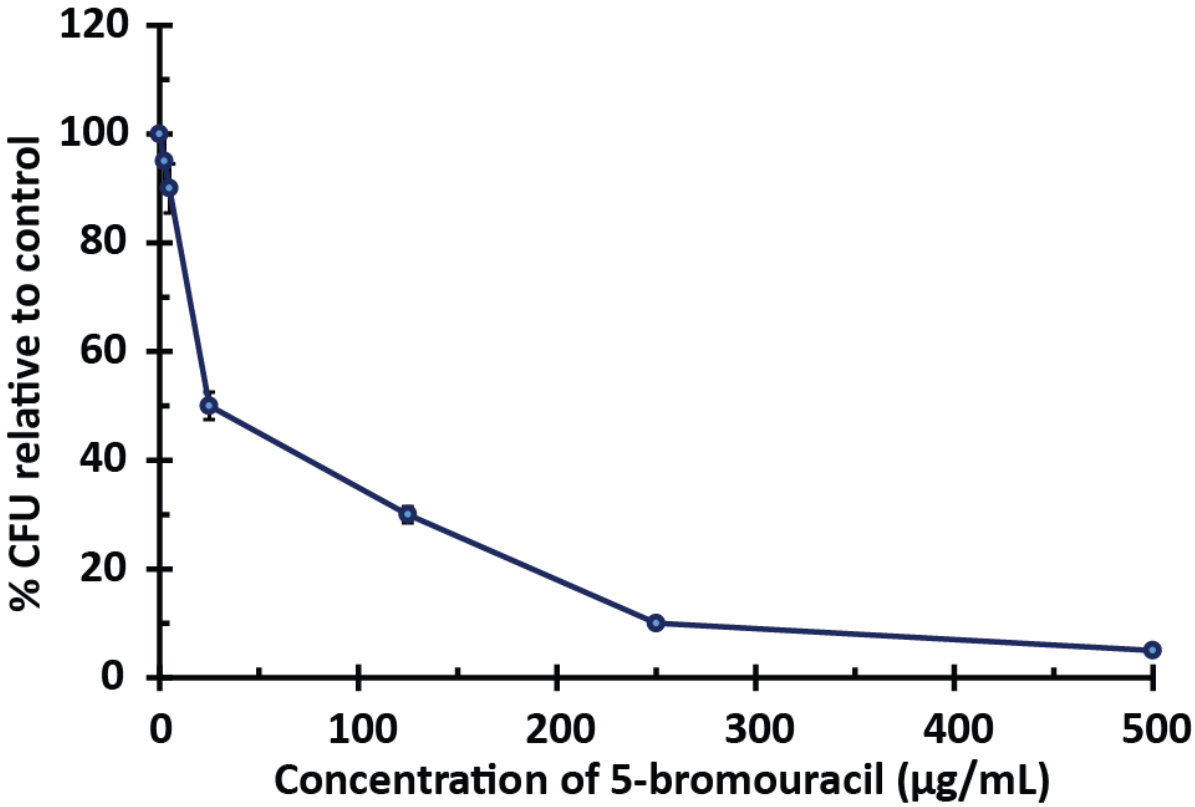

Fig. 1 Plot of cell survival for increasing concentration of 5-bromouracil (5-BU). At higher concentration of 5-BU, many mutants were non-viable, resulting in a low survival rate and CFU count. Taking into account the slow growth rate of the AMB-1, we decided to make use of 10 µg/mL of 5-BU that yielded ~80% survival rate. For the mutation-selection cycle, we cultured the AMB-1 in media supplemented with 10 µg/mL of 5'-BU for 8 days to provide the selection pressure to select for mutants that are also faster growing as slower growing mutants may not be as useful in long term cultivation. Of these mutants we then selected more magnetic mutants (through magnetic ratcheting-based selection).

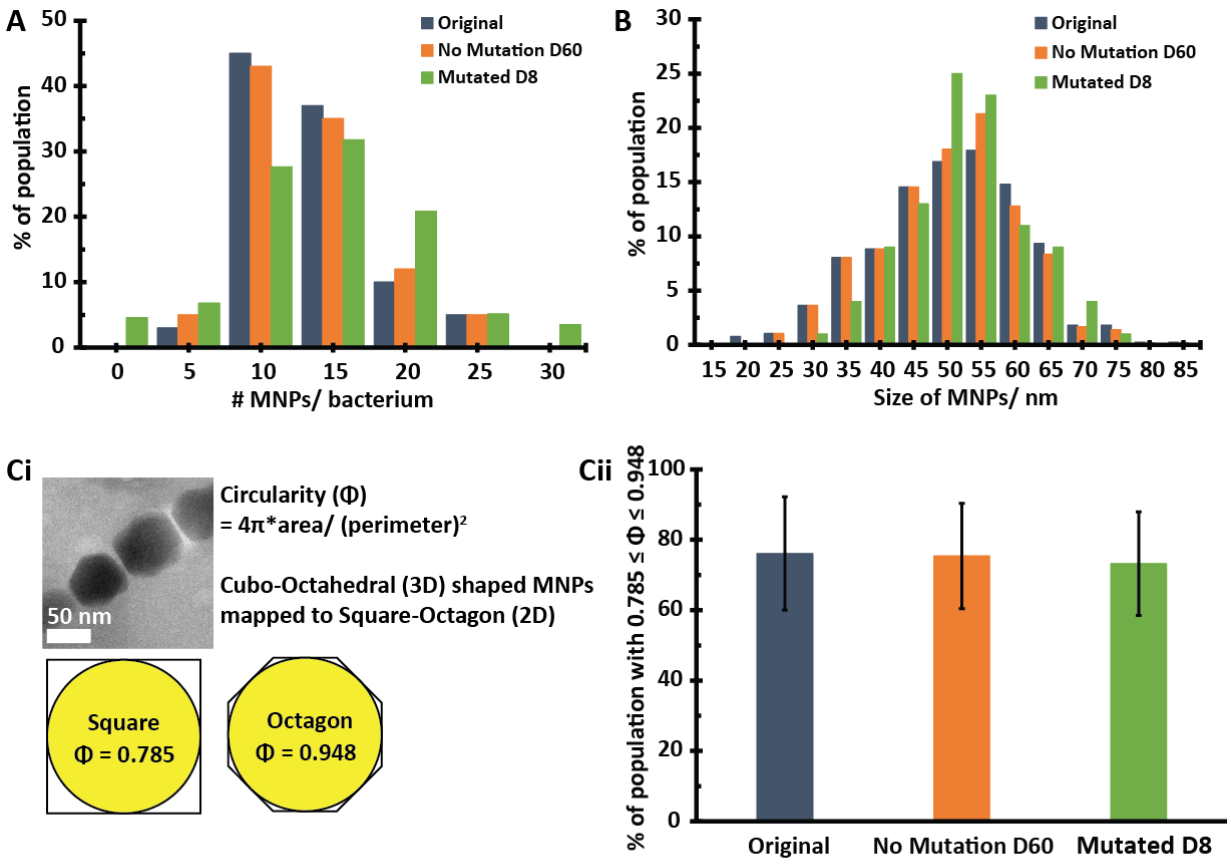

D

	% bacteria with > 25 MNPs/ bacterium	Size of MNPs (avg/ sd)	% MNPs with 0.785 ≤ Φ ≤ 0.948
Original	5.0 ± 0.3 %	48.5 ± 12.1	78.0 ± 11.3 %
10 µg/mL 5' BU for 8 days	8.1 ± 2.5 %	53.5 ± 10.4	75.3 ± 14.5 %
10 µg/mL 5' BU for 12 days	7.6 ± 0.5 %	54.0 ± 11.2	71.6 ± 16.2 %
10 µg/mL 5' BU for 16 days	Irregularly shaped MNPs		

Fig. 2 Random mutagenesis with 5-bromouracil broadened the population of AMB-1 mutants producing different quantities of MNPs/bacterium. (**A**) Growing AMB-1 with 10 µg/mL 5-bromouracil for 8 days generated mutants with a broader distribution of MNPs/bacterium while that of the population grown for additional 60 days without any mutagenic treatment did not show a significant difference in MNPs/bacterium. (**B**) The size distribution of MNPs was not affected significantly by mutagenesis. (**Ci**) As the 3D shape of MNPs produced by AMB-1 has cubo-octahedral character - in 2D projections (square and octagon), the circularity is estimated to be between 0.785 and 0.948. (**Cii**) The circularity within this range for the MNPs was not affected significantly by mutagenesis. (**D**) Optimization table summarizing the effects of mutagenesis on MNP production (number, size and shape) to identify a suitable duration for treatment with 5-bromouracil for sufficient mutation to occur.

Design of magnetic ratcheting platform

Table 1 Definitions and values of parameters

Parameter	Definition	(Value) Unit
V_p	Magnetic volume of particle	m^3
$\Delta\chi_p$	Difference in magnetic susceptibility between particle (x_p) and medium (x_0)	(0.0072) (dimensionless)
u_0	Magnetic permeability of free space	$(4\pi * 10^{-7})$ $kgms^{-2}A^{-2}$
B	Applied magnetic field	T
F_{den}	Magnetic force density of a local magnetic field $= (B.\nabla)B$	$kg^2A^{-2}s^{-4}m^{-1}$
x	Particle location in horizontal (x) axis	m
P	Pillar pitch	m
ω_{ext}	Ratcheting frequency	s^{-1}
t	Time	s
v	Velocity	$\sim 10^{-6}$ m s^{-1}
L	Length	$\sim 10^{-3}$ m
ν	Dynamic viscosity of water (25 °C)	$(8.90*10^{-4})$ $kgm^{-1}s^{-1}$
r_p	Effective radius of bacterium	$(2*10^{-6})$ m
$\bar{u}_p$	Averaged particle speed	m s^{-1}

The movement of a superparamagnetic particle such as the MNPs produced by AMB-1 magnetotactic bacteria in an aqueous medium is governed by the magnetic force equation as shown in **Equation 1.**[315] Here, we derive a formulation to describe how objects with different magnetic content will equilibrate in regions of different pitch between permalloy micro-pillars as a function of a critical ratcheting frequency.

$$F_{mag} = \frac{V_p \Delta\chi_p}{u_0}(B.\nabla)B \qquad \textbf{Equation 1}$$

In our magnetic ratcheting setup (**Fig. 1A**), the particles are ratcheted from left to right (in the positive x direction) due to the horizontal force i.e. F_x. The particle location is thus modeled as a travelling wave as shown in **Equation 2** where $F_{den} = (B.\nabla)B$.

$$F_x = \frac{V_p \Delta \chi_p}{u_0} F_{den} * \sin(\frac{2x}{P} - 2\omega_{ext} t) \qquad \textbf{Equation 2}$$

The magnetic force (F_{mag}) is balanced by the fluid drag which can be approximated using Stokes drag equation because of the low Reynolds number associated with the motion. The equation for Stokes drag equation is solved by ignoring the inertial terms in the Navier-Stokes equation in the case where Reynolds number is <<1. Reynolds number is expressed in **Equation 3**.

$$Re = \frac{inertial\ forces}{viscous\ forces} = \frac{vL}{\nu} \qquad \textbf{Equation 3}$$

The Re of a particle moving under the influence of our magnetic ratcheting platform in a fluid is <<1 as v is in the range of ~10^{-6} m s^{-1} and L, the dimension of the bacterium is in the range of ~10^{-6} m while ν of water at 25 ^{o}C is ~$8.90*10^{-4}$ m^2s^{-1}. We note that the bacterium is cylindrical in shape and not spherical but the Stokes' drag around a non-spherical object can be modeled with a shape factor determined experimentally by Johnson et al.[316] For the case of the cylindrically-shaped bacterium, the shape factor is 0.75 found by substituting values into the equations outlined in ref [257].

Thus **Equation 4** can be used to model the Stokes drag particles experience.

$$F_{drag} = 6\pi\nu r_p \bar{u}_p \qquad \textbf{Equation 4}$$

By balancing **Equation 2** and **4**, the particle speed ($\bar{u}_p$) can be solved as shown in **Equation 5**.

$$\bar{u}_p = \frac{V_p \Delta\chi_p}{u_0} F_{den} * \frac{1}{6\pi\nu r_p} * \sin(\frac{2x}{P} - 2\omega_{ext} t) \quad \textbf{Equation 5}$$

Next, a substitution where $\Omega = \frac{x}{P} - \omega_{ext} t$ is performed where Ω represents the phase lag of the particle motion within the traveling wave of the magnetic ratcheting field. The partial derivative of Ω is shown in **Equation 6** by knowing that during magnetic ratcheting, ω_{ext} is kept constant and using the substitution $\frac{\partial x}{\partial t} = \bar{u}_p$.

$$\frac{\partial \Omega}{\partial t} = \frac{\partial x}{\partial t}\frac{1}{P} - \frac{\partial \omega_{ext}}{\partial t} * t - \omega_{ext}$$

$$= \frac{\bar{u}_p}{P} - \omega_{ext}$$

$$= \omega_{critical} * \sin(2\Omega) - \omega_{ext} \qquad \textbf{Equation 6}$$

The $\omega_{critical}$ can thus be numerically represented in **Equation 7**. This equation describes the linear transport of particles when $\omega_{ext} \leq \omega_{critical}$. However, when $\omega_{ext} > \omega_{critical}$, the particle speed decays with increasing ω_{ext} until it fails to traverse the array of magnetic permalloys and are trapped at the pillar edge.

$$\omega_{critical} = \frac{V_p \Delta\chi_p F_{den}}{u_0 6\pi v r_p P}$$ **Equation 7**

To determine $\omega_{critical}$, we first tracked the ratcheting trajectories of 1 μm magnetic micro-particles across horizontal pitches with 10 μm increments and calculated F_{mag}based on the **Equation 4** force equilibrium with Stokes drag force (**Appendix C Fig. 3**). 1 μm particles (17% iron oxide content) were used as (1) smaller particles were too small for accurate tracking in real-time and (2) , the values of the magnetic volume (v_p) of the 1 μm particles and MNPs produced by AMB-1 are close (**Table 2**).

Table 2 Calculation for magnetic volume

1 μm particle (17% iron oxide)	**AMB-1**
$v_p = \frac{4}{3}\pi(0.5^3) * 10^{-18} * 0.17$ $= 0.089\ \mu m^3$	Model the MNPs chain as a rigid rod[317] As seen from **Fig. 1D**, the average radius and length of AMB-1 is ~ 0.5 μm and 3 μm respectively. $v_{p,bacterium} = \pi(0.5^2) * 10^{-12} * 3 * 10^{-6}$ $= 2.36\ \mu m^3$ The % vol of magnetite MNPs in AMB-1 can be calculated below by knowing that the average radius of MNPs is 25 nm modelled after spheres and we are only keen to isolate AMB-1 mutants with ≥ 20 MNPs/bacterium. $\%\ vol_{MNPs} = \frac{\frac{4}{3}*\pi*(25)^3*10^{-27}*20}{\pi*(0.5)^2*10^{-12}*3*10^{-6}} = 0.056$ Hence $v_{p,MNPs} = 2.36 * 0.056$ $= 0.13\ \mu m^3$

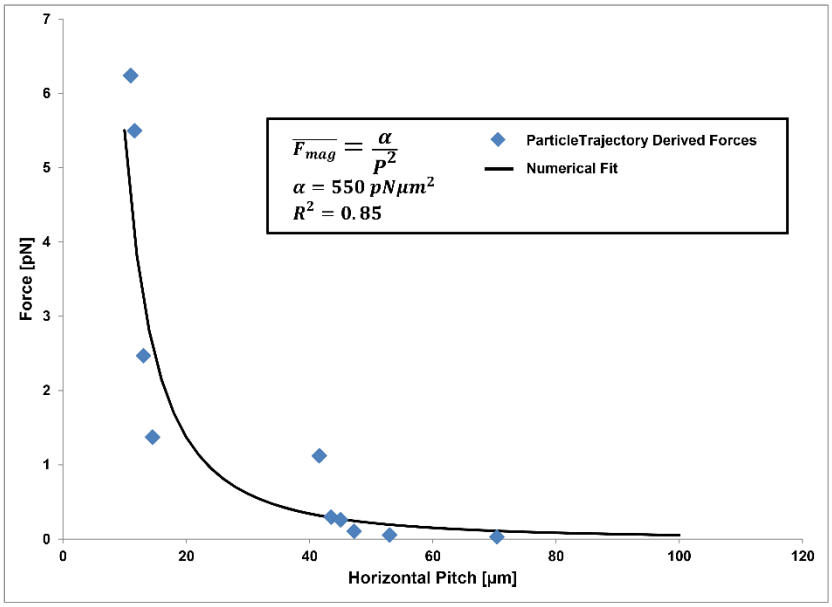

Fig. 3 Plot of F_{mag} against P. A power law best fit with $R^2 = 0.85$ gives the relationship $F_{mag=\frac{\alpha}{P^2}}$ where $\alpha = 550*10^{-24}$ N m^{-2}.

$$F_{mag} = \frac{\alpha}{P^2} \qquad \textbf{Equation 8}$$

Equating the magnitude on **Equation 2** and **8**, we can obtain an expression for F_{den}.

$$F_{den} = \frac{\alpha u_0}{P^2 v \chi_p} \qquad \textbf{Equation 9}$$

Substituting Equation 9 into Equation 7, we can derive an expression for $\omega_{critical}$ and use it to approximate and narrow the range of ratcheting frequency ω_{ext} we should use during the selection phase of directed evolution.

$$\omega_{critical} = \frac{\alpha}{6\pi v r_p P^3} \qquad \textbf{Equation 10}$$

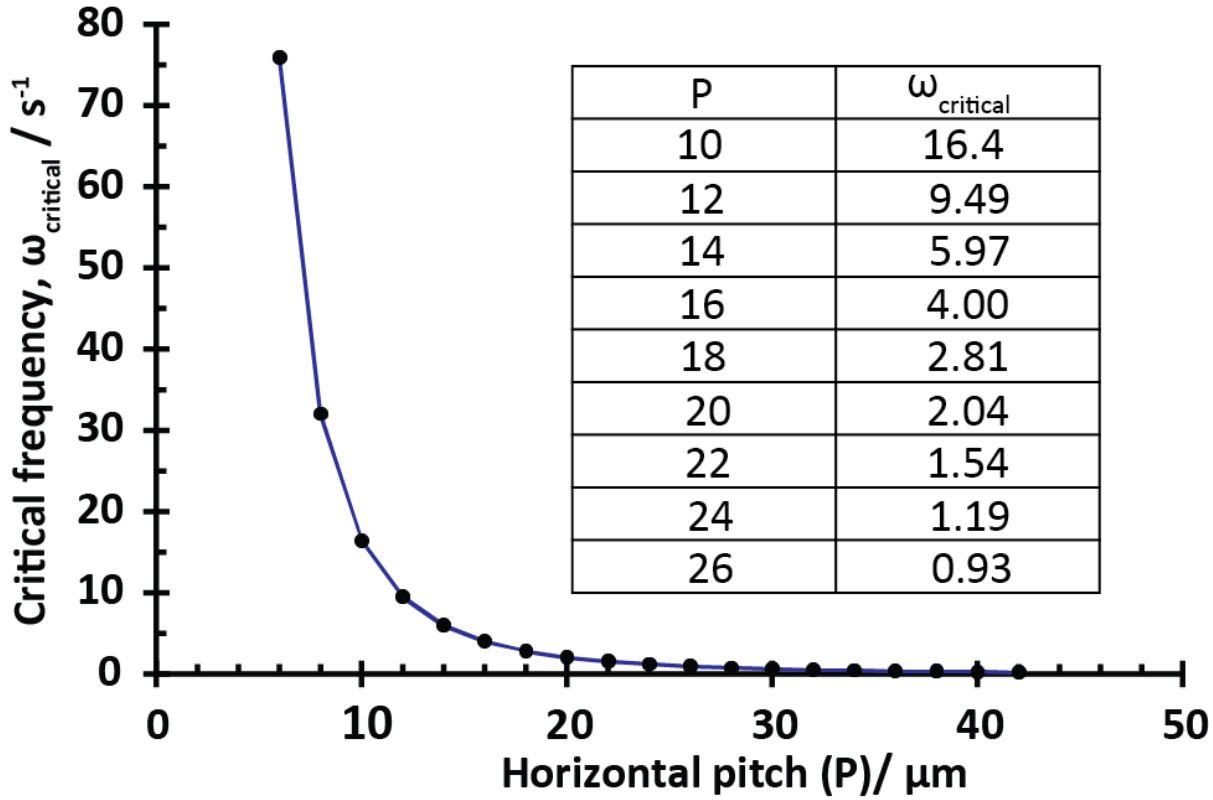

P	$\omega_{critical}$
10	16.4
12	9.49
14	5.97
16	4.00
18	2.81
20	2.04
22	1.54
24	1.19
26	0.93

Fig. 4 Plot of critical frequency against horizontal pitch for 1 µm magnetic micro-particle with 17% iron oxide content. Particles are transported horizontally across the array when $\omega_{ext} \leq \omega_{critical}$. In a population of AMB-1 mutants, some bacteria have larger than average number of MNPs/ bacterium. Let us imagine a situation where the average number of MNPs/ bacterium equates to one 1 µm particle. Hence, at P = 20 µm, the critical frequency is 2 Hz and if we set the external ratcheting frequency to be 5 Hz, only bacteria with greater magnetic content than one 1 µm particle will be transported and trapped at their respective pitch where the magnetic force balanced with Stokes drag force does not yield sufficient velocity to traverse to the next element in the array over the cycle time.

Table 3 Ratcheting parameters for each selection cycle

Ratcheting cycle	**Ratcheting frequency and duration**
1st	5 Hz for 30 min
2nd	5 Hz for 30 min
3rd	5 Hz for 25 min
4th	5 Hz for 25 min
5th	5 Hz for 20 min

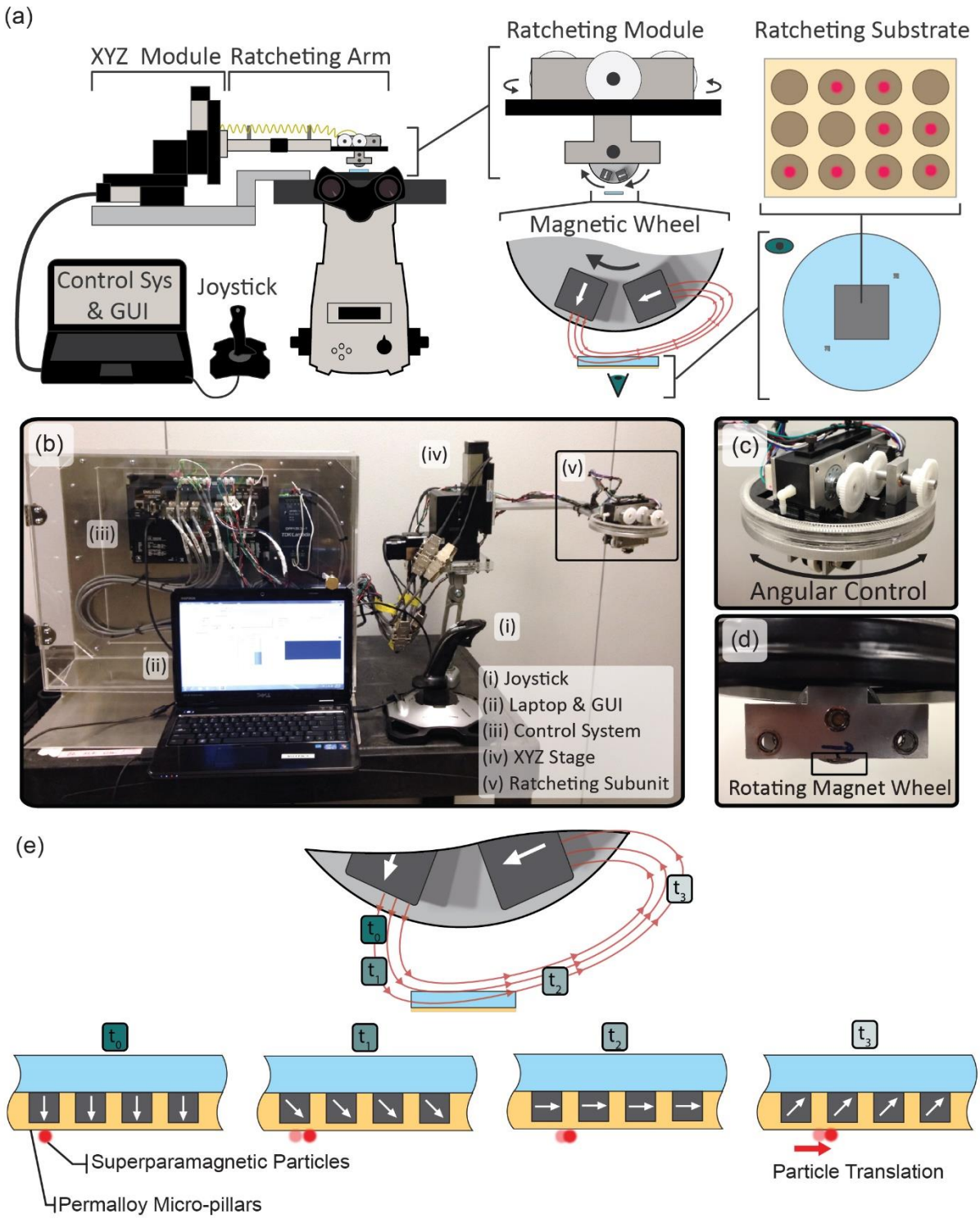

Fig. 5 Schematic and real-life image of magnetic ratcheting platform. (**a**) Schematic and (**b-d**) real-life image of platform. The joystick allows control of the ratcheting arm. (**e**) A continuous cycling magnetic field is generated to create energy potential wells to trap superparamagnetic particles or AMB-1 and to negate the effects of flagellar motion.

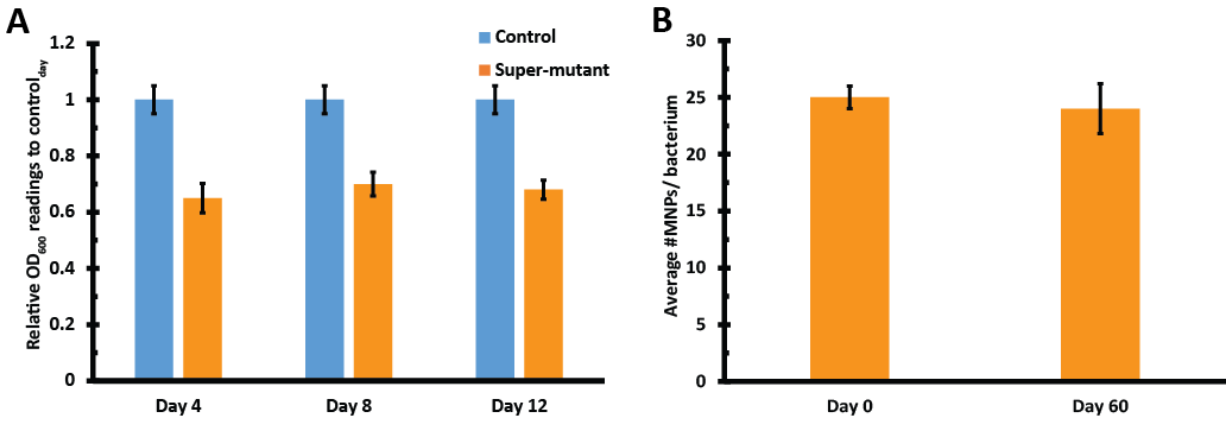

Fig. 6 Relative optical densities of original and mutated AMB-1 and average number of MNPs/over-producers after 60 days of culture. (**A**) After the 5th cycle of mutation-selection, the collected AMB-1 over-producers showed about 30% slower growth, due to the non-targeted effects of random chemical mutagenesis. Hence we hypothesize that by combining targeted genetic manipulations with our magnetic ratcheting system, we should be able to generate over-producers that are desirable both in terms of metabolic rates and number of MNPs/ bacterium. (**B**) The AMB-1 over-producers maintained the high magnetosome producing phenotypes after 60 days of culture, showing that the effects of the selection pressure were maintained over tens of cell division cycles.

Appendix D

Supporting information for Chapter 5

Table 1 Comparisons of different methods to quantify magnetic contents of MTB

	C-mag[242]	**Color inspection**[222]	**Electron microscope**[318]	**Optical magnetic imaging**[319]	**Magnetic ratcheting**[229]	**Magnetic microfluidic**[320]
Time needed	Fast (~5 min)	Slow (~2 weeks)	Slow (~2-3 hr)	Fast (~s)	Fast (~1 hr)	Fast (mins)
Subjective	Yes, does not work for polymorphic MTB	Yes	Yes	No	No	No
Automated	No	No	No	Yes	No	Can be
Quantitative	No	No	Semi	Yes	Yes	Yes
Potential to re-culture after measurement	Yes	Yes	No	Yes	Yes	Yes
Potential for single cell selection	No	Yes	No	No	Yes	Yes
Potential for continuous flow	N.A.	N.A.	N.A.	N.A.	No	Yes
Potential for integration with bioreactor	N.A.	N.A.	N.A.	N.A.	No	Yes

There are also a few other techniques described in literature. They are very recent developments and usually make use of imaging platforms. The techniques are correlative fluorescence and fluid cell scanning transmission electron microscopy[321] and confocal Raman micro-spectrometry.[322]

Table 2 Magnetic volume (V_p) calculations

1 µm particle (17% iron oxide)	**AMB-1**
$v_p = \frac{4}{3}\pi(0.5^3) * 10^{-18} * 0.17$ $= 0.089$ µm^3	Model the MNPs chain as a rigid rod[317] The average radius and length of AMB-1 is ~ 0.5 µm and 3 µm respectively. $v_{p,bacterium} = \pi(0.5^2) * 10^{-12} * 3 * 10^{-6}$ $= 2.36$ µm^3 The % vol of magnetite MNPs in AMB-1 can be calculated below by knowing that the average radius of MNPs is 25 nm modelled after spheres and we are only keen to isolate AMB-1 mutants with ≥ 20 magnetosomess/bacterium. $\%\ vol_{MNPs} = \frac{\frac{4}{3}*\pi*(25)^3*10^{-27}*20}{\pi*(0.5)^2*10^{-12}*3*10^{-6}} = 0.056$ Hence $v_{p,magnetosomes} = 2.36 * 0.056$ $= 0.13\ \mu m^3$

From the calculations, we can see that the magnetic volumes of a 1 µm bead and an AMB-1 bacterium with 20 magnetosomes are comparable. Therefore, we can make use of 1 µm magnetic bead to characterize the possible behaviors of AMB-1 in the microchannel.

Table 3 Calculation of treatment time

Volume of MTB suspension in syringe = 1.0 mL
Volume of tubing = 0.1 mL
Volume of microchannel = length x width x height = 2 x 10^{-2} x 23 2 x 10^{-6} x 500 x 10^{-6} = 0.00023 mL
Flow rate = 25 μL/min = 0.025 mL/min
Maximum time for MTB treatment = (1.0+0.1+0.00023)/0.025 = 44 min

The main volume that affects the length of time for MTB treatment at 10 ^{o}C at pH 8.5 is the volume in the syringe. For sensitive MTB strains, the processed volume can be reduced or can be processed in batches accordingly. It is useful to note that as the combined flow rate is still slow *i.e.* at 25 μL/min, using a syringe with smaller diameter would help to make the flow more stable which is affected by how fast the screw moves in a syringe pump.

Table 4 Comparisons between AMB-1 and MSR-1

Property	**AMB-1**	**MSR-1**
Shape	Spirillum	Spirillum
Size (Length x Width)/ μm	3 x 0.4-0.6	1-20 x 0.7 (Polymorphic)
MNP shape	Cubo-octahedral	Cubo-octahedral
MNP size/ nm	35-50	35-50
#MNPs/cell	~11	~23
Isolation condition	Media inlet: 15 μL/min MTB inlet: 10 μL/min 373 mT	Media inlet: 15 μL/min MTB inlet: 10 μL/min 150 mT

Table 5 Evaluating the change in Stoke's drag and magnetic forces as a function of cell size

	Ordinary MSR-1 Average radius and length of MSR-1 is ~ 0.5 µm and 3 µm respectively.	**MSR-1 with twice the size (and assumed with twice the number of magnetosomes)** Average radius and length of MSR-1 is ~ 0.5 µm and 6 µm respectively.	**Results**
Using equation 2	$F_{drag} = 6\pi v r_p \bar{u}_p$	$F_{drag} = 12\pi v r_p \bar{u}_p$	100% increase in Stokes' drag
Using equations in Table S3	$v_{p,magnetosomes} = 0.13\ \mu m^3$	$v_{p,magnetosomes} = 0.13\ \mu m^3$	Same magnetic volume because when MSR-1 divides, only the length but not the radius doubles

Therefore, longer MSR-1 (stationary phase) experience greater Stokes' drag and are expected to exit through the waste outlet while shorter MSR-1 (log phase) are expected to exit through the selection outlet.

Experimental data	
Magnetic field strength at 0.9 cm (~distance from magnet to microchannel) from magnet surface	$y = 270(0.9)^{-3.076}$ $= 373$ mT
Theoretical estimate	
$B_{r,max}$ (manufacturer)	14800 Gauss
Dimensions (manufacturer)	0.01 x 0.01 x 0.01 m^3
Calculated dipole moment for 1 magnet	$(\frac{14800}{10^4} * 0.01^3)/(4\pi * 10^{-7})$ $= 1.178$ Am^2
Calculated dipole moment for 2 magnets	1.178 * 2 $= 2.34$ Am^2
Using the conversion: 10 $mA.m^2 = 1$ $nT.m^3$	
Distance from magnet to microchannel) from magnet surface to get 373 mT	$((\frac{2.34}{10} * 10^3 * 10^{-6})/373)^{1/3}$ $= 0.73$ cm

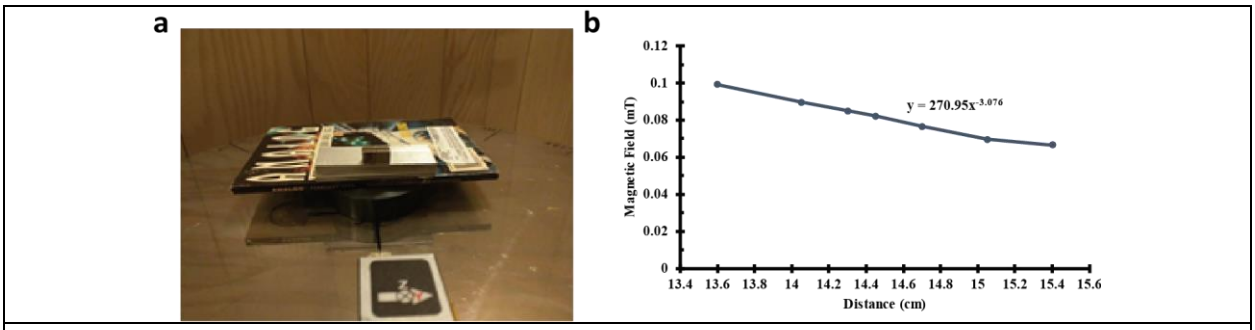

Fig. 1 Magnetic field decay measured with a Hall magnetometer and theoretical estimate with manufacturer's information. (**a**) Measurement set-up. (**b**) Experimentally determined decay of magnetic field at different distances away from the Hall magnetometer.

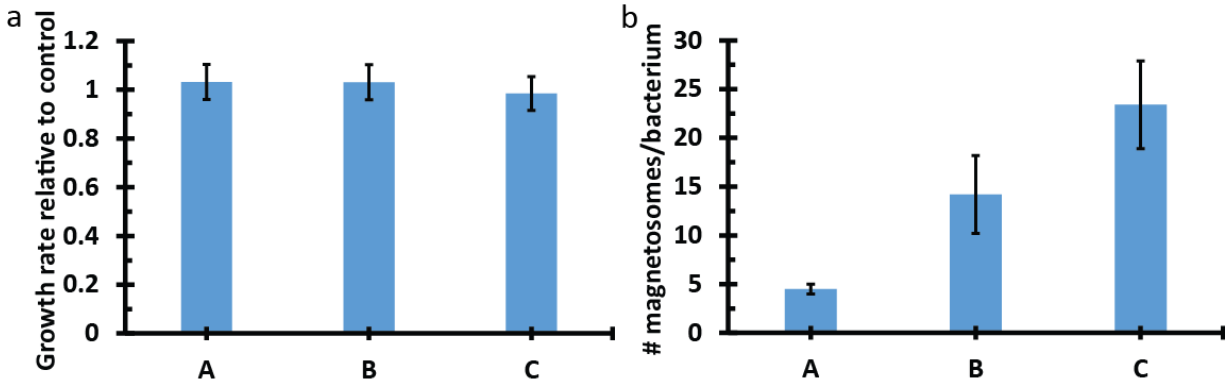

Fig. 2 Optical densities and number of magnetosome per cell of different AMB-1 mutants cultured for 3 days in normal media (~12-18 cell cycles) after treatment with 10 ^{o}C media at pH 8.5 for 1 hr. Treatment did not significantly affect the (**a**) optical densities compared to own control group and (**b**) number of magnetosomes per cell of different groups of AMB-1. A: AMB-1 mutants with mutants with 0 $\pm$ 0.5 magnetosomes/bacterium. B: AMB-1 mutants with mutants with 11.2 $\pm$ 3.7 magnetosomes/bacterium. C: AMB-1 mutants with mutants with 25.0 $\pm$ 3.5 number of magnetosomes/bacterium.

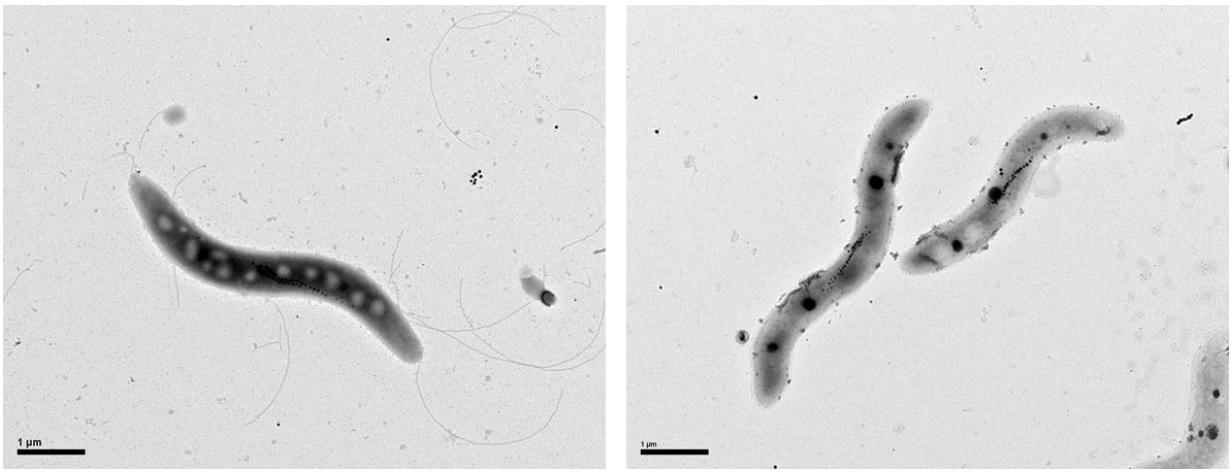

Fig. 3 TEM images of MSR-1. (**a**) MSR-1 wild type with flagella. MSR-1 also has ~twice the number of magnetosomes than AMB-1 (**b**) MSR-1 Δ*flaA* without flagellum

References

(1) McBeath, R.; Pirone, D. M.; Nelson, C. M.; Bhadriraju, K.; Chen, C. S. Cell Shape, Cytoskeletal Tension, and RhoA Regulate Stem Cell Lineage Commitment. *Dev. Cell* **2004**, *6*, 483–495.

(2) Wirtz, D.; Konstantopoulos, K.; Searson, P. C. The Physics of Cancer: The Role of Physical Interactions and Mechanical Forces in Metastasis. *Nat Rev Cancer* **2011**, *11*, 512–522.

(3) Warkiani, M. E.; Tay, A. K. P.; Khoo, B. L.; Xiaofeng, X.; Han, J.; Lim, C. T. Malaria Detection Using Inertial Microfluidics. *Lab Chip* **2015**, *15*, 1101–1109.

(4) Tyler, W. J. The Mechanobiology of Brain Function. *Nat. Rev. Neurosci.* **2012**, *13*, 867–878.

(5) Brouzés, E.; Farge, E. Interplay of Mechanical Deformation and Patterned Gene Expression in Developing Embryos. *Curr. Opin. Genet. Dev.* **2004**, *14*, 367–374.

(6) Siechen, S.; Yang, S.; Chiba, A.; Saif, T. Mechanical Tension Contributes to Clustering of Neurotransmitter Vesicles at Presynaptic Terminals. *Proc. Natl. Acad. Sci. U. S. A.* **2009**, *106*, 12611–12616.

(7) Lamoureux, P.; Ruthel, G.; Buxbaum, R. E.; Heidemann, S. R. Mechanical Tension Can Specify Axonal Fate in Hippocampal Neurons. *J. Cell Biol.* **2002**, *159*, 499–508.

(8) Anava, S.; Greenbaum, A.; Jacob, E. Ben; Hanein, Y.; Ayali, A. The Regulative Role of Neurite Mechanical Tension in Network Development. *Biophys. J.* **2009**, *96*, 1661–1670.

(9) Zhang, Y.; Zhou, Y.; Yu, C.; Lin, L.; Li, C.; Jiang, T. Reduced Cortical Folding in Mental Retardation. *AJNR. Am. J. Neuroradiol.* **2010**, *31*, 1063–1067.

(10) Sharp, D. J.; Scott, G.; Leech, R. Network Dysfunction after Traumatic Brain Injury. *Nat.*

Rev. Neurol. **2014**, *10*, 156–166.

(11) Xiong, Y.; Aih, C. L.; Suter, D. M.; Lee, G. U. Topography and Nanomechanics of Live Neuronal Growth Cones Analyzed by Atomic Force Microscopy. *Biophys. J.* **2009**, *96*, 5060–5072.

(12) Sappington, R. M.; Sidorova, T.; Long, D. J.; Calkins, D. J. TRPV1: Contribution to Retinal Ganglion Cell Apoptosis and Increased Intracellular Ca2+ with Exposure to Hydrostatic Pressure. *Investig. Ophthalmol. Vis. Sci.* **2009**, *50*, 717–728.

(13) Kilinc, D.; Blasiak, A.; Lee, G. Microtechnologies for Studying the Role of Mechanics in Axon Growth and Guidance. *Front. Cell. Neurosci.* **2015**.

(14) Berdondini, L.; Imfeld, K.; Maccione, A.; Tedesco, M.; Neukom, S.; Koudelka-Hep, M.; Martinoia, S. Active Pixel Sensor Array for High Spatio-Temporal Resolution Electrophysiological Recordings from Single Cell to Large Scale Neuronal Networks. *Lab Chip* **2009**, *9*, 2644–2651.

(15) Huang, Y.; Williams, J. C.; Johnson, S. M. Brain Slice on a Chip: Opportunities and Challenges of Applying Microfluidic Technology to Intact Tissues. *Lab Chip* **2012**, *12*, 2103.

(16) Kurth, F.; Eyer, K.; Franco-Obregón, A.; Dittrich, P. S. A New Mechanobiological Era: Microfluidic Pathways to Apply and Sense Forces at the Cellular Level. *Curr. Opin. Chem. Biol.* **2012**, *16*, 400–408.

(17) Rambani, K.; Vukasinovic, J.; Glezer, A.; Potter, S. M. Culturing Thick Brain Slices: An Interstitial 3D Microperfusion System for Enhanced Viability. *J. Neurosci. Methods* **2009**, *180*, 243–254.

(18) Marbán, E. Cardiac Channelopathies. *Nature* **2002**, *415*, 213–218.

(19) Delmas, P.; Hao, J.; Rodat-Despoix, L. Molecular Mechanisms of Mechanotransduction in Mammalian Sensory Neurons. *Nat. Rev. Neurosci.* **2011**, *12*, 139–153.

(20) Galkin, V. E.; Orlova, A.; Egelman, E. H. Actin Filaments as Tension Sensors. *Curr. Biol.* **2012**, *22*, R96–R101.

(21) Smith, S. J. Neuronal Cytomechanics: The Actin-Based Motility of Growth Cones. *Science* **1988**, *242*, 708–715.

(22) Matus, a. Actin-Based Plasticity in Dendritic Spines. *Science* **2000**, *290*, 754–758.

(23) Hu, X.; Viesselmann, C.; Nam, S.; Merriam, E.; Dent, E. W. Activity-Dependent Dynamic Microtubule Invasion of Dendritic Spines. *J. Neurosci.* **2008**, *28*, 13094–13105.

(24) Brown, H. G.; Hoh, J. H. Entropic Exclusion by Neurofilament Sidearms: A Mechanism for Maintaining Interfilament Spacing. *Biochemistry* **1997**, *36*, 15035–15040.

(25) Perrot, R.; Eyer, J. Neuronal Intermediate Filaments and Neurodegenerative Disorders. *Brain Res. Bull.* **2009**, *80*, 282–295.

(26) Dityatev, A.; Schachner, M.; Sonderegger, P. The Dual Role of the Extracellular Matrix in Synaptic Plasticity and Homeostasis. *Nat. Rev. Neurosci.* **2010**, *11*, 735–746.

(27) Tsunozaki, M.; Bautista, D. M. Mammalian Somatosensory Mechanotransduction. *Curr Opin Neurobiol* **2009**, *19*, 362–369.

(28) Hu, J.; Lewin, G. R. Mechanosensitive Currents in the Neurites of Cultured Mouse Sensory Neurones. *J. Physiol.* **2006**, *577*, 28.

(29) Hamill, O. P.; McBride, D. W. Rapid Adaptation of Single Mechanosensitive Channels in Xenopus Oocytes. *Proc. Natl. Acad. Sci. U. S. A.* **1992**, *89*, 7462–7466.

(30) McCarter, G. C.; Reichling, D. B.; Levine, J. D. Mechanical Transduction by Rat Dorsal Root Ganglion Neurons in Vitro. *Neurosci. Lett.* **1999**, *273*, 179–182.

(31) Sachs, F. Stretch-Activated Ion Channels: What Are They? *Physiology (Bethesda).* **2010**, *25*, 50–56.

(32) Liu, M.; Song, W.; Li, P.; Huang, Y.; Gong, X.; Zhou, G.; Jia, X.; Zheng, L.; Fan, Y. Galanin Protects against Nerve Injury after Shear Stress in Primary Cultured Rat Cortical Neurons. *PLoS One* **2013**, *8*.

(33) Bhattacharya, M. R. C.; Bautista, D. M.; Wu, K.; Haeberle, H.; Lumpkin, E. a; Julius, D. Radial Stretch Reveals Distinct Populations of Mechanosensitive Mammalian Somatosensory Neurons. *Proc. Natl. Acad. Sci. U. S. A.* **2008**, *105*, 20015–20020.

(34) Dertinger, S. K. W.; Jiang, X.; Li, Z.; Murthy, V. N.; Whitesides, G. M. Gradients of Substrate-Bound Laminin Orient Axonal Specification of Neurons. *Proc. Natl. Acad. Sci. U. S. A.* **2002**, *99*, 12542–12547.

(35) Millet, L. J.; Stewart, M. E.; Nuzzo, R. G.; Gillette, M. U. Guiding Neuron Development with Planar Surface Gradients of Substrate Cues Deposited Using Microfluidic Devices. *Lab Chip* **2010**, *10*, 1525–1535.

(36) Sundararaghavan, H. G.; Monteiro, G. a.; Firestein, B. L.; Shreiber, D. I. Neurite Growth in 3D Collagen Gels with Gradients of Mechanical Properties. *Biotechnol. Bioeng.* **2009**, *102*, 632–643.

(37) Rajnicek, A.; Britland, S.; McCaig, C. Contact Guidance of CNS Neurites on Grooved Quartz: Influence of Groove Dimensions, Neuronal Age and Cell Type. *J. Cell Sci.* **1997**, *110 (Pt 2*, 2905–2913.

(38) Kaehr, B.; Allen, R.; Javier, D. J.; Currie, J.; Shear, J. B. Guiding Neuronal Development with in Situ Microfabrication. *Proc. Natl. Acad. Sci. U. S. A.* **2004**, *101*, 16104–16108.

(39) Parpura, V.; Haydon, P. G.; Henderson, E. Three-Dimensional Imaging of Living Neurons

and Glia with the Atomic Force Microscope. *J. Cell Sci.* **1993**, *104 (Pt 2*, 427–432.

(40) Gopal, A.; Luo, Z.; Lee, J. Y.; Kumar, K.; Li, B.; Hoshino, K.; Schmidt, C.; Ho, P. S.; Zhang, X. Nano-Opto-Mechanical Characterization of Neuron Membrane Mechanics under Cellular Growth and Differentiation. *Biomed. Microdevices* **2008**, *10*, 611–622.

(41) Taylor, A. M.; Blurton-Jones, M.; Rhee, S. W.; Cribbs, D. H.; Cotman, C. W.; Jeon, N. L. A Microfluidic Culture Platform for CNS Axonal Injury, Regeneration and Transport. *Nat. Methods* **2005**, *2*, 599–605.

(42) Taylor, A. M.; Rhee, S. W.; Tu, C. H.; Cribbs, D. H.; Cotman, C. W.; Jeon, N. L. Microfluidic Multicompartment Device for Neuroscience Research. *Langmuir* **2003**, *19*, 1551–1556.

(43) Dotti, C. G.; Sullivan, C. a; Banker, G. a. The Establishment of Polarity by Hippocampal Neurons in Culture. *The Journal of neuroscience : the official journal of the Society for Neuroscience*, 1988, *8*, 1454–1468.

(44) Hosmane, S.; Fournier, A.; Wright, R.; Rajbhandari, L.; Siddique, R.; Yang, I. H.; Ramesh, K. T.; Venkatesan, A.; Thakor, N. Valve-Based Microfluidic Compression Platform: Single Axon Injury and Regrowth. *Lab Chip* **2011**, *11*, 3888.

(45) Hellman, A. N.; Vahidi, B.; Kim, H. J.; Mismar, W.; Steward, O.; Jeon, N. L.; Venugopalan, V. Examination of Axonal Injury and Regeneration in Micropatterned Neuronal Culture Using Pulsed Laser Microbeam Dissection. *Lab Chip* **2010**, *10*, 2083–2092.

(46) Yang, Y.; Gozen, O.; Watkins, A.; Lorenzini, I.; Lepore, A.; Gao, Y.; Vidensky, S.; Brennan, J.; Poulsen, D.; Won Park, J.; *et al.* Presynaptic Regulation of Astroglial Excitatory Neurotransmitter Transporter GLT1. *Neuron* **2009**, *61*, 880–894.

(47) Teh, S.-Y.; Lin, R.; Hung, L.-H.; Lee, A. P. Droplet Microfluidics. *Lab Chip* **2008**, *8*, 198–220.

(48) Campàs, O.; Mammoto, T.; Hasso, S.; Sperling, R. a; O'Connell, D.; Bischof, A. G.; Maas, R.; Weitz, D. a; Mahadevan, L.; Ingber, D. E. Quantifying Cell-Generated Mechanical Forces within Living Embryonic Tissues. *Nat. Methods* **2014**, *11*, 183–189.

(49) Corbin, E. A.; Kong, F.; Lim, C. T.; King, W. P.; Bashir, R. Biophysical Properties of Human Breast Cancer Cells Measured Using Silicon MEMS Resonators and Atomic Force Microscopy. *Lab Chip* **2015**, *15*, 839–847.

(50) Corbin, E. A.; Millet, L. J.; Keller, K. R.; King, W. P.; Bashir, R. Measuring Physical Properties of Neuronal and Glial Cells with Resonant Microsensors. *Anal. Chem.* **2014**, *86*, 4864–4872.

(51) Park, K.; Mehrnezhad, A.; Corbin, E. A.; Bashir, R. Optomechanical Measurement of the Stiffness of Single Adherent Cells. *Lab Chip* **2015**, 3460–3464.

(52) Teixeira, A. I.; Ilkhanizadeh, S.; Wigenius, J. A.; Duckworth, J. K.; Inganäs, O.; Hermanson, O. The Promotion of Neuronal Maturation on Soft Substrates. *Biomaterials* **2009**, *30*, 4567–4572.

(53) Tseng, P.; Judy, J. W.; Di Carlo, D. Magnetic Nanoparticle–mediated Massively Parallel Mechanical Modulation of Single-Cell Behavior. *Nature Methods*, 2012.

(54) Kunze, A.; Tseng, P.; Godzich, C.; Murray, C.; Caputo, A.; Schweizer, F. E.; Di Carlo, D. Engineering Cortical Neuron Polarity with Nanomagnets on a Chip. *ACS Nano* **2015**.

(55) T., M. M. D. . B. R. . D. A. M. and F. Calcium Signaling | Springer http://www.springer.com/us/book/9789400728875 (accessed May 10, 2015).

(56) Mattson, M. P.; LaFerla, F. M.; Chan, S. L.; Leissring, M. A.; Shepel, P. N.; Geiger, J. D.

Calcium Signaling in the ER: Its Role in Neuronal Plasticity and Neurodegenerative Disorders. *Trends Neurosci.* **2000**, *23*, 222–229.

(57) Tsai, H.-C.; Zhang, F.; Adamantidis, A.; Stuber, G. D.; Bonci, A.; de Lecea, L.; Deisseroth, K. Phasic Firing in Dopaminergic Neurons Is Sufficient for Behavioral Conditioning. *Science* **2009**, *324*, 1080–1084.

(58) Tay, A.; Kunze, A.; Murray, C.; Di Carlo, D. Induction of Calcium Influx in Cortical Neural Networks by Nanomagnetic Forces. *ACS Nano* **2016**.

(59) Ciofani, G.; Danti, S.; D'Alessandro, D.; Ricotti, L.; Moscato, S.; Bertoni, G.; Falqui, A.; Berrettini, S.; Petrini, M.; Mattoli, V.; *et al.* Enhancement of Neurite Outgrowth in Neuronal-like Cells Following Boron Nitride Nanotube-Mediated Stimulation. *ACS Nano* **2010**, *4*, 6267–6277.

(60) Marino, A.; Arai, S.; Hou, Y.; Sinibaldi, E.; Pellegrino, M.; Chang, Y.-T.; Mazzolai, B.; Mattoli, V.; Suzuki, M.; Ciofani, G. Piezoelectric Nanoparticle-Assisted Wireless Neuronal Stimulation. *ACS Nano* **2015**.

(61) Julius, D. Molecular Mechanisms of Nociception . *Nature* **2001**, *413*, 203–210.

(62) Gillespie, P. G.; Walker, R. G. Molecular Basis of Mechanosensory Transduction. *Nature* **2001**, *413*, 194–202.

(63) Levina, N.; Tötemeyer, S.; Stokes, N. R.; Louis, P.; Jones, M. a; Booth, I. R. Protection of Escherichia Coli Cells against Extreme Turgor by Activation of MscS and MscL Mechanosensitive Channels: Identification of Genes Required for MscS Activity. *EMBO J.* **1999**, *18*, 1730–1737.

(64) Chalfie, M. Neurosensory Mechanotransduction. *Nat. Rev. Mol. Cell Biol.* **2009**, *10*, 44–52.

(65) Zhang, Z.; Kindrat, A. N.; Sharif-Naeini, R.; Bourque, C. W. Actin Filaments Mediate Mechanical Gating during Osmosensory Transduction in Rat Supraoptic Nucleus Neurons. *J. Neurosci.* **2007**, *27*, 4008–4013.

(66) Viana, F.; de la Peña, E.; Pecson, B.; Schmidt, R. F.; Belmonte, C. Swelling-Activated Calcium Signalling in Cultured Mouse Primary Sensory Neurons. *Eur. J. Neurosci.* **2001**, *13*, 722–734.

(67) Vilceanu, D.; Stucky, C. L. TRPA1 Mediates Mechanical Currents in the Plasma Membrane of Mouse Sensory Neurons. *PLoS One* **2010**, *5*, 1–10.

(68) Pavesi, A.; Adriani, G.; Rasponi, M.; Zervantonakis, I. K.; Fiore, G. B.; Kamm, R. D. Controlled Electromechanical Cell Stimulation on-a-Chip. *Sci. Rep.* **2015**, *5*, 11800.

(69) Nguyen, M.-D.; Tinney, J. P.; Ye, F.; Elnakib, A. A.; Yuan, F.; El-Baz, A.; Sethu, P.; Keller, B. B.; Giridharan, G. A. Effects of Physiologic Mechanical Stimulation on Embryonic Chick Cardiomyocytes Using a Microfluidic Cardiac Cell Culture Model. *Anal. Chem.* **2015**, *87*, 2107–2113.

(70) Jacques-Fricke, B. T.; Seow, Y.; Gottlieb, P. a; Sachs, F.; Gomez, T. M. Ca2+ Influx through Mechanosensitive Channels Inhibits Neurite Outgrowth in Opposition to Other Influx Pathways and Release from Intracellular Stores. *J. Neurosci.* **2006**, *26*, 5656–5664.

(71) Honoré, E.; Patel, A. J.; Chemin, J.; Suchyna, T.; Sachs, F. Desensitization of Mechano-Gated K2P Channels. *Proc. Natl. Acad. Sci. U. S. A.* **2006**, *103*, 6859–6864.

(72) Clement, G. T.; Nomura, H.; Adachi, H.; Kamakura, T. The Feasibility of Non-Contact Ultrasound for Medical Imaging. *Phys. Med. Biol.* **2013**, *58*, 6263–6278.

(73) Kisaalita, W. S.; Evans, M.; Lund, R. B. Size Changes in Differentiating Neuroblastoma Cells. *Vitr. Cell. Dev. Biol. - Anim.* **1997**, *33*, 734–737.

(74) Yuste, R. From the Neuron Doctrine to Neural Networks. *Nat. Rev. Neurosci.* **2015**, *16*, 487–497.

(75) Kaplan, W. D.; Trout, W. E. The Behavior of Four Neurological Mutants of Drosophila. *Genetics* **1969**, *61*, 399–409.

(76) Ketchum, K. A.; Joiner, W. J.; Sellers, A. J.; Kaczmarek, L. K.; Goldstein, S. A. A New Family of Outwardly Rectifying Potassium Channel Proteins with Two Pore Domains in Tandem. *Nature* **1995**, *376*, 690–695.

(77) Noda, M.; Shimizu, S.; Tanabe, T.; Takai, T.; Kayano, T.; Ikeda, T.; Takahashi, H.; Nakayama, H.; Kanaoka, Y.; Minamino, N.; *et al.* Primary Structure of Electrophorus Electricus Sodium Channel Deduced from cDNA Sequence. *Nature* **1984**, *312*, 121–127.

(78) Nowycky, M. C.; Fox, A. P.; Tsien, R. W. Three Types of Neuronal Calcium Channel with Different Calcium Agonist Sensitivity. *Nature* **1985**, *316*, 440–443.

(79) Cosens, D. J.; Manning, a. Abnormal Electroretinogram from a Drosophila Mutant. *Nature* **1969**, *224*, 285–287.

(80) Huang, H.; Delikanli, S.; Zeng, H.; Ferkey, D. M.; Pralle, A. Remote Control of Ion Channels and Neurons through Magnetic-Field Heating of Nanoparticles. *Nat. Nanotechnol.* **2010**, *5*, 602–606.

(81) Chen, R.; Romero, G.; Christiansen, M. G.; Mohr, A.; Anikeeva, P. Wireless Magnetothermal Deep Brain Stimulation. *Science* **2015**, *347*, 1477–1480.

(82) Coste, B.; Mathur, J.; Schmidt, M.; Earley, T. J.; Ranade, S.; Petrus, M. J.; Dubin, A. E.; Patapoutian, A. Piezo1 and Piezo2 Are Essential Components of Distinct Mechanically Activated Cation Channels. *Science* **2010**, *330*, 55–60.

(83) Becq, F. On the Discovery and Development of CFTR Chloride Channel Activators. *Curr.*

Pharm. Des. **2006**, *12*, 471–484.

(84) Augustine, G. J. How Does Calcium Trigger Neurotransmitter Release? *Curr. Opin. Neurobiol.* **2001**, *11*, 320–326.

(85) Hirata, H.; Tatsumi, H.; Sokabe, M. Mechanical Forces Facilitate Actin Polymerization at Focal Adhesions in a Zyxin-Dependent Manner. *J. Cell Sci.* **2008**, *121*, 2795–2804.

(86) Fan, A.; Stebbings, K. A.; Llano, D. A.; Saif, T. Stretch Induced Hyperexcitability of Mice Callosal Pathway. *Front. Cell. Neurosci.* **2015**, *9*, 292.

(87) Kashani, A. H.; Chen, B. M.; Grinnell, A. D. Hypertonic Enhancement of Transmitter Release from Frog Motor Nerve Terminals: Ca2+ Independence and Role of Integrins. *J. Physiol.* **2001**, *530*, 243–252.

(88) Kleiman, R. J.; Reichardt, L. F. Testing the Agrin Hypothesis. *Cell* **1996**, *85*, 461–464.

(89) Tourovskaia, A.; Li, N.; Folch, A. Localized Acetylcholine Receptor Clustering Dynamics in Response to Microfluidic Focal Stimulation with Agrin. *Biophys. J.* **2008**, *95*, 3009–3016.

(90) Vincent, A.; Lang, B.; Kleopa, K. a. Autoimmune Channelopathies and Related Neurological Disorders. *Neuron* **2006**, *52*, 123–138.

(91) Botzolakis, E. J.; Maheshwari, a.; Feng, H. J.; Lagrange, a. H.; Shaver, J. H.; Kassebaum, N. J.; Venkataraman, R.; Baudenbacher, F.; Macdonald, R. L. Achieving Synaptically Relevant Pulses of Neurotransmitter Using PDMS Microfluidics. *J. Neurosci. Methods* **2009**, *177*, 294–302.

(92) Bernstein, J. G.; Garrity, P. A.; Boyden, E. S. Optogenetics and Thermogenetics: Technologies for Controlling the Activity of Targeted Cells within Intact Neural Circuits. *Current Opinion in Neurobiology*, 2012, *22*, 61–71.

(93) Taylor, A. M.; Dieterich, D. C.; Ito, H. T.; Kim, S. a.; Schuman, E. M. Microfluidic Local Perfusion Chambers for the Visualization and Manipulation of Synapses. *Neuron* **2010**, *66*, 57–68.

(94) Taylor, A. M.; Jeon, N. L. Micro-Scale and Microfluidic Devices for Neurobiology. *Curr. Opin. Neurobiol.* **2010**, *20*, 640–647.

(95) Croushore, C. a; Sweedler, J. V. Microfluidic Systems for Studying Neurotransmitters and Neurotransmission. *Lab Chip* **2013**, *13*, 1666–1676.

(96) Nandi, P.; Desai, D. P.; Lunte, S. M. Development of a PDMS-Based Microchip Electrophoresis Device for Continuous Online in Vivo Monitoring of Microdialysis Samples. *Electrophoresis* **2010**, *31*, 1414–1422.

(97) Wang, M.; Roman, G. T.; Perry, M. L.; Kennedy, R. T. Microfluidic Chip for High Efficiency Electrophoretic Analysis of Segmented Flow from a Microdialysis Probe and in Vivo Chemical Monitoring. *Anal. Chem.* **2009**, *81*, 9072–9078.

(98) Lamoureux, P.; Buxbaum, R. E.; Heidemann, S. R. Direct Evidence That Growth Cones Pull. *Nature* **1989**, *340*, 159–162.

(99) Chada, S.; Lamoureux, P.; Buxbaum, R. E.; Heidemann, S. R. Cytomechanics of Neurite Outgrowth from Chick Brain Neurons. *J. Cell Sci.* **1997**, *110 (Pt 1*, 1179–1186.

(100) Fass, J. N.; Odde, D. J. Tensile Force-Dependent Neurite Elicitation via Anti-beta1 Integrin Antibody-Coated Magnetic Beads. *Biophys. J.* **2003**, *85*, 623–636.

(101) Franze, K.; Gerdelmann, J.; Weick, M.; Betz, T.; Pawlizak, S.; Lakadamyali, M.; Bayer, J.; Rillich, K.; Gögler, M.; Lu, Y. B.; *et al.* Neurite Branch Retraction Is Caused by a Threshold-Dependent Mechanical Impact. *Biophys. J.* **2009**, *97*, 1883–1890.

(102) Van Essen, D. C. A Tension-Based Theory of Morphogenesis and Compact Wiring in the

Central Nervous System. *Nature* **1997**, *385*, 313–318.

(103) Rajagopalan, J.; Tofangchi, A.; Saif, T. a. Drosophila Neurons Actively Regulate Axonal Tension in Vivo. *Biophys. J.* **2010**, *99*, 3208–3215.

(104) Lu, W.; Fox, P.; Lakonishok, M.; Davidson, M. W.; Gelfand, V. I. Initial Neurite Outgrowth in Drosophila Neurons Is Driven by Kinesin-Powered Microtubule Sliding. *Curr. Biol.* **2013**, *23*, 1018–1023.

(105) Smith, D. H.; Wolf, J. a; Meaney, D. F. A New Strategy to Produce Sustained Growth of Central Nervous System Axons: Continuous Mechanical Tension. *Tissue Eng.* **2001**, *7*, 131–139.

(106) McDonald, J. W. Repairing the Damaged Spinal Cord. *Sci. Am.* **1999**, *281*, 64–73.

(107) Ahmed, W. W.; Kural, M. H.; Saif, T. a. A Novel Platform for in Situ Investigation of Cells and Tissues under Mechanical Strain. *Acta Biomater.* **2010**, *6*, 2979–2990.

(108) Takayama, Y.; Kotake, N.; Haga, T.; Suzuki, T.; Mabuchi, K. Formation of One-Way-Structured Cultured Neuronal Networks in Microfluidic Devices Combining with Micropatterning Techniques. *J. Biosci. Bioeng.* **2012**, *114*, 92–95.

(109) Park, J. W.; Vahidi, B.; Kim, H. J.; Rhee, S. W.; Jeon, N. L. Quantitative Analysis of CNS Axon Regeneration Using a Microfluidic Neuron Culture Device. *Biochip J.* **2008**, *2*, 44–51.

(110) Siddique, R.; Thakor, N. Investigation of Nerve Injury through Microfluidic Devices. *J. R. Soc. Interface* **2014**, *11*, 20130676.

(111) Nguyen, T. D.; Hogue, I. B.; Cung, K.; Purohit, P. K.; McAlpine, M. C. Tension-Induced Neurite Growth in Microfluidic Channels. *Lab Chip* **2013**, *13*, 3735–3740.

(112) Guo, S. X.; Bourgeois, F.; Chokshi, T.; Durr, N. J.; Hilliard, M. A.; Chronis, N.; Ben-

Yakar, A. Femtosecond Laser Nanoaxotomy Lab-on-Achip for in Vivo Nerve Regeneration Studies. *Nat. Methods* **2008**, *5*, 531–533.

(113) Chokshi, T. V; Ben-Yakar, A.; Chronis, N. CO2 and Compressive Immobilization of C. Elegans on-Chip. *Lab Chip* **2009**, *9*, 151–157.

(114) Kilinc, D.; Blasiak, A.; O'Mahony, J. J.; Lee, G. U. Low Piconewton Towing of CNS Axons against Diffusing and Surface-Bound Repellents Requires the Inhibition of Motor Protein-Associated Pathways. *Sci Rep* **2014**, *4*, 7128.

(115) Soichet, M. S.; Tate, C. C.; Baumann, M. D.; LaPlaca, M. C. Strategies for Regeneration and Repair in the Injured Central Nervous System. In *Indwelling Neural Implants*; 2008; p. Chapter 8.

(116) Gu, L.; Black, B.; Ordonez, S.; Mondal, A.; Jain, A.; Mohanty, S. Microfluidic Control of Axonal Guidance. *Sci. Rep.* **2014**, *4*, 6457.

(117) Luo, L.; O'Leary, D. D. M. Axon Retraction and Degeneration in Development and Disease. *Annu. Rev. Neurosci.* **2005**, *28*, 127–156.

(118) Heidemann, S. R.; Buxbaum, R. E. Mechanical Tension as a Regulator of Axonal Development. *Neurotoxicology* **1994**, *15*, 95–107.

(119) Bayly, P. V.; Taber, L. a.; Kroenke, C. D. Mechanical Forces in Cerebral Cortical Folding: A Review of Measurements and Models. *J. Mech. Behav. Biomed. Mater.* **2014**, *29*, 568–581.

(120) Hilgetag, C. C.; Barbas, H. Developmental Mechanics of the Primate Cerebral Cortex. *Anat. Embryol. (Berl).* **2005**, *210*, 411–417.

(121) Hilgetag, C. C.; Barbas, H. Role of Mechanical Factors in the Morphology of the Primate Cerebral Cortex. *PLoS Comput. Biol.* **2006**, *2*, 146–159.

(122) Manzini, M. C.; Walsh, C. A. What Disorders of Cortical Development Tell Us about the Cortex: One plus One Does Not Always Make Two. *Curr. Opin. Genet. Dev.* **2011**, *21*, 333–339.

(123) Nordahl, C. W.; Dierker, D.; Mostafavi, I.; Schumann, C. M.; Rivera, S. M.; Amaral, D. G.; Essen, D. C. Van. Cortical Folding Abnormalities in Autism Revealed by Surface-Based Morphometry. *J. Neurosci.* **2007**, *27*, 11725–11735.

(124) Hardan, A. Y.; Jou, R. J.; Keshavan, M. S.; Varma, R.; Minshew, N. J. Increased Frontal Cortical Folding in Autism: A Preliminary MRI Study. *Psychiatry Res* **2004**, *131*, 263–268.

(125) Hardan, A. Y.; Muddasani, S.; Vemulapalli, M.; Keshavan, M. S.; Minshew, N. J. An MRI Study of Increased Cortical Thickness in Autism. *Am. J. Psychiatry* **2006**, *163*, 1290–1292.

(126) Tallinen, T.; Chung, J. Y.; Rousseau, F.; Girard, N.; Lefèvre, J.; Mahadevan, L. On the Growth and Form of Cortical Convolutions. *Nat. Phys.* **2016**, *advance on*.

(127) Toro, R.; Perron, M.; Pike, B.; Richer, L.; Veillette, S.; Pausova, Z.; Paus, T. Brain Size and Folding of the Human Cerebral Cortex. *Cereb. Cortex (New York, N.Y. 1991)* **2008**, *18*, 2352–2357.

(128) Germanaud, D.; Lefèvre, J.; Toro, R.; Fischer, C.; Dubois, J.; Hertz-Pannier, L.; Mangin, J. F. Larger Is Twistier: Spectral Analysis of Gyrification (SPANGY) Applied to Adult Brain Size Polymorphism. *Neuroimage* **2012**, *63*, 1257–1272.

(129) Sun, T.; Hevner, R. F. Growth and Folding of the Mammalian Cerebral Cortex: From Molecules to Malformations. *Nat. Rev. Neurosci.* **2014**, *15*, 217–232.

(130) Budday, S.; Raybaud, C.; Kuhl, E. A Mechanical Model Predicts Morphological

Abnormalities in the Developing Human Brain. *Sci. Rep.* **2014**, *4*, 5644.

(131) Tang, Y.; Kim, J.; Lopez-Valdes, H. E.; Brennan, K. C.; Ju, Y. S. Development and Characterization of a Microfluidic Chamber Incorporating Fluid Ports with Active Suction for Localized Chemical Stimulation of Brain Slices. *Lab Chip* **2011**, *11*, 2247–2254.

(132) Wang, J.; Ren, L.; Li, L.; Liu, W.; Zhou, J.; Yu, W.; Tong, D.; Chen, S. Microfluidics: A New Cosset for Neurobiology. *Lab Chip* **2009**, *9*, 644–652.

(133) Ghajar, J. Traumatic Brain Injury. *Lancet* **2000**, *356*, 923–929.

(134) Ellis, E. F.; McKinney, J. S.; Willoughby, K. A.; Liang, S.; Povlishock, J. T. A New Model for Rapid Stretch-Induced Injury of Cells in Culture: Characterization of the Model Using Astrocytes. *J. Neurotrauma* **1995**, *12*, 325–339.

(135) Nakayama, Y.; Aoki, Y.; Niitsu, H. Studies on the Mechanisms Responsible for the Formation of Focal Swellings on Neuronal Processes Using a Novel in Vitro Model of Axonal Injury. *J. Neurotrauma* **2001**, *18*, 545–554.

(136) Lusardi, T. a; Rangan, J.; Sun, D.; Smith, D. H.; Meaney, D. F. A Device to Study the Initiation and Propagation of Calcium Transients in Cultured Neurons after Mechanical Stretch. *Ann. Biomed. Eng.* **2004**, *32*, 1546–1558.

(137) Magdesian, M. H.; Sanchez, F. S.; Lopez, M.; Thostrup, P.; Durisic, N.; Belkaid, W.; Liazoghli, D.; Grütter, P.; Colman, D. R. Atomic Force Microscopy Reveals Important Differences in Axonal Resistance to Injury. *Biophys. J.* **2012**, *103*, 405–414.

(138) Elkin, B. S.; Azeloglu, E. U.; Costa, K. D.; Morrison, B. Mechanical Heterogeneity of the Rat Hippocampus Measured by Atomic Force Microscope Indentation. *J. Neurotrauma* **2007**, *24*, 812–822.

(139) Maneshi, M. M.; Sachs, F.; Hua, S. Z. A Threshold Shear Force for Calcium Influx in an

Astrocyte Model of Traumatic Brain Injury. *J. Neurotrauma* **2015**, 150410132303002.

(140) Chronis, N. Worm Chips: Microtools for C. Elegans Biology. *Lab Chip* **2010**, *10*, 432–437.

(141) West, A. E.; Chen, W. G.; Dalva, M. B.; Dolmetsch, R. E.; Kornhauser, J. M.; Shaywitz, A. J.; Takasu, M. A.; Tao, X.; Greenberg, M. E. Calcium Regulation of Neuronal Gene Expression. *Proc. Natl. Acad. Sci. U. S. A.* **2001**, *98*, 11024–11031.

(142) Berridge, M. J.; Bootman, M. D.; Lipp, P. Calcium--a Life and Death Signal. *Nature*, 1998, *395*, 645–648.

(143) Banghart, M.; Borges, K.; Isacoff, E.; Trauner, D.; Kramer, R. H. Light-Activated Ion Channels for Remote Control of Neuronal Firing. *Nat. Neurosci.* **2004**, *7*, 1381–1386.

(144) Tyler, W. J.; Tufail, Y.; Finsterwald, M.; Tauchmann, M. L.; Olson, E. J.; Majestic, C. Remote Excitation of Neuronal Circuits Using Low-Intensity, Low-Frequency Ultrasound. *PLoS One* **2008**, *3*.

(145) Zemelman, B. V.; Lee, G. A.; Ng, M.; Miesenböck, G. Selective Photostimulation of Genetically chARGed Neurons. *Neuron* **2002**, *33*, 15–22.

(146) Boyden, E. S.; Zhang, F.; Bamberg, E.; Nagel, G.; Deisseroth, K. Millisecond-Timescale, Genetically Targeted Optical Control of Neural Activity. *Nat. Neurosci.* **2005**, *8*, 1263–1268.

(147) Sparta, D. R.; Stamatakis, A. M.; Phillips, J. L.; Hovelsø, N.; van Zessen, R.; Stuber, G. D. Construction of Implantable Optical Fibers for Long-Term Optogenetic Manipulation of Neural Circuits. *Nat. Protoc.* **2012**, *7*, 12–23.

(148) Wang, N.; Butler, J. P.; Ingber, D. E. Mechanotransduction across the Cell Surface and through the Cytoskeleton. *Science* **1993**, *260*, 1124–1127.

(149) Hughes, S.; McBain, S.; Dobson, J.; El Haj, A. J. Selective Activation of Mechanosensitive Ion Channels Using Magnetic Particles. *J. R. Soc. Interface* **2008**, *5*, 855–863.

(150) Steketee, M. B.; Moysidis, S. N.; Jin, X.-L.; Weinstein, J. E.; Pita-Thomas, W.; Raju, H. B.; Iqbal, S.; Goldberg, J. L. Nanoparticle-Mediated Signaling Endosome Localization Regulates Growth Cone Motility and Neurite Growth. *Proceedings of the National Academy of Sciences*, 2011, *108*, 19042–19047.

(151) Tay, A. K.; Dhar, M.; Pushkarsky, I.; Di Carlo, D. Research Highlights: Manipulating Cells inside and Out. *Lab Chip* **2015**, *15*, 2533–2537.

(152) Dobson, J. Remote Control of Cellular Behaviour with Magnetic Nanoparticles. *Nat. Nanotechnol.* **2008**, *3*, 139–143.

(153) Jung, S.; Bang, M.; Kim, B. S.; Lee, S.; Kotov, N. A.; Kim, B.; Jeon, D. Intracellular Gold Nanoparticles Increase Neuronal Excitability and Aggravate Seizure Activity in the Mouse Brain. *PLoS One* **2014**, *9*.

(154) Kim, S.; Im, W. S.; Kang, L.; Lee, S. T.; Chu, K.; Kim, B. I. The Application of Magnets Directs the Orientation of Neurite Outgrowth in Cultured Human Neuronal Cells. *J. Neurosci. Methods* **2008**, *174*, 91–96.

(155) Etoc, F.; Vicario, C.; Lisse, D.; Siaugue, J.-M.; Piehler, J.; Coppey, M.; Dahan, M. Magnetogenetic Control of Protein Gradients inside Living Cells with High Spatial and Temporal Resolution. *Nano Lett.* **2015**.

(156) Walkey, C. D.; Olsen, J. B.; Song, F.; Liu, R.; Guo, H.; Olsen, D. W. H.; Cohen, Y.; Emili, A.; Chan, W. C. W. Protein Corona Fingerprinting Predicts the Cellular Interaction of Gold and Silver Nanoparticles. *ACS Nano* **2014**, *8*, 2439–2455.

(157) Lesniak, A.; Fenaroli, F.; Monopoli, M. P.; Åberg, C.; Dawson, K. A.; Salvati, A. Effects of the Presence or Absence of a Protein Corona on Silica Nanoparticle Uptake and Impact on Cells. *ACS Nano* **2012**, *6*, 5845–5857.

(158) He, C.; Hu, Y.; Yin, L.; Tang, C.; Yin, C. Effects of Particle Size and Surface Charge on Cellular Uptake and Biodistribution of Polymeric Nanoparticles. *Biomaterials* **2010**, *31*, 3657–3666.

(159) Gao, H.; Yang, Z.; Zhang, S.; Cao, S.; Shen, S.; Pang, Z.; Jiang, X. Ligand Modified Nanoparticles Increases Cell Uptake, Alters Endocytosis and Elevates Glioma Distribution and Internalization. *Sci. Rep.* **2013**, *3*, 2534.

(160) Westenbroek, R. E.; Hell, J. W.; Warner, C.; Dubel, S. J.; Snutch, T. P.; Catterall, W. A. Biochemical Properties and Subcellular Distribution of an N-Type Calcium Channel Alpha 1 Subunit. *Neuron* **1992**, *9*, 1099–1115.

(161) Rao, W.; Wang, H.; Han, J.; Zhao, S.; Dumbleton, J.; Agarwal, P.; Zhang, W.; Zhao, G.; Yu, J.; Zynger, D. L.; *et al.* Chitosan-Decorated Doxorubicin-Encapsulated Nanoparticle Targets and Eliminates Tumor Reinitiating Cancer Stem-like Cells. *ACS Nano* **2015**, *9*, 5725–5740.

(162) Patel, J. C.; Witkovsky, P.; Avshalumov, M. V; Rice, M. E. Mobilization of Calcium from Intracellular Stores Facilitates Somatodendritic Dopamine Release. *J. Neurosci.* **2009**, *29*, 6568–6579.

(163) Dworakowska, B.; Dołowy, K.; Tyson, J. R.; Snutch, T. P.; Piontkivska, H.; Hughes, A. L.; Bidaud, I.; Mezghrani, A.; Swayne, L. A.; Monteil, A.; *et al.* Molecular Nature of Voltage-Gated Calcium Channels: Structure and Species Comparison. *Wiley Interdiscip. Rev. Membr. Transp. Signal.* **2013**, *2*, 181–206.

(164) Calabrese, B.; Tabarean, I. V; Juranka, P.; Morris, C. E. Mechanosensitivity of N-Type Calcium Channel Currents. *Biophys. J.* **2002**, *83*, 2560–2574.

(165) McCleskey, E. W.; Fox, A. P.; Feldman, D. H.; Cruz, L. J.; Olivera, B. M.; Tsien, R. W.; Yoshikami, D. Omega-Conotoxin: Direct and Persistent Blockade of Specific Types of Calcium Channels in Neurons but Not Muscle. *Proc. Natl. Acad. Sci. U. S. A.* **1987**, *84*, 4327–4331.

(166) Sabass, B.; Stone, H. A. Mechanosensing by Tethered Membrane Channels. *Bull. Am. Phys. Soc.* **2016**.

(167) Zhao, Q.; Wu, K.; Geng, J.; Chi, S.; Wang, Y.; Zhi, P.; Zhang, M.; Xiao, B. Ion Permeation and Mechanotransduction Mechanisms of Mechanosensitive Piezo Channels. *Neuron* **2016**, *89*, 1248–1263.

(168) Tay, A.; Kunze, A.; Jun, D.; Hoek, E.; Di Carlo, D. The Age of Cortical Neural Networks Affects Their Interactions with Magnetic Nanoparticles. *Small* **2016**.

(169) Chameau, P.; Lucas, P.; Melliti, K.; Bournaud, R.; Shimahara, T. Development of Multiple Calcium Channel Types in Cultured Mouse Hippocampal Neurons. *Neuroscience* **1999**, *90*, 383–388.

(170) Stanley, S. a; Gagner, J. E.; Damanpour, S.; Yoshida, M.; Dordick, J. S.; Friedman, J. M. Radio-Wave Heating of Iron Oxide Nanoparticles Can Regulate Plasma Glucose in Mice. *Science* **2012**, *336*, 604–608.

(171) Stanley, S. a; Sauer, J.; Kane, R. S.; Dordick, J. S.; Friedman, J. M. Remote Regulation of Glucose Homeostasis in Mice Using Genetically Encoded Nanoparticles. *Nat. Med.* **2014**, *21*, 92–98.

(172) Stanley, S. A.; Kelly, L.; Latcha, K. N.; Schmidt, S. F.; Yu, X.; Nectow, A. R.; Sauer, J.;

Dyke, J. P.; Dordick, J. S.; Friedman, J. M. Bidirectional Electromagnetic Control of the Hypothalamus Regulates Feeding and Metabolism. *Nature* **2016**.

(173) Wheeler, M. A.; Smith, C. J.; Ottolini, M.; Barker, B. S.; Purohit, A. M.; Grippo, R. M.; Gaykema, R. P.; Spano, A. J.; Beenhakker, M. P.; Kucenas, S.; *et al.* Genetically Targeted Magnetic Control of the Nervous System. *Nat. Neurosci.* **2016**.

(174) Hudspeth, A. J. Making an Effort to Listen: Mechanical Amplification in the Ear. *Neuron*, 2008, *59*, 530–545.

(175) Delmas, P.; Coste, B. Mechano-Gated Ion Channels in Sensory Systems. *Cell* **2013**, *155*, 278–284.

(176) Pravettoni, E.; Bacci, a; Coco, S.; Forbicini, P.; Matteoli, M.; Verderio, C. Different Localizations and Functions of L-Type and N-Type Calcium Channels during Development of Hippocampal Neurons. *Dev. Biol.* **2000**, *227*, 581–594.

(177) Cai, D.; Mataraza, J. M.; Qin, Z.-H.; Huang, Z.; Huang, J.; Chiles, T. C.; Carnahan, D.; Kempa, K.; Ren, Z. Highly Efficient Molecular Delivery into Mammalian Cells Using Carbon Nanotube Spearing. *Nat. Methods* **2005**, *2*, 449–454.

(178) Plank, C.; Schillinger, U.; Scherer, F.; Bergemann, C.; Rémy, J. S.; Krötz, F.; Anton, M.; Lausier, J.; Rosenecker, J. The Magnetofection Method: Using Magnetic Force to Enhance Gene Delivery. *Biological Chemistry*, 2003, *384*, 737–747.

(179) Santos, L. J.; Reis, R. L.; Gomes, M. E. Harnessing Magnetic-Mechano Actuation in Regenerative Medicine and Tissue Engineering. *Trends Biotechnol.* **2015**, *33*, 471–479.

(180) Ito, A.; Akiyama, H.; Kawabe, Y.; Kamihira, M. Magnetic Force-Based Cell Patterning Using Arg-Gly-Asp (RGD) Peptide-Conjugated Magnetite Cationic Liposomes. *J. Biosci. Bioeng.* **2007**, *104*, 288–293.

(181) Kriha, O.; Becker, M.; Lehmann, M.; Kriha, D.; Krieglstein, J.; Yosef, M.; Schlecht, S.; Wehrspohn, R. B.; Wendorff, J. H.; Greiner, A. Connection of Hippocampal Neurons by Magnetically Controlled Movement of Short Electrospun Polymer Fibers - A Route to Magnetic Micromanipulators. *Adv. Mater.* **2007**, *19*, 2483–2485.

(182) Sakar, M. S.; Steager, E. B.; Cowley, A.; Kumar, V.; Pappas, G. J. Wireless Manipulation of Single Cells Using Magnetic Microtransporters. *2011 IEEE Int. Conf. Robot. Autom.* **2011**, 2668–2673.

(183) Xie, J.; Chen, L.; Varadan, V. K.; Yancey, J.; Srivatsan, M. The Effects of Functional Magnetic Nanotubes with Incorporated Nerve Growth Factor in Neuronal Differentiation of PC12 Cells. *Nanotechnology* **2008**, *19*, 105101.

(184) Fischer, T. M.; Steinmetz, P. N.; Odde, D. J. Robust Micromechanical Neurite Elicitation in Synapse-Competent Neurons via Magnetic Bead Force Application. In *Annals of Biomedical Engineering*; 2005; Vol. 33, pp. 1229–1237.

(185) Mannix, R. J.; Kumar, S.; Cassiola, F.; Montoya-Zavala, M.; Feinstein, E.; Prentiss, M.; Ingber, D. E. Nanomagnetic Actuation of Receptor-Mediated Signal Transduction. *Nature nanotechnology*, 2008, *3*, 36–40.

(186) Rosenberg, S. S.; Spitzer, N. C. Calcium Signaling in Neuronal Development. *Cold Spring Harb. Perspect. Biol.* **2011**, *3*, 1–13.

(187) Perlmutter, J. S.; Mink, J. W. Deep Brain Stimulation. *Annu. Rev. Neurosci.* **2006**, *29*, 229–257.

(188) Matthews, B. D.; Lavan, D. A.; Overby, D. R.; Karavitis, J.; Ingber, D. E. Electromagnetic Needles with Submicron Pole Tip Radii for Nanomanipulation of Biomolecules and Living Cells. *Appl. Phys. Lett.* **2004**, *85*, 2968–2970.

(189) Carvalho-de-Souza, J. L.; Treger, J. S.; Dang, B.; Kent, S. B. H.; Pepperberg, D. R.; Bezanilla, F. Photosensitivity of Neurons Enabled by Cell-Targeted Gold Nanoparticles. *Neuron* **2015**, *86*, 207–217.

(190) Summers, H. D.; Rees, P.; Holton, M. D.; Brown, M. R.; Chappell, S. C.; Smith, P. J.; Errington, R. J. Statistical Analysis of Nanoparticle Dosing in a Dynamic Cellular System. *Nature nanotechnology*, 2011, *6*, 170–174.

(191) Jiang, W.; Kim, B. Y. S.; Rutka, J. T.; Chan, W. C. W. Nanoparticle-Mediated Cellular Response Is Size-Dependent. *Nature nanotechnology*, 2008, *3*, 145–150.

(192) Grünberg, K.; Wawer, C.; Tebo, B. M.; Schüler, D. A Large Gene Cluster Encoding Several Magnetosome Proteins Is Conserved in Different Species of Magnetotactic Bacteria. *Appl. Environ. Microbiol.* **2001**, *67*, 4573–4582.

(193) Chen, T.-W.; Wardill, T. J.; Sun, Y.; Pulver, S. R.; Renninger, S. L.; Baohan, A.; Schreiter, E. R.; Kerr, R. a; Orger, M. B.; Jayaraman, V.; *et al.* Ultrasensitive Fluorescent Proteins for Imaging Neuronal Activity. *Nature* **2013**, *499*, 295–300.

(194) Eggeman, A. S.; Majetich, S. a.; Farrell, D.; Pankhurst, Q. a. Size and Concentration Effects on High Frequency Hysteresis of Iron Oxide Nanoparticles. *IEEE Trans. Magn.* **2007**, *43*, 2451–2453.

(195) Cole, A. J.; David, A. E.; Wang, J.; Galbán, C. J.; Hill, H. L.; Yang, V. C. Polyethylene Glycol Modified, Cross-Linked Starch-Coated Iron Oxide Nanoparticles for Enhanced Magnetic Tumor Targeting. *Biomaterials* **2011**, *32*, 2183–2193.

(196) Kong, S. D.; Zhang, W.; Lee, J. H.; Brammer, K.; Lal, R.; Karin, M.; Jin, S. Magnetically Vectored Nanocapsules for Tumor Penetration and Remotely Switchable on-Demand Drug Release. *Nano Lett.* **2010**, *10*, 5088–5092.

(197) Borodinsky, L. N.; Root, C. M.; Cronin, J. a; Sann, S. B.; Gu, X.; Spitzer, N. C. Activity-Dependent Homeostatic Specification of Transmitter Expression in Embryonic Neurons. *Nature* **2004**, *429*, 523–530.

(198) O'Leary, T.; Williams, A. H.; Caplan, J. S.; Marder, E. Correlations in Ion Channel Expression Emerge from Homeostatic Tuning Rules. *Proc. Natl. Acad. Sci. U. S. A.* **2013**, *110*, E2645-54.

(199) O'Leary, T.; Williams, A. H.; Franci, A.; Marder, E. Cell Types, Network Homeostasis, and Pathological Compensation from a Biologically Plausible Ion Channel Expression Model. *Neuron* **2014**, *82*, 809–821.

(200) Beck, H.; Yaari, Y. Plasticity of Intrinsic Neuronal Properties in CNS Disorders. *Nat Rev Neurosci* **2008**, *9*, 357–369.

(201) Contractor, A.; Klyachko, V. A.; Portera-Cailliau, C. Altered Neuronal and Circuit Excitability in Fragile X Syndrome. *Neuron* **2015**, *87*, 699–715.

(202) Ferron, L.; Nieto-Rostro, M.; Cassidy, J. S.; Dolphin, A. C. Fragile X Mental Retardation Protein Controls Synaptic Vesicle Exocytosis by Modulating N-Type Calcium Channel Density. *Nat. Commun.* **2014**, *5*, 3628.

(203) Liu, B.; Li, L.; Chen, J.; Wang, Z.; Li, Z.; Wan, Q. Regulation of GABAA Receptors by Fragile X Mental Retardation Protein. *Int. J. Physiol. Pathophysiol. Pharmacol.* **2013**, *5*, 169–176.

(204) Hagerman, P. J.; Stafstrom, C. E. Origins of Epilepsy in Fragile X Syndrome. *Epilepsy Curr.* **2009**, *9*, 108–112.

(205) Weiss, N. The N-Type Voltage-Gated Calcium Channel: When a Neuron Reads a Map. *J. Neurosci.* **2008**, *28*, 5621–5622.

(206) Oberman, L.; Ifert-Miller, F.; Najib, U.; Bashir, S.; Woollacott, I.; Gonzalez-Heydrich, J.; Picker, J.; Rotenberg, A.; Pascual-Leone, A. Transcranial Magnetic Stimulation Provides Means to Assess Cortical Plasticity and Excitability in Humans with Fragile X Syndrome and Autism Spectrum Disorder. *Front. Synaptic Neurosci.* **2010**, *2*, 1–8.

(207) Snutch, T. P. Targeting Chronic and Neuropathic Pain: The N-Type Calcium Channel Comes of Age. *NeuroRx* **2005**, *2*, 662–670.

(208) Hannon, H. E.; Atchison, W. D. Omega-Conotoxins as Experimental Tools and Therapeutics in Pain Management. *Marine Drugs*, 2013, *11*, 680–699.

(209) Ino, M.; Yoshinaga, T.; Wakamori, M.; Miyamoto, N.; Takahashi, E.; Sonoda, J.; Kagaya, T.; Oki, T.; Nagasu, T.; Nishizawa, Y.; *et al.* Functional Disorders of the Sympathetic Nervous System in Mice Lacking the Alpha 1B Subunit (Cav 2.2) of N-Type Calcium Channels. *Proc. Natl. Acad. Sci. U. S. A.* **2001**, *98*, 5323–5328.

(210) Tay, A.; Schweizer, F. E.; Di Carlo, D. Micro- and Nano-Technologies to Probe the Mechano-Biology of the Brain. *Lab Chip* **2016**, *16*, 1962–1977.

(211) Prozorov, T.; Bazylinski, D. a.; Mallapragada, S. K.; Prozorov, R. Novel Magnetic Nanomaterials Inspired by Magnetotactic Bacteria: Topical Review. *Mater. Sci. Eng. R Reports* **2013**, *74*, 133–172.

(212) Yan, L.; Zhang, S.; Chen, P.; Liu, H.; Yin, H.; Li, H. Magnetotactic Bacteria, Magnetosomes and Their Application. *Microbiol. Res.* **2012**, *167*, 507–519.

(213) Valencia, P. M.; Farokhzad, O. C.; Karnik, R.; Langer, R. Microfluidic Technologies for Accelerating the Clinical Translation of Nanoparticles. *Nat. Nanotechnol.* **2012**, *7*, 623–629.

(214) Pollithy, A.; Romer, T.; Lang, C.; Müller, F. D.; Helma, J.; Leonhardt, H.; Rothbauer, U.;

Schüler, D. Magnetosome Expression of Functional Camelid Antibody Fragments (Nanobodies) in Magnetospirillum Gryphiswaldense. *Appl. Environ. Microbiol.* **2011**, *77*, 6165–6171.

(215) Gonzales, M.; Mitsumori, L. M.; Kushleika, J. V.; Rosenfeld, M. E.; Krishnan, K. M. Cytotoxicity of Iron Oxide Nanoparticles Made from the Thermal Decomposition of Organometallics and Aqueous Phase Transfer with Pluronic F127. *Contrast Media Mol. Imaging* **2010**, *5*, 286–293.

(216) Cheng, Z.; Al Zaki, A.; Hui, J. Z.; Muzykantov, V. R.; Tsourkas, A. Multifunctional Nanoparticles: Cost versus Benefit of Adding Targeting and Imaging Capabilities. *Science* **2012**, *338*, 903–910.

(217) Jones, S. R.; Wilson, T. D.; Brown, M. E.; Rahn-Lee, L.; Yu, Y.; Fredriksen, L. L.; Ozyamak, E.; Komeili, A.; Chang, M. C. Y. Genetic and Biochemical Investigations of the Role of MamP in Redox Control of Iron Biomineralization in Magnetospirillum Magneticum. *Proc. Natl. Acad. Sci. U. S. A.* **2015**, *112*, 3904–3909.

(218) Kolinko, I.; Lohße, A.; Borg, S.; Raschdorf, O.; Jogler, C.; Tu, Q.; Pósfai, M.; Tompa, E.; Plitzko, J. M.; Brachmann, A.; *et al.* Biosynthesis of Magnetic Nanostructures in a Foreign Organism by Transfer of Bacterial Magnetosome Gene Clusters. *Nat. Nanotechnol.* **2014**, *9*, 193–197.

(219) Schubbe, S.; Kube, M.; Scheffel, A.; Wawer, C.; Heyen, U.; Meyerdierks, A.; Madkour, M. H.; Mayer, F.; Reinhardt, R.; Schuler, D. Characterization of a Spontaneous Nonmagnetic Mutant of Magnetospirillum Gryphiswaldense Reveals a Large Deletion Comprising a Putative Magnetosome Island. *J. Bacteriol.* **2003**, *185*, 5779–5790.

(220) Sezonov, G.; Joseleau-Petit, D.; D'Ari, R. Escherichia Coli Physiology in Luria-Bertani

Broth. *J. Bacteriol.* **2007**, *189*, 8746–8749.

(221) Lohße, A.; Kolinko, I.; Raschdorf, O.; Uebe, R.; Borg, S.; Brachmann, A.; Plitzko, J. M.; Müller, R.; Zhang, Y.; Schüler, D. Overproduction of Magnetosomes by Genomic Amplification of Biosynthetic Gene Clusters in a Magnetotactic Bacterium. *Appl. Environ. Microbiol.* **2016**.

(222) Schultheiss, D.; Schüler, D. Development of a Genetic System for Magnetospirillum Gryphiswaldense. *Arch. Microbiol. 179*, 89–94.

(223) Šafařík, I.; Šafaříková, M. Use of Magnetic Techniques for the Isolation of Cells. *J. Chromatogr. B Biomed. Sci. Appl.* **1999**, *722*, 33–53.

(224) Blakemore, R. P. Magnetotactic Bacteria. *Annu. Rev. Microbiol.* **1982**, *36*, 217–238.

(225) Robert, D.; Pamme, N.; Conjeaud, H.; Gazeau, F.; Iles, A.; Wilhelm, C. Cell Sorting by Endocytotic Capacity in a Microfluidic Magnetophoresis Device. *Lab Chip* **2011**, *11*, 1902–1910.

(226) Pamme, N.; Wilhelm, C. Continuous Sorting of Magnetic Cells via on-Chip Free-Flow Magnetophoresis. *Lab Chip* **2006**, *6*, 974–980.

(227) Myers, R. M.; Lerman, L. S.; Maniatis, T. A General Method for Saturation Mutagenesis of Cloned DNA Fragments. *Science* **1985**, *229*, 242–247.

(228) Kolinko, I.; Jogler, C.; Katzmann, E.; Schüler, D. Frequent Mutations within the Genomic Magnetosome Island of Magnetospirillum Gryphiswaldense Are Mediated by RecA. *J. Bacteriol.* **2011**, *193*, 5328–5334.

(229) Murray, C.; Pao, E.; Tseng, P.; Aftab, S.; Kulkarni, R.; Rettig, M.; Di Carlo, D. Quantitative Magnetic Separation of Particles and Cells Using Gradient Magnetic Ratcheting. *Small* **2016**.

(230) Goodman, M. F.; Hopkins, R. L.; Lasken, R.; Mhaskar, D. N. The Biochemical Basis of 5-Bromouracil- and 2-Aminopurine-Induced Mutagenesis. *Basic Life Sci* **1985**, *31*, 409–423.

(231) Benzert, S.; Freesef, E. INDUCTION OF SPECIFIC MUTATIONS WITH 5-BROMOURACIL*. *J. Chem. Phys. J. Geophys. Res. J. Chem. Phys. Terrest. Phys. J. Chem. Phys. J. Atm. Terrest. Phys* **1594**, *98*, 2–27.

(232) Lohße, A.; Ullrich, S.; Katzmann, E.; Borg, S.; Wanner, G.; Richter, M.; Voigt, B.; Schweder, T.; Schüler, D. Functional Analysis of the Magnetosome Island in Magnetospirillum Gryphiswaldense: The mamAB Operon Is Sufficient for Magnetite Biomineralization. *PLoS One* **2011**, *6*.

(233) Scheffel, A.; Gärdes, A.; Grünberg, K.; Wanner, G.; Schüler, D. The Major Magnetosome Proteins MamGFDC Are Not Essential for Magnetite Biomineralization in Magnetospirillum Gryphiswaldense but Regulate the Size of Magnetosome Crystals. *J. Bacteriol.* **2008**, *190*, 377–386.

(234) Wu, W.; He, Q.; Jiang, C. Magnetic Iron Oxide Nanoparticles: Synthesis and Surface Functionalization Strategies. *Nanoscale Res. Lett.* **2008**, *3*, 397–415.

(235) Hou, Y.; Xu, Z.; Sun, S. Controlled Synthesis and Chemical Conversions of FeO Nanoparticles. *Angew. Chemie - Int. Ed.* **2007**, *46*, 6329–6332.

(236) Vácha, R.; Martinez-Veracoechea, F. J.; Frenkel, D. Receptor-Mediated Endocytosis of Nanoparticles of Various Shapes. *Nano Lett.* **2011**, *11*, 5391–5395.

(237) Brunner, T. J.; Wick, P.; Manser, P.; Spohn, P.; Grass, R. N.; Limbach, L. K.; Bruinink, A.; Stark, W. J. In Vitro Cytotoxicity of Oxide Nanoparticles: Comparison to Asbestos, Silica, and the Effect of Particle Solubility †. *Environ. Sci. Technol.* **2006**, *40*, 4374–4381.

(238) Matsunaga, T.; Okamura, Y.; Fukuda, Y.; Wahyudi, A. T.; Murase, Y.; Takeyama, H. Complete Genome Sequence of the Facultative Anaerobic Magnetotactic Bacterium Magnetospirillum Sp. Strain AMB-1. *DNA Res.* **2005**, *12*, 157–166.

(239) Taoka, A.; Eguchi, Y.; Mise, S.; Oestreicher, Z.; Uno, F.; Fukumori, Y. A Magnetosome-Associated Cytochrome MamP Is Critical for Magnetite Crystal Growth during the Exponential Growth Phase. *FEMS Microbiol. Lett.* **2014**, *358*, 21–29.

(240) Murat, D.; Falahati, V.; Bertinetti, L.; Csencsits, R.; Körnig, A.; Downing, K.; Faivre, D.; Komeili, A. The Magnetosome Membrane Protein, MmsF, Is a Major Regulator of Magnetite Biomineralization in Magnetospirillum Magneticum AMB-1. *Mol. Microbiol.* **2012**, *85*, 684–699.

(241) Wang, D.; Bodovitz, S. Single Cell Analysis: The New Frontier in "Omics." *Trends in Biotechnology*, 2010, *28*, 281–290.

(242) Zhao, L.; Wu, D.; Wu, L.-F.; Song, T. A Simple and Accurate Method for Quantification of Magnetosomes in Magnetotactic Bacteria by Common Spectrophotometer. *J. Biochem. Biophys. Methods* **2007**, *70*, 377–383.

(243) Gossett, D. R.; Weaver, W. M.; MacH, A. J.; Hur, S. C.; Tse, H. T. K.; Lee, W.; Amini, H.; Di Carlo, D. Label-Free Cell Separation and Sorting in Microfluidic Systems. *Analytical and Bioanalytical Chemistry*, 2010, *397*, 3249–3267.

(244) Berg, H. C. The Rotary Motor of Bacterial Flagella. *Annu Rev Biochem* **2003**, *72*, 19–54.

(245) Schultheiss, D.; Kube, M.; Schüler, D. Inactivation of the Flagellin Gene flaA in Magnetospirillum Gryphiswaldense Results in Nonmagnetotactic Mutants Lacking Flagellar Filaments. *Appl. Environ. Microbiol.* **2004**, *70*, 3624–3631.

(246) Alphandéry, E.; Ding, Y.; Ngo, A. T.; Wang, Z. L.; Wu, L. F.; Pileni, M. P. Assemblies of

Aligned Magnetotactic Bacteria and Extracted Magnetosomes: What Is the Main Factor Responsible for the Magnetic Anisotropy? *ACS Nano* **2009**, *3*, 1539–1547.

(247) Uebe, R.; Schüler, D. Magnetosome Biogenesis in Magnetotactic Bacteria. *Nat. Rev. Microbiol.* **2016**, *14*, 621–637.

(248) Warkiani, M. E.; Tay, A. K. P.; Guan, G.; Han, J. Membrane-Less Microfiltration Using Inertial Microfluidics. *Sci. Rep.* **2015**, *5*, 11018.

(249) Katzmann, E.; Müller, F. D.; Lang, C.; Messerer, M.; Winklhofer, M.; Plitzko, J. M.; Schüler, D. Magnetosome Chains Are Recruited to Cellular Division Sites and Split by Asymmetric Septation. *Mol. Microbiol.* **2011**, *82*, 1316–1329.

(250) Shimoshige, H.; Kobayashi, H.; Mizuki, T.; Nagaoka, Y.; Inoue, A.; Maekawa, T. Effect of Polyethylene Glycol on the Formation of Magnetic Nanoparticles Synthesized by Magnetospirillum Magnetotacticum MS-1. *PLoS One* **2015**, *10*, e0127481.

(251) Warkiani, M. E.; Tay, A. K. P.; Khoo, B. L.; Xiaofeng, X.; Han, J.; Lim, C. T. Malaria Detection Using Inertial Microfluidics. *Lab Chip* **2014**, *15*, 1101–1109.

(252) Popp, F.; Armitage, J. P.; Schüler, D. Polarity of Bacterial Magnetotaxis Is Controlled by Aerotaxis through a Common Sensory Pathway. *Nat. Commun.* **2014**, *5*, 5398.

(253) Jaqaman, K.; Loerke, D.; Mettlen, M.; Kuwata, H.; Grinstein, S.; Schmid, S. L.; Danuser, G. Robust Single-Particle Tracking in Live-Cell Time-Lapse Sequences. *Nat. Methods* **2008**, *5*, 695–702.

(254) Pantoja, R.; Nagarah, J. M.; Starace, D. M.; Melosh, N. A.; Blunck, R.; Bezanilla, F.; Heath, J. R. Silicon Chip-Based Patch-Clamp Electrodes Integrated with PDMS Microfluidics. In *Biosensors and Bioelectronics*; 2004; Vol. 20, pp. 509–517.

(255) Hennig, G. W.; Gould, T. W.; Koh, S. D.; Corrigan, R. D.; Heredia, D. J.; Shonnard, M.

C.; Smith, T. K. Use of Genetically Encoded Calcium Indicators (GECIs) Combined with Advanced Motion Tracking Techniques to Examine the Behavior of Neurons and Glia in the Enteric Nervous System of the Intact Murine Colon. *Front. Cell. Neurosci.* **2015**, *9*, 436.

(256) Inoue, M.; Takeuchi, A.; Horigane, S.; Ohkura, M.; Gengyo-Ando, K.; Fujii, H.; Kamijo, S.; Takemoto-Kimura, S.; Kano, M.; Nakai, J.; *et al.* Rational Design of a High-Affinity, Fast, Red Calcium Indicator R-CaMP2. *Nat. Methods* **2014**, *12*, 64–70.

(257) Berlin, S.; Carroll, E. C.; Newman, Z. L.; Okada, H. O.; Quinn, C. M.; Kallman, B.; Rockwell, N. C.; Martin, S. S.; Lagarias, J. C.; Isacoff, E. Y. Photoactivatable Genetically Encoded Calcium Indicators for Targeted Neuronal Imaging. *Nat. Methods* **2015**, 1–10.

(258) Palmer, A. E.; Giacomello, M.; Kortemme, T.; Hires, S. A.; Lev-Ram, V.; Baker, D.; Tsien, R. Y. Ca2+ Indicators Based on Computationally Redesigned Calmodulin-Peptide Pairs. *Chem. Biol.* **2006**, *13*, 521–530.

(259) Peterka, D. S.; Takahashi, H.; Yuste, R. Imaging Voltage in Neurons. *Neuron*, 2011, *69*, 9–21.

(260) Hochbaum, D. R.; Zhao, Y.; Farhi, S. L.; Klapoetke, N.; Werley, C. A.; Kapoor, V.; Zou, P.; Kralj, J. M.; Maclaurin, D.; Smedemark-Margulies, N.; *et al.* All-Optical Electrophysiology in Mammalian Neurons Using Engineered Microbial Rhodopsins. *Nat. Methods* **2014**, *11*, 825–833.

(261) Akemann, W.; Mutoh, H.; Perron, A.; Rossier, J.; Knöpfel, T. Imaging Brain Electric Signals with Genetically Targeted Voltage-Sensitive Fluorescent Proteins. *Nat. Methods* **2010**, *7*, 643–649.

(262) St-Pierre, F.; Chavarha, M.; Lin, M. Z. Designs and Sensing Mechanisms of Genetically

Encoded Fluorescent Voltage Indicators. *Curr. Opin. Chem. Biol.* **2015**, *27*, 31–38.

(263) Jahn, A.; Reiner, J. E.; Vreeland, W. N.; DeVoe, D. L.; Locascio, L. E.; Gaitan, M. Preparation of Nanoparticles by Continuous-Flow Microfluidics. *Journal of Nanoparticle Research*, 2008, *10*, 925–934.

(264) Cabeza, V. S.; Kuhn, S.; Kulkarni, A. a; Jensen, K. F. Size-Controlled Flow Synthesis of Gold Nanoparticles Using a Segmented Flow Micro Fluidic Platform. *30th Anniv. Langmuir* **2012**, *28*, 7007–7013.

(265) Karnik, R.; Gu, F.; Basto, P.; Cannizzaro, C.; Dean, L.; Kyei-Manu, W.; Langer, R.; Farokhzad, O. C. Microfluidic Platform for Controlled Synthesis of Polymeric Nanoparticles. *Nano Lett.* **2008**, *8*, 2906–2912.

(266) Song, Y.; Hormes, J.; Kumar, C. S. S. R. Microfluidic Synthesis of Nanomaterials. *Small*, 2008, *4*, 698–711.

(267) Zhao, C. X.; He, L.; Qiao, S. Z.; Middelberg, A. P. J. Nanoparticle Synthesis in Microreactors. *Chem. Eng. Sci.* **2011**, *66*, 1463–1479.

(268) Blakemore, R. Magnetotactic Bacteria. *Science (80-.).* **1975**, *190*, 377–379.

(269) Xie, J.; Chen, K.; Chen, X. Production, Modification and Bio-Applications of Magnetic Nanoparticles Gestated by Magnetotactic Bacteria. *Nano Research*, 2009, *2*, 261–278.

(270) Lee, H.; Purdon, A. M.; Chu, V.; Westervelt, R. M. Controlled Assembly of Magnetic Nanoparticles from Magnetotactic Bacteria Using Microelectromagnets Arrays. *Nano Lett.* **2004**, *4*, 995–998.

(271) Lang, C.; Schüler, D. Expression of Green Fluorescent Protein Fused to Magnetosome Proteins in Microaerophilic Magnetotactic Bacteria. *Appl. Environ. Microbiol.* **2008**, *74*, 4944–4953.

(272) Zurkiya, O.; Chan, A. W. S.; Hu, X. MagA Is Sufficient for Producing Magnetic Nanoparticles in Mammalian Cells, Making It an MRI Reporter. *Magn. Reson. Med.* **2008**, *59*, 1225–1231.

(273) Packer, M. S.; Liu, D. R. Methods for the Directed Evolution of Proteins. *Nat. Rev. Genet.* **2015**, *16*, 379–394.

(274) Feng, M.; Lu, Y.; Yang, Y.; Zhang, M.; Xu, Y.-J.; Gao, H.-L.; Dong, L.; Xu, W.-P.; Yu, S.-H. Bioinspired Greigite Magnetic Nanocrystals: Chemical Synthesis and Biomedicine Applications. *Sci. Rep.* **2013**, *3*, 2994.

(275) Gao, Y.; Wei, Z.; Li, F.; Yang, Z. M.; Chen, Y. M.; Zrinyi, M.; Osada, Y. Synthesis of a Morphology Controllable Fe 3 O 4 Nanoparticle/hydrogel Magnetic Nanocomposite Inspired by Magnetotactic Bacteria and Its Application in H 2 O 2 Detection. *Green Chem.* **2014**, *16*, 1255–1261.

(276) Shilo, M.; Sharon, A.; Baranes, K.; Motiei, M.; Lellouche, J.-P. M.; Popovtzer, R. The Effect of Nanoparticle Size on the Probability to Cross the Blood-Brain Barrier: An in-Vitro Endothelial Cell Model. *J. Nanobiotechnology* **2015**, *13*, 19.

(277) Lockman, P. R.; Koziara, J. M.; Mumper, R. J.; Allen, D. D. Nanoparticle Surface Charges Alter Blood-Brain Barrier Integrity and Permeability. *J. Drug Target.* **2004**, *12*, 635–641.

(278) Petros, R. a; DeSimone, J. M. Strategies in the Design of Nanoparticles for Therapeutic Applications. *Nat. Rev. Drug Discov.* **2010**, *9*, 615–627.

(279) Qiao, R.; Jia, Q.; Hüwel, S.; Xia, R.; Liu, T.; Gao, F.; Galla, H. J.; Gao, M. Receptor-Mediated Delivery of Magnetic Nanoparticles across the Blood-Brain Barrier. *ACS Nano* **2012**, *6*, 3304–3310.

(280) Wiley, D. T.; Webster, P.; Gale, A.; Davis, M. E. Transcytosis and Brain Uptake of Transferrin-Containing Nanoparticles by Tuning Avidity to Transferrin Receptor. *Proc. Natl. Acad. Sci. U. S. A.* **2013**, *110*, 8662–8667.

(281) Clark, A. J.; Davis, M. E. Increased Brain Uptake of Targeted Nanoparticles by Adding an Acid-Cleavable Linkage between Transferrin and the Nanoparticle Core. *Proc. Natl. Acad. Sci. U. S. A.* **2015**, *112*, 12486–12491.

(282) Liu, H.-L.; Hua, M.-Y.; Yang, H.-W.; Huang, C.-Y.; Chu, P.-C.; Wu, J.-S.; Tseng, I.-C.; Wang, J.-J.; Yen, T.-C.; Chen, P.-Y.; *et al.* Magnetic Resonance Monitoring of Focused Ultrasound/magnetic Nanoparticle Targeting Delivery of Therapeutic Agents to the Brain. *Proc. Natl. Acad. Sci. U. S. A.* **2010**, *107*, 15205–15210.

(283) Kong, S. D.; Lee, J.; Ramachandran, S.; Eliceiri, B. P.; Shubayev, V. I.; Lal, R.; Jin, S. Magnetic Targeting of Nanoparticles across the Intact Blood-Brain Barrier. *J. Control. Release* **2012**, *164*, 49–57.

(284) Jinhao, G. A. O.; Hongwei, G. U.; Bing, X. U. Multifunctional Magnetic Nanoparticles: Design, Synthesis, and Biomedical Applications. *Acc. Chem. Res.* **2009**, *42*, 1097–1107.

(285) Yin, H.; Too, H. P.; Chow, G. M. The Effects of Particle Size and Surface Coating on the Cytotoxicity of Nickel Ferrite. *Biomaterials* **2005**, *26*, 5818–5826.

(286) Jain, T. K.; Reddy, M. K.; Morales, M. A.; Leslie-Pelecky, D. L.; Labhasetwar, V. Biodistribution, Clearance, and Biocompatibility of Iron Oxide Magnetic Nanoparticles in Rats. *Mol. Pharm.* **2008**, *5*, 316–327.

(287) Pankhurst, Q. a; Connolly, J.; Jones, S. K.; Dobson, J. Applications of Magnetic Nanoparticles in Biomedicine. *J. Phys. D. Appl. Phys.* **2003**, *36*, R167–R181.

(288) Reddy, L. H.; Arias, J. L.; Nicolas, J.; Couvreur, P. Magnetic Nanoparticles: Design and

Characterization, Toxicity and Biocompatibility, Pharmaceutical and Biomedical Applications. *Chemical Reviews*, 2012, *112*, 5818–5878.

(289) Tartaj, P.; Morales, M. a D. P.; Veintemillas-Verdaguer, S.; Gonz lez-Carre o, T.; Serna, C. J. The Preparation of Magnetic Nanoparticles for Applications in Biomedicine. *J. Phys. D. Appl. Phys.* **2003**, *36*, R182–R197.

(290) Puri, I. K.; Ganguly, R. Particle Transport in Therapeutic Magnetic Fields. *Annu. Rev. Fluid Mech.* **2014**, *46*, 407–440.

(291) Halbach, K. Design of Permanent Multipole Magnets with Oriented Rare Earth Cobalt Material. *Nucl. Instruments Methods* **1980**, *169*, 1–10.

(292) Bonmassar, G.; Lee, S. W.; Freeman, D. K.; Polasek, M.; Fried, S. I.; Gale, J. T. Microscopic Magnetic Stimulation of Neural Tissue. *Nat. Commun.* **2012**, *3*, 921.

(293) Oxley, T. J.; Opie, N. L.; John, S. E.; Rind, G. S.; Ronayne, S. M.; Wheeler, T. L.; Judy, J. W.; McDonald, A. J.; Dornom, A.; Lovell, T. J. H.; *et al.* Minimally Invasive Endovascular Stent-Electrode Array for High-Fidelity, Chronic Recordings of Cortical Neural Activity. *Nat. Biotechnol.* **2016**, *34*, 320–327.

(294) Cho, Y.; Shi, R.; Ben Borgens, R. Chitosan Nanoparticle-Based Neuronal Membrane Sealing and Neuroprotection Following Acrolein-Induced Cell Injury. *J. Biol. Eng.* **2010**, *4*, 2.

(295) Wang, X.; Chi, N.; Tang, X. Preparation of Estradiol Chitosan Nanoparticles for Improving Nasal Absorption and Brain Targeting. *Eur. J. Pharm. Biopharm.* **2008**, *70*, 735–740.

(296) Malhotra, M.; Tomaro-Duchesneau, C.; Prakash, S. Synthesis of TAT Peptide-Tagged PEGylated Chitosan Nanoparticles for siRNA Delivery Targeting Neurodegenerative

Diseases. *Biomaterials* **2013**, *34*, 1270–1280.

(297) Kim, D. K.; Mikhaylova, M.; Wang, F. H.; Kehr, J.; Bjelke, B.; Zhang, Y.; Tsakalakos, T.; Muhammed, M. Starch-Coated Superparamagnetic Nanoparticles as MR Contrast Agents. *Chem. Mater.* **2003**, *15*, 4343–4351.

(298) Linemann, T.; Thomsen, L. B.; du Jardin, K. G.; Laursen, J. C.; Jensen, J. B.; Lichota, J.; Moos, T. Development of a Novel Lipophilic, Magnetic Nanoparticle for in Vivo Drug Delivery. *Pharmaceutics* **2013**, *5*, 246–260.

(299) Obermeier, a; Küchler, S.; Matl, F. D.; Pirzer, T.; Stemberger, a; Mykhaylyk, O.; Friess, W.; Burgkart, R. Magnetic Drug Targeting as New Therapeutic Option for the Treatment of Biomaterial Infections. *J. Biomater. Sci. Polym. Ed.* **2011**.

(300) Pala, A.; Liberatore, M.; D'Elia, P.; Nepi, F.; Megna, V.; Mastantuono, M.; Al-Nahhas, A.; Rubello, D.; Barteri, M. Labelling of Granulocytes by Phagocytic Engulfment with 64Cu-Labelled Chitosan-Coated Magnetic Nanoparticles. *Mol. Imaging Biol.* **2012**, *14*, 593–598.

(301) Ruge, C. A.; Schaefer, U. F.; Herrmann, J.; Kirch, J.; Cañadas, O.; Echaide, M.; Pérez-Gil, J.; Casals, C.; Müller, R.; Lehr, C. M. The Interplay of Lung Surfactant Proteins and Lipids Assimilates the Macrophage Clearance of Nanoparticles. *PLoS One* **2012**, *7*.

(302) Purves, D.; Augustine, G. J.; Fitzpatrick, D.; Katz, L. C.; LaMantia, A.-S.; McNamara, J. O.; Williams, S. M. The Nociceptive Components of the Thalamus and Cortex, 2001.

(303) Dhaka, A.; Viswanath, V.; Patapoutian, A. Trp Ion Channels and Temperature Sensation. *Annu. Rev. Neurosci.* **2006**, *29*, 135–161.

(304) Gu, Y.; Gu, C. Physiological and Pathological Functions of Mechanosensitive Ion Channels. *Molecular Neurobiology*, 2014, *50*, 339–347.

(305) Harteneck, C.; Gollasch, M. Pharmacological Modulation of Diacylglycerol-Sensitive TRPC3/6/7 Channels. *Curr. Pharm. Biotechnol.* **2011**, *12*, 35–41.

(306) Qin, X.; Yue, Z.; Sun, B.; Yang, W.; Xie, J.; Ni, E.; Feng, Y.; Mahmood, R.; Zhang, Y.; Yue, L. Sphingosine and FTY720 Are Potent Inhibitors of the Transient Receptor Potential Melastatin 7 (TRPM7) Channels. *British Journal of Pharmacology*, 2013, *168*, 1294–1312.

(307) Kim, T. J.; Joo, C.; Seong, J.; Vafabakhsh, R.; Botvinick, E. L.; Berns, M. W.; Palmer, A. E.; Wang, N.; Ha, T.; Jakobsson, E.; *et al.* Distinct Mechanisms Regulating Mechanical Force-Induced Ca2+ Signals at the Plasma Membrane and the ER in Human MSCs. *Elife* **2015**, *2015*.

(308) Ranade, S. S.; Woo, S.-H.; Dubin, A. E.; Moshourab, R. A.; Wetzel, C.; Petrus, M.; Mathur, J.; Bégay, V.; Coste, B.; Mainquist, J.; *et al.* Piezo2 Is the Major Transducer of Mechanical Forces for Touch Sensation in Mice. *Nature* **2014**, *516*, 121–125.

(309) Borbiro, I.; Badheka, D.; Rohacs, T. Activation of TRPV1 Channels Inhibits Mechanosensitive Piezo Channel Activity by Depleting Membrane Phosphoinositides. *Sci. Signal.* **2015**, *8*, ra15.

(310) Volkers, L.; Mechioukhi, Y.; Coste, B. Piezo Channels: From Structure to Function. *Pflugers Archiv European Journal of Physiology*, 2014, *467*, 95–99.

(311) Goldstein, S. a; Bockenhauer, D.; O'Kelly, I.; Zilberberg, N. Potassium Leak Channels and the KCNK Family of Two-P-Domain Subunits. *Nat. Rev. Neurosci.* **2001**, *2*, 175–184.

(312) Brohawn, S. G.; Su, Z.; MacKinnon, R. Mechanosensitivity Is Mediated Directly by the Lipid Membrane in TRAAK and TREK1 K + Channels. *Proc. Natl. Acad. Sci.* **2014**, *111*, 3614–3619.

(313) Wheeler, M. A.; Smith, C. J.; Ottolini, M.; Barker, B. S.; Purohit, A. M.; Grippo, R. M.; Gaykema, R. P.; Spano, A. J.; Beenhakker, M. P.; Kucenas, S.; *et al.* Genetically Targeted Magnetic Control of the Nervous System. *Nat. Neurosci.* **2016**.

(314) Poole, K.; Herget, R.; Lapatsina, L.; Ngo, H.-D. D.; Lewin, G. R.; Herget, R.; Lapatsina, L.; Ngo, H.-D. D.; Lewin, G. R.; Herget, R.; *et al.* Tuning Piezo Ion Channels to Detect Molecular-Scale Movements Relevant for Fine Touch. *Nat. Commun.* **2014**, *5*, 3520.

(315) Shevkoplyas, S. S.; Siegel, A. C.; Westervelt, R. M.; Prentiss, M. G.; Whitesides, G. M. The Force Acting on a Superparamagnetic Bead due to an Applied Magnetic Field. *Lab Chip* **2007**, *7*, 1294–1302.

(316) Leith, D. Drag on Nonspherical Objects. *Aerosol Sci. Technol.* **1987**, *6*, 153–161.

(317) Loehr, J.; Pfeiffer, D.; Schüler, D.; Fischer, T. M. Magnetic Guidance of the Magnetotactic Bacterium Magnetospirillum Gryphiswaldense. *Soft Matter* **2016**.

(318) Bazylinski, D. A.; Garratt-Reed, A. J.; Frankel, R. B. Electron Microscopic Studies of Magnetosomes in Magnetotactic Bacteria. *Microsc. Res. Tech.* **1994**, *27*, 389–401.

(319) Le Sage, D.; Arai, K.; Glenn, D. R.; DeVience, S. J.; Pham, L. M.; Rahn-Lee, L.; Lukin, M. D.; Yacoby, a; Komeili, a; Walsworth, R. L. Optical Magnetic Imaging of Living Cells. *Nature* **2013**, *496*, 486–489.

(320) Xia, N.; Hunt, T. P.; Mayers, B. T.; Alsberg, E.; Whitesides, G. M.; Westervelt, R. M.; Ingber, D. E. Combined Microfluidic-Micromagnetic Separation of Living Cells in Continuous Flow. *Biomed. Microdevices* **2006**, *8*, 299–308.

(321) Woehl, T. J.; Kashyap, S.; Firlar, E.; Perez-Gonzalez, T.; Faivre, D.; Trubitsyn, D.; Bazylinski, D. A.; Prozorov, T. Correlative Electron and Fluorescence Microscopy of Magnetotactic Bacteria in Liquid: Toward in Vivo Imaging. *Sci. Rep.* **2014**, *4*, 6854.

(322) Eder, S. H. K.; Gigler, A. M.; Hanzlik, M.; Winklhofer, M. Sub-Micrometer-Scale Mapping of Magnetite Crystals and Sulfur Globules in Magnetotactic Bacteria Using Confocal Raman Micro-Spectrometry. *PLoS One* **2014**, *9*.